Detection of Fatigue Crack in Metallic Structures with

In-Situ Phased Array Ultrasonics

BY

TANJA RAKOVIC
B.S., University of Illinois at Chicago, 2020

THESIS

Submitted as partial fulfillment of the requirements
for the degree of Master of Science in Civil Engineering
in the Graduate College of the
University of Illinois at Chicago, 2021

Chicago, Illinois

Defense Committee:

Dr. Didem Ozevin, Chair and Advisor
Dr. Ernesto Indacochea, Civil, Materials, and Environmental Engineering
Dr. Sheng-Wei Chi, Civil, Materials, and Environmental Engineering

This thesis is dedicated to my mother, Jela, who always pushed me to new heights and supported me in every way possible. I also dedicate this work to my uncle Milorad who encouraged me to continue my education even from 5000 miles away. Finally, I dedicate this work to my folklore ensemble "Oko Sokolovo" for keeping me grounded and being supportive throughout this journey.

ACKNOWLEDGMENTS

I would like to thank the many people that helped make this thesis possible. First, thank you to my thesis committee Dr. Didem Ozevin, Dr. Ernesto Indacochea, and Dr. Sheng-Wei Chi for their support, enthusiasm towards this project and timely responses when reviewing this thesis. My mentor, Dr. Didem Ozevin, is inspiring, dedicated and very knowledgeable about this topic that I had limited knowledge on. She made sure I was ready to tackle the challenges of this project and accepted me as a research assistant, which allowed me to gain experience conducting research and helped fund my graduate studies. Even throughout the pandemic she made sure everything smoothly and as normal as possible. For all of this, I am forever grateful. I would like to thank Dr. Ernesto Indacochea, and Dr. Sheng-Wei Chi for their invaluable feedback and expert opinion while reviewing this thesis. Thank you to Gorkem Okudan for answering my many questions and helping me with many parts of this project including numerical modelling and MATLAB inputs. I would also like to thank Sara Arevalo for her timely answers to my questions and helping me with all the requirements necessary to finish my graduate studies. Finally, thank you to the UIC Machine Shop for their assistance.

TR

TABLE OF CONTENTS

LIST OF TABLES

LIST OF FIGURES

LIST OF ABBREVIATIONS

AE   Acoustic Emission

CT   Compact Tension

DAQ   Data Acquisition

DI   Damage Index

DIs   Damage Indices

FFT   Fast Fourier Transform

LRFD   Load and Resistance Factor Design

NDE   Nondestructive Evaluation

PZT   Lead Zirconate Titanate

PoD   Probability of Detection

SHM   Structural Health Monitoring

UT   Ultrasonic Testing

SUMMARY

A study of obtaining ultrasonic data and correlating it to the fatigue crack length was carried out using numerical and experimental methods. The fundamental goal was to use a guided wave ultrasonic testing (UT) phase array to detect a crack from one position in a modified compact tension (CT) specimen. The specimen was equipped with one transducer and seven receivers, which were used to detect damage signals for a fatigue crack up to 10 mm. Numerical and experimental studies both captured ultrasonic data that was converted into waveforms. The waveform data in specified time and frequency domains were used to calculate various damage indices (DIs) referencing the crack-free baseline condition and the new surface wave condition and correlate them to the fatigue crack length.

Numerical studies were conducted using COMSOL Multiphysics to obtain response information about each receiver. The 2D structural steel 6.25 inch x 6 inch rectangular specimen with 1.5 inch x 2.5 inch rectangular loading pins was modelled, with the sensors represented by points on top of the specimen. First, a static model was completed to ensure the stresses allowed the crack to form at the notch tip first and to check plasticity. Once this was confirmed, dynamic models were made with additional varying crack lengths and the excitation signal generated by MATLAB and the Hilbert transform. Frequencies of 400 kHz and 300 kHz were tested. The signal waveforms were obtained and analyzed for a certain time domain, which was around the expected crack arrival. The damage indices were calculated from the signal data based on amplitude, energy, frequency and phase shift. Acceptable damage index (DI) equations from each category were identified and they demonstrated that sensors 2 and 3 were most sensitive to

SUMMARY (Continued)

damage detection, especially at 400 kHz and when the time range analyzed was around the

expected crack arrival.

Experimental studies on the same specimen were performed to obtain ultrasonic signals

at 400 kHz and 300 kHz. Fatigue loading using the Instron 8500 servo-hydraulic fatigue testing

machine was conducted to grow the fatigue crack up to 8.53 mm which corresponded to 80,000

cycles. The optical microscope captured pictures after each 10,000 cycle interval which were

used later to measure the crack length in MATLAB's Image Processing Toolbox. The 4 cycle

sine wave excitation signal was applied to the transmitter. The Mistras data acquisition system

recorded the ultrasonic data for each receiver, which was used to calculate the experimental

damage indices. The same equations were used from the numerical study. The results indicated

that both sensors 2 and 3 were more effective at 400 kHz than at 300 kHz and during the time

range of the expected crack signal. A comparison of the numerical and experimental results

showed some differences between the modelling and actual setup, but overall a similar trend was

observed. The results confirmed that both DIs referencing the crack-free condition and the

surface wave can be used to detect damage. Further research can include using acoustic

emissions to record the signals *in-situ*, using probability of detection curves to predict the most

effective DI, studying higher frequencies and studying more samples to validate the approach.

1. INTRODUCTION

1.1 Statement of Problem

Metal structures are subject to different types of cyclic loads including live and environmental (wind, snow, rain). With enough cyclic loading, micro-cracks start to form which later increase in size and then eventually cause the structure to fail. A metal's fatigue strength is the only way to know how many loading cycles it can undergo before failing. Even with this knowledge, it is important to monitor the structure either continuously or periodically by using structural health monitoring (SHM) techniques. These can include acoustic emission (AE), UT and thermal imaging, which can provide information about the structure in real-time and prevent failure. For large structures like bridges and airplanes, SHM is vital in order to prevent catastrophic failure and consequently loss of life and destruction. Even though there are some disadvantages of SHM regarding interpretation of data and the need for experienced personnel, research on this topic is increasing and requirements for the successful implementation of SHM are becoming clearer.

1.2 Objective and Approach

The objective of this study is to use a guided wave UT phase array to detect a crack from one position in a test specimen designed to grow a crack at the notch tip. The UT waveforms were analyzed to develop effective DIs to detect the fatigue crack. The maximum energy, maximum amplitude, frequency and phase shift parameters were used to correlate the data with fatigue crack length.

The research approach required numerical and experimental methods to achieve the objective. The numerical models were created in the COMSOL Multiphysics software. The first model was completely static and only used the solid mechanics physics. This provided information about the maximum stresses and where the crack was expected to form first in the specimen. The succeeding models were dynamic and used an additional time-dependent physics which depended on the frequency, wave propagation velocity and load function. One model was made for each expected crack length, and they revealed signals that were used to calculate the DIs. The experiment was conducted using the specimen made of structural steel. Fatigue tests were completed to grow the crack, which were measured directly using the images processed with the MATLAB Image Processing Toolbox. The DIs were calculated from the corresponding UT tests, which were compared to the numerical results. The relationship between DI and crack length were obtained. Figure 1 shows a flowchart of the methods used for this thesis to obtain the necessary information needed to calculate the DIs.
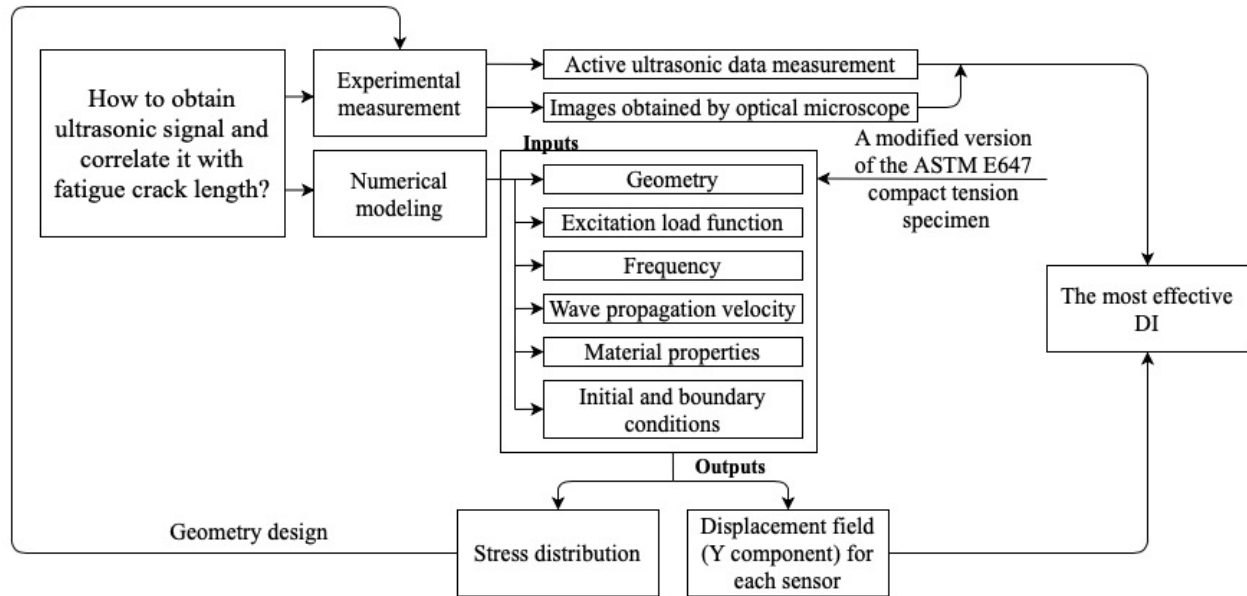
Figure 1. Flowchart outlining the experimental and numerical processes with inputs and outputs generated by the COMSOL Multiphysics software.

1.3 Structure of Thesis

The thesis is structured so that the problem statement is provided first, followed by the main objective and types of models and experiments performed. Chapter 2 discusses fatigue crack propagation characteristics, their applications to metal structures and nondestructive evaluation (NDE) methods used to detect fatigue cracks, including AE and UT. Additionally, the various ways to calculate DIs to characterize crack propagation and apply it to SHM are discussed. Chapter 3 introduces the numerical models completed in COMSOL Multiphysics, including the static stress model and the numerous dynamic models simulating the ultrasonic wave propagation throughout the structure transmitted by an actuator (represented by a point) closest to the notch tip, while the other sensors record the data. Two frequencies and seven different crack lengths were modeled. Chapter 4 describes the experimental studies and the

3

corresponding setup. The experiment consisted of fatigue testing, *in-situ* phased-array UT and optical microscope analysis. The optical microscope was used to obtain pictures of the notch tip and crack after each 10,000 cycle interval, which were analyzed in MATLAB to obtain the actual crack lengths. The correlation between the ultrasonic data and crack length was obtained for different DIs. These results were compared with the numerical results and the most effective DIs were chosen. Finally, Chapter 5 summarizes this research and discusses major findings and future work.

2. LITERATURE REVIEW

2.1 Introduction

Structures can experience fatigue cracks when subjected to repeated cyclic loads. If the cracks become too large then the structure may fail catastrophically, leading to damage, injuries and more money needed to complete repairs. Structures where fatigue cracks are common include the spline section of a gearbox in a helicopter transmission system [1], high-speed railroads [2], bogie frames in railway vehicles [3], heavy ship and aerospace structures [4] and bridges. To prevent serious damage, it is imperative to monitor these structures. When cracks first initiate, they can be very small and hard to detect with the human eye. It is ineffective to take no action until the crack grows large enough so that humans can see it. As loads on these structures continue increase, structural integrity concerns continue to rise, which is why effective methods for locating and determining the extent of damage is needed.

2.2 Fatigue Cracks in Metallic Structures

Metallic structures are subject to repetitive loading, which is one of the biggest reasons for their failure [5]. In fact, 90% of these failures are caused by fatigue cracks [5]. There are three fatigue crack stages: 1) initiation stage, when the crack just begins to form at critical zones where the stresses are high, 2) propagation stage, when the crack grows and any repairs could still be done in this stage and 3) fracture stage, when the crack becomes so large that the member breaks. This is shown in Figure 2, where da/dN is crack growth per cycle and ΔK is the stress intensity factor range. It shows the crack growing quickly in the beginning and end stages until ultimate fracture occurs.
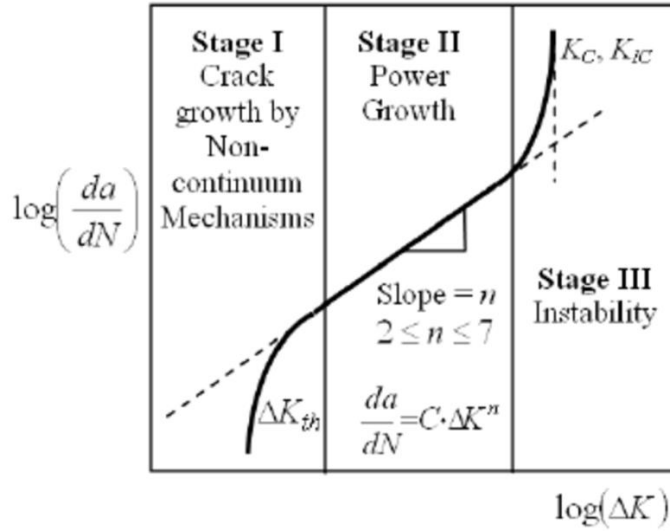
Figure 2. Stages of fatigue crack propagation [6].

An example of fatigue cracks in real-world structures are ones found in the spline section of a gearbox in a helicopter transmission system. The non-redundant spline section component is subjected to externally cyclic loading and is more likely to develop fatigue cracks [1]. Because it is non-redundant, it is important to detect fatigue cracks before they start to propagate quickly. Rails also encounter internal fatigue cracks that can contribute to train derailments [2]. This is due to the contact of the rail and wheel and the subsequent extensive loads. Any necessary repairs could lead to closures and cost a substantial amount of money. For example, in 2012 a Norfolk Southern train derailed in Columbus, Ohio due to rolling contact fatigue [7]. The cost of damage was $1.2 million and 100 people were evacuated [7]. Bogie frames, also part of railway structures, may fail suddenly due to fatigue cracks that developed because of heavy loads and high speeds [3]. Loads and speeds have been increasing to meet increasing product demand. However, this has been leading to more accidents such as collision and derailment [3]. Heavy

ship structures are also prone to fatigue damage because of high loads caused by waves, cargo distributions and vibrations [8]. Similar to railways, ships provide an important transportation mode to meet increasing demands. The failure of this structure can also cause loss of life as well as supply chain disruption. In bridges, fatigue cracks are usually located in under-bridge members, which are difficult and expensive to access. Damage occurring in a fracture critical member, which is a steel member in tension, could cause an entire bridge to collapse if it failed [9].

Therefore, there are many structures that people rely on every day where fatigue failure is inevitable due to high cyclic loadings. In order to prevent catastrophic failure, inspection is needed either by the hands-on method or NDE method. If damage such as cracks are located on the surface and they are large enough, then conventional methods such as image processing and thermal imaging can be used. However, ideal conditions need to be present including enough light and high camera resolution.

2.3 Nondestructive Evaluation Methods for Detecting Fatigue Cracks

Nondestructive evaluation methods are used to detect and locate flaws in materials without affecting the integrity of the material [10]. Periodic inspections are performed from time to time, depending on the structure's age and if any new changes arise. Continuous monitoring involves leaving sensors on a structure for an extended period of time, which is known as SHM. Contact sensing involves touching the structure while non-contact sensing does not. The two main methods discussed in this research are UT, which is an active NDE method and AE, which is a passive NDE method. Both methods involve contact in this study, and therefore need to be attached to the structure to record its response. Other common NDE methods applied to metallic

7

structures include eddy current, infrared imaging, liquid penetrant inspection and magnetic

particle inspection.

UT is particularly popular because of its high penetration capabilities, sensitivity, quick

results and lack of hazards to the operators [2]. The sound waves travel through the material with

attenuation and they are reflected where there are flaws. Cracks and other types of damage are

characterized by a metal/gas interface, which means that the wave can reflect completely at

cracks. UT includes guided waves, bulk waves and nonlinear waves. The bulk and guided waves

are shown in Figure 3 depending on different mediums and frequencies.
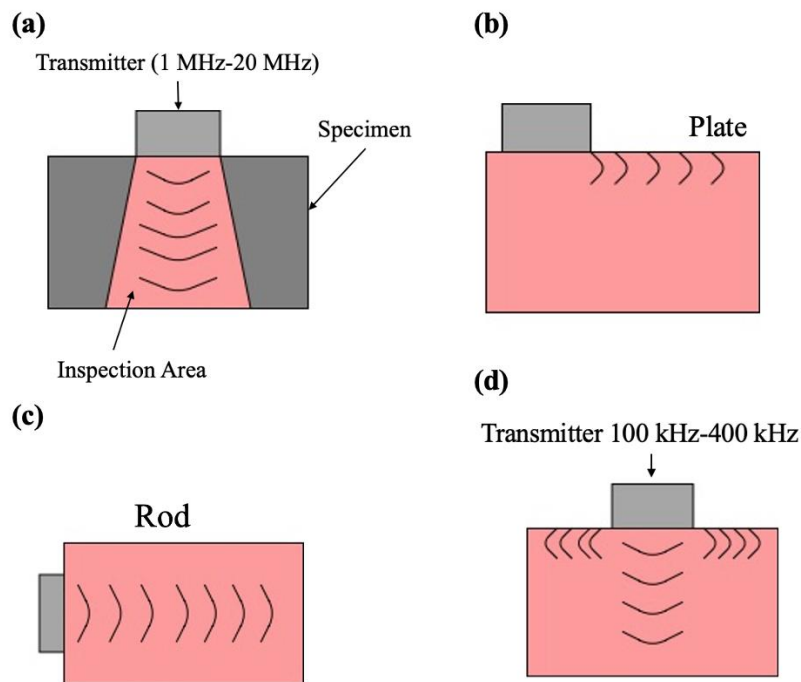
Figure 3. Type of UT waves: (a) bulk waves, (b) guided waves in a plate, (c) guided waves in a rod and (d) guided waves based on frequency.

Guided waves are commonly used by researchers because they have a longer range than bulk waves and can travel without too much attenuation [11]. This is particularly useful for long structures like bridges, pipes and rails. Yan et al. used ultrasonic guided waves to investigate the weld zone of a bogie frame since this area is highly susceptible to damage due to high rail speeds and heavy loads [3]. A notch was artificially created at the weld zone and the T-shaped specimen was excited with five-peak sine waves modulated by a cosine. Five piezoelectric lead zirconate titanate (PZT) disks were used as actuators and five were used as sensors. It was found that no acceptable signals were produced below a 200 kHz frequency and they did not change noticeably due to small cracks. At 300 kHz, the waveforms were too complicated, so 240 kHz was used. The crack length was characterized using DI equations (discussed further in Section 2.3.1) which allowed for long-term SHM. This was beneficial since bogie frames are used for long periods of time which increases the chance for fatigue crack growth. Zhu et al. also used ultrasonic guided waves to detect fatigue cracks under the vibration condition for SHM in a 650 mm x 60 mm x 4 mm steel beam [4]. Static loads ranging from 0 to 24 MPa were used as they least influenced wave propagation. The excitation signal consisted of a five cycle sinusoidal wave modulated by the Hanning window at frequencies from 60-100 kHz. Two PZT patches were used as the actuator and sensor, located on either end of the beam. After 67,000 cycles an 8 mm length crack was noticed. The subsequent DI results allowed for an accurate method to detect fatigue cracks under vibration condition. Ultrasonic guided waves were also proposed for use in an experiment to characterize a fatigue crack in thin metal plates by Abbas and Shafiee [11]. By conducting a literature search, they found that the crack orientation, shape, width, depth and length were directly related to the output signal in a plate surface. Sensor placement with respect to the incident guided waves was also important to consider. To address these concerns, the proposed

experiment would form cracks with various shapes and orientations on the plates with PZT

sensors located around the crack. The actuator would be placed in the middle, close to the crack,

but this would also be varied throughout the experiment. This setup would allow for optimal

detection of output signal patterns. By using ultrasonic guided waves and confirming

experimental results with a numerical model, this would give information about damage

tolerance in metal plates and improve guided wave UT techniques. Another type of guided

waves, Rayleigh waves, were applied by Ushakov et al. to investigate surface and subsurface

zones of metals [12]. The rectangular specimen was incised with a notch at depths from 0 mm to

3.2 mm to measure the amplitude and time of the output signal at frequencies ranging from 2.5 to

5.0 MHz. The transmitter and receiver were located on either side of the notch. The recorded

signal amplitudes depended on notch depth, and it was found that the amplitude sharply

decreased at a frequency of 5.0 MHz, as the notch depth increased at the same time. This

frequency was well defined for fatigue crack depths ranging from 0.6 to 20 mm. For cracks

deeper than 20 mm, the optimal frequency was 2.5 MHz or 1.8 MHz. A reported limitation was

that if the crack was located at the specimen's edge, the Rayleigh waves penetrated right through

it and the recorded crack depth was smaller than the actual value. Lamb waves, also part of

guided waves, were used by Michaels in a spatially distributed array of PZT sensors that acted

both as transmitters and receivers [13]. An advantage of this spatially distributed configuration

was the ability to capture the damage location from many angles, increasing the probability of

detection. The six sensors were attached to a 610 mm x 610 mm x 4.76 mm aluminum plate. The

transducers were excited with a commercial spike mode pulse receiver at a frequency of 250

kHz. These signals were used to localize damage and compare it to the baseline condition. A

delay-and-sum algorithm proved to be most effective for this objective. Guided waves have many advantages, but bulk and nonlinear waves have also been used for ultrasonic inspection.

Bulk waves were used by Ali et al. in plate samples with two different materials: aluminum and austenitic stainless steel [14]. Twelve notches 10 mm long and 3 mm wide were machined into the samples. The excitation signal consisted of a 3 cycle Hanning windowed toneburst at a frequency of 2 MHz. An average of 30 trials were completed to account for experimental uncertainties. This experiment compared probability of detection (PoD) curves for empirical and classical curves (discussed further in Section 2.4). Predicting this curve can give insight into the best method for detecting small cracks. However, this was limited to certain crack configurations. In Felice and Fan's review of ultrasonic sizing techniques using bulk wave testing, it was determined that indications of damage using bulk waves may show even without any damage [15]. This was due to multiple crack reflections or the presence of a bulk wave within a creeping wave. More research may need to be done to obtain improved results with bulk waves and to test different crack orientations, which is also a limitation of guided waves.

There has also been an increase in research relating to fatigue crack detection using non-linear ultrasonics. This is an area of interest because linear ultrasonics are sometimes not sensitive enough to detect these small cracks. Wang et al. investigated the effect of sensor position, wave cycles and frequency on fatigue crack detection using nonlinear UT [16]. A finite element model of a 90 mm x 50 mm x 3 mm aluminum plate was built in the LS-DYNA software. A crack was simulated at the tip of the notch, located at the top center of the model. The actuating signal was a 10 cycle sinusoidal tone-burst signal modulated by the Hanning window at a frequency of 1.2 MHz. The nonlinear parameter β' showed a linear upward trend as the crack grew. It was found that a smaller number of cycles at a higher frequency increased the

sensitivity of nonlinear detection. The sensors closest to the crack and exciter showed the largest

upward change in β'. These results were confirmed with an experiment which used the same

setup as in the numerical model. The experimental results showed that β' grew as the crack grew,

but not at the same rate as the numerical β'. This was because the fatigue crack did not actually

propagate in a straight line and therefore acted differently than what was modelled in the

software. Finally, it was found that as the angle between the crack and the sensor increased, the

sensitivity of crack detection decreased. Similar reasoning was used in this research for the

differences in numerical and experimental results discussed in Chapters 3 and 4.

Even with these classic methods, there are still new UT methods being researched.

Meksen et al. discussed a method that replaced an image with a sparse matrix to detect cracks

automatically by analyzing the matrix elements [17]. This was beneficial since images of large

structures come with a great extent of data, and the fatigue crack was extremely small compared

to the structure, which made it difficult to see. The matrix was created with the Split-Spectrum

Process, and then the Randomized Hough transform was applied to detect hyperbolas which

were used to characterize cracks.

Therefore, many researchers have employed UT using guided waves, bulk waves and

nonlinear waves for improvement of UT techniques, SHM and accurate damage localization.

Numerous advantages include accuracy, high sensitivity, portability and lack of hazards to

operators. However, disadvantages of UT include the need for experienced personnel, couplants

for effective transfer of waves between the transducer and structural element, and the waves not

registering damage if the structural element is too small or thin. Table I shows a summary of all

the UT parameters used by researchers.

Table I: SUMMARY OF UT PARAMETERS USED BY RESEARCHERS

Researcher(s)	_Structure investigated (Material)_	_Frequency_	_Excitation signal_	_Type of UT wave_
Yan et al. [3]	Weld zone of a bogie frame (Q235 steel)	240 kHz	Five peak sine waves modulated by a cosine	Guided
Zhu et al. [4]	Beam (304 steel)	60 - 100 kHz	Five cycle sinusoidal wave modulated by the Hanning window	Guided
Abbas and Shafiee [11]	Thin metal plates (Aluminum)	N/A since the experiment was not conducted	N/A since the experiment was not conducted	Guided
Ushakov et al. [12]	Surface and subsurface zones of rectangular metal specimen (06Х12НДЛ cast hydroturbine steel)	2.5 - 5.0 MHz	Rayleigh wave transforms into surface wave, where the minimum signal to noise ratio is 5.0 dB	Guided (Rayleigh)
Michaels [13]	Plate (Aluminum)	250 kHz	Transducers excited with a commercial spike mode pulse receiver	Guided (Lamb)
Ali et al. [14]	Plate (Aluminum and austenitic stainless steel)	2 MHz	3 cycle Hanning windowed toneburst	Bulk
Wang et al. [16]	Plate (Aluminum)	1.2 MHz	10 cycle sinusoidal tone-burst signal modulated by the Hanning window	Nonlinear

2.3.1 Damage Indices of Ultrasonic Measurement

The damage index calculated from acoustic features is used to characterize damage in solids [3,5]. It can also be used for SHM by monitoring fatigue crack growth, determining the crack length and damage identification [3]. DIs based on the amplitude and energy of the ultrasonic signal within a certain time or frequency domain have been commonly used by researchers [3,5,18,19,20]. In general, the principle of amplitude and energy-based DIs relies on the ultrasonic signal. Figure 4 shows an ultrasonic waveform and the corresponding cumulative energy curve from T. Michaels and J. Michaels [19]. The maximum energy within a certain time window is taken to calculate the energy-based DIs, and from the waveforms the maximum amplitude can be obtained to calculate the amplitude-based DIs.
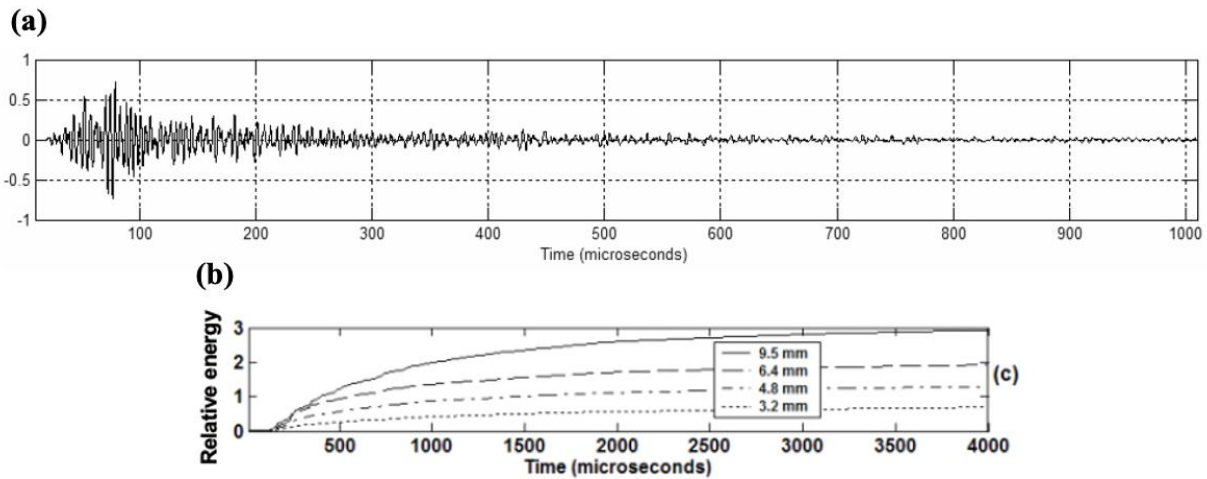
Figure 4. Example of ultrasonic (a) waveform and (b) cumulative energy curve [19].

While Yan et al. used amplitude and energy-based DIs for a single actuator-sensor path in the time domain [3] as shown in Table II, Jin et al. used normalized amplitude and energy DIs for multiple actuator-sensor paths in the time domain [5] as shown in Table III. This method was successful and showed that using different actuator-sensor pairs produced the most useful crack location information [5,21].

Table II: DI EQUATIONS USED BY YAN ET AL. [3]

DI Number	Equation	Description
1	$DI_1 = |A_1 - A_2|/A_1$	Amplitude-based
2	$DI_2 = \sqrt{\int [f_2(t) - f_1(t)]^2 \, dt / \int [f_1(t)]^2 \, dt}$	Root mean square deviation-based
3	$DI_3 = \left(\frac{1}{T}\right) \int [f(t) - \bar{f}(t)]^2 \, dt$	Mean variance-based
4	$DI_4 = (\int |f_1(t)|^2 \, dt)/(\int |f_2(t)|^2 \, dt)$	Energy-based
5	$DI_5 = (\int |f_1(t) - f_2(t)|^2 \, dt)/(\int |f_1(t)|^2 \, dt)$	Energy-based
6	$DI_6 = |\int [f_2(t)]^2 \, dt - \int [f_1(t)]^2 \, dt|/(\int [f_1(t)]^2 \, dt)$	Energy-based
7	$DI_7 = (\int |f_1(t)|^2 \, dt - \int |f_2(t)|^2 dt)/(\int |f_2(t)|^2 \, dt)$	Energy-based
8	$DI_8 = \ln A_2/A_1$	Amplitude attenuation-based

15

The undamaged signal is $f_1(t)$, while $f_2(t)$ is the crack signal. A_1 is the amplitude of the undamaged signal and A_2 is the amplitude of crack signal. It was found that the energy-based DI_6 produced the best results. The other equations were also acceptable, but the unacceptable DIs were DI_4 based on mean variance and DI_7 based on energy. These were based on the first arrival window and typical actuator-sensors paths. It was also found that if the crack propagated towards the actuator-sensor path, this affected the signal. The amplitude reached zero if the crack passed the actuator-sensor path (starting from the notch). If multiple actuator–sensor paths and arrivals were to be used, the propagation of the crack could be monitored up to 74 mm long.

Table III: DI EQUATIONS USED BY JIN ET AL. [5]

DI Number	Equation	Description
1	$DI(i,j)_{1,k-t} = \dfrac{u(i,j)_{B-k}(t) - u(i,j)_{D-k}(t)}{u(i,j)_{B-k}(t)}$	Magnitude-based
2	$DI(i,j)_{2,k-f} = \dfrac{u(i,j)_{B-k}(f) - u(i,j)_{D-k}(f)}{u(i,j)_{B-k}(f)}$	Amplitude-based
3	$DI(i,j)_{3,k-t} = \dfrac{\int_{t1}^{t2}[u(i,j)_{B-k}(t) - u(i,j)_{D-k}(t)]^2 dt}{\int_{t1}^{t2} u(i,j)_{B-k}^2(t)\, dt}$	Energy-based
4	$DI(i,j)_{4,k-f} = \dfrac{\int_{f1}^{f2}[u(i,j)_{B-k}(f) - u(i,j)_{D-k}(f)]^2 df}{\int_{f1}^{f2} u(i,j)_{B-k}^2(f)\, df}$	Energy-based
5	$DI(i,j)_{5,magnitude-fusion-t}$ $= \sum_{k=1}^{N}(\alpha_{magnitude-k-t}DI(i,j)_{magnitude-k-t}$	Magnitude-based
6	$DI(i,j)_{6,amplitude-fusion-f}$ $= \sum_{k=1}^{N}(\alpha_{amplitude-k-f}DI(i,j)_{amplitude-k-f}$	Amplitude-based
7	$DI(i,j)_{7,energy-fusion-t} = \sum_{k=1}^{N}(\alpha_{energy-k-t}DI(i,j)_{energy-k-t}$	Energy-based
8	$DI(i,j)_{8,energy-fusion-f} = \sum_{k=1}^{N}(\alpha_{energy-k-f}DI(i,j)_{energy-k-f}$	Energy-based

The actuator-sensor path $A_i - S_j$ is represented by $DI(i,j)$. The subscript k represents the kth $A_i - S_j$ path, t is time and f is frequency. $u(i,j)_{B-k}(t)$ and $u(i,j)_{D-k}(t)$ correspond to the baseline signal and current signal of the S_0 mode. $DI(i,j)_{5,magnitude-fusion-t}$, and $DI(i,j)_{7,energy-fusion-t}$ are the ultimate fusion DIs in the time domain. $DI(i,j)_{6,amplitude-fusion-f}$ and $DI(i,j)_{8,energy-fusion-f}$ are synthetic DIs in the frequency domain. α represents the weights of each path. The hybrid DIs (number 5-8) were made to combine all the available DIs for the sensor configuration. This was beneficial because it helped minimize external noise and experimental uncertainties. It was found that magnitude and energy-based DIs in the time domain were not very effective in predicting crack size. This is because if the crack was too small, its magnitude was almost unnoticeable. While all the DIs produced high correlation coefficients with respect to the crack length, the ones in the frequency domain were higher, suggesting that they can characterize fatigue crack propagation more accurately. The synthetic fusion DIs were also able to achieve the same objective, but the amplitude-based frequency (non-fusion) DIs overall showed the best results.

Figure 5 shows DI results from Yan et al. [3] and Jin et al. [5] with similar trends where the DI increased as the crack length increased. This was expected since the signal amplitude and energy increased as the crack grew. The DIs also leveled off when the crack length reached a certain point. Yan et al. found that cracks were detectable in the range of 20 mm toward the actuator-sensor path [3], while Jin et al. was able to detect cracks in the range of 15 mm [5].
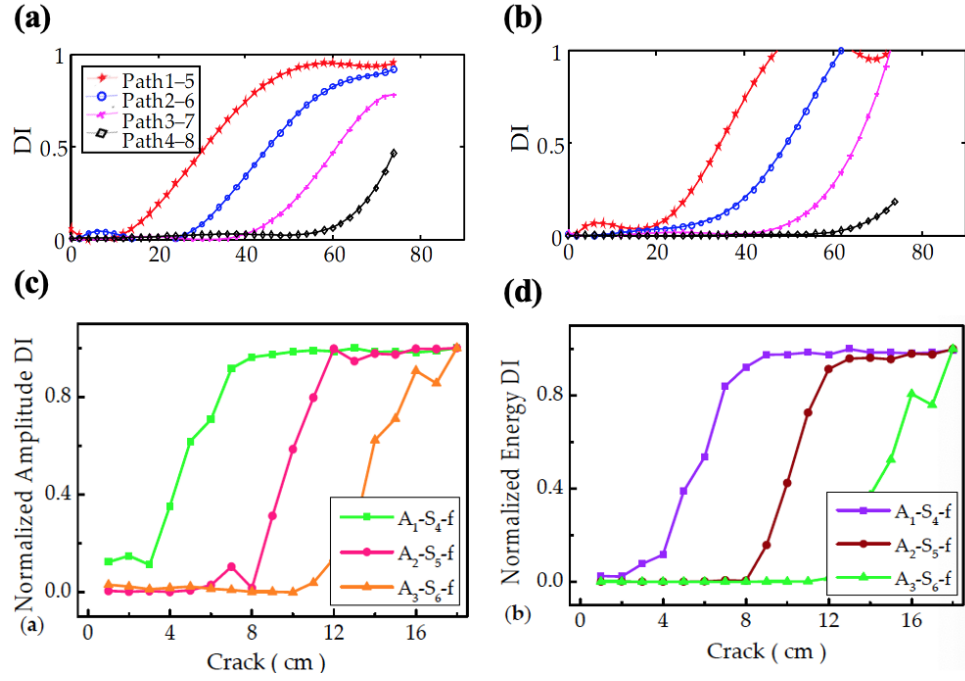
Figure 5. Acceptable damage index (a) based on amplitude [3], (b) based on energy [3], (c) based on amplitude [5] and (d) based on energy [5].

A less commonly used method using a sequence curve, was used by Zhu et al. as a crack detection method for a specimen with and without a crack [4]. It was found that transmission signals were more sensitive than reflection signals, so they were used to calculate the DI. The DI equations are shown in Table IV.

Table IV: DI EQUATIONS USED BY ZHU ET AL. [4]

DI Number	Equation		Description
1	$$DI_1 = \frac{RMS(S_1 - S_2)}{RMS(S_1) + RMS(S_2)}$$		Root mean square-based
2	$$DI_2 < f_t(u), h_t(u) > = \frac{RMS(f_t(u) - h_t(u))}{RMS(f_t(u)) + RMS(h_t(u))}$$		Sequence curve of DI
-	$f_t(u) = g(u - t)f(u)$	$h_t(u) = g(u - t)h(u)$	-

The first baseline signal is S_1, while S_2 is the second signal with crack. RMS is the root mean square, $g(u)$ is the rectangular window function, $f(u)$ and $h(u)$ are different signals and $f_t(u)$ and $h_t(u)$ are the different signals in a window function. These DIs also displayed similar results as the aforementioned research and increased with crack size. The DIs were on the order of magnitude of 10^{-1} for the cracked case, which according to the researchers, was typical for the fatigue crack condition and therefore it was acceptable and could be used to identify the fatigue crack.

Many times, the DI was calculated in the literature by comparing signals from damaged structures to signals from the undamaged structure. T. Michaels and J. Michaels detected damage using this method by subtracting the two signals and obtaining the peak amplitude and/or energy [19]. Mal et al. calculated a DI based on the spectra of the two signals and the frequency response function of the structure [22]. Banerjee et al. compared the dynamic response of the two signals and determined a threshold where anything above it was reliable and gave information about damage proximity [23]. Michaels et al. used both time and frequency domain features where the sensors needed to be attached on or near the structure [24]. Comparing the signal with

damage to the baseline signal was useful when damage is the only variable present. While the previously mentioned DIs are popular in research, there are also DIs based on nonlinear UT as well as new innovative DIs.

Lee and Hong used nonlinear UT to investigate structural integrity by using a damage index in addition to an intactness index [25]. The DI depended on the number of sideband occurrences and the total number of experiments, and the intactness index was found by comparing magnitudes obtained at the same frequency in two different experiments. The values of both indices indicated whether the specimen was intact or if a crack was present. Another DI was introduced by Climent-Llorca, et al. which involved a new parameter based on frequency and amplitudes of the first and second-order intermodulation products [26].
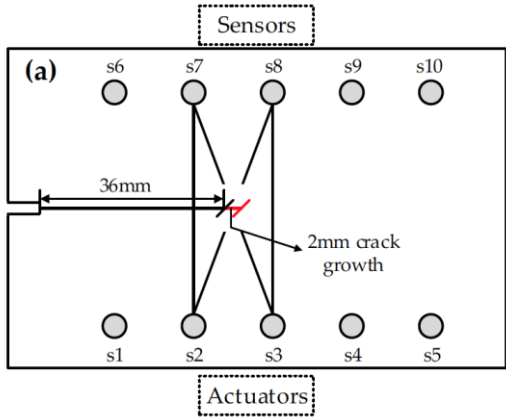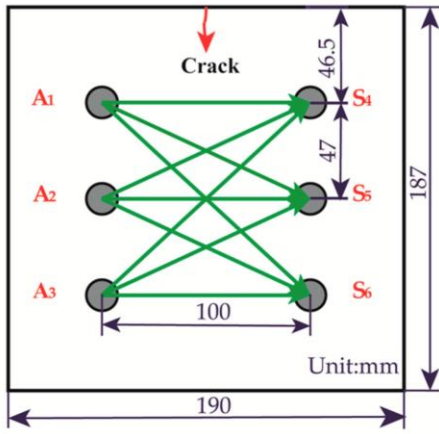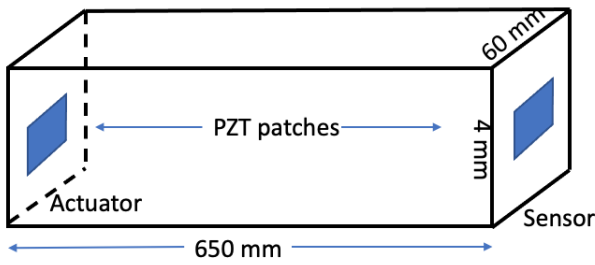
Jin et al. incorporated the innovative linear fusions of DIs as shown previously in Table III and differential fusion of DIs, which was verified with an experiment conducted on a steel plate structure using a high stability frequency of 265 kHz [5]. These DIs differ from more commonly used amplitude and energy-based DIs because they can provide information about crack propagation, not just crack localization. It was found that the hybrid DIs can characterize propagation of fatigue cracks. Si and Zongfeng quantified structural damage with an acousto-ultrasonics based multi-damage index approach [27]. SHM was done with energy and phase divergence indices. An experiment was conducted to validate the multi-damage index approach on two specimens: one in pristine condition and one with cracks. They found that the intensity of reflected waves in the damaged specimen was linearly proportional to the incident wave intensity and damage size.
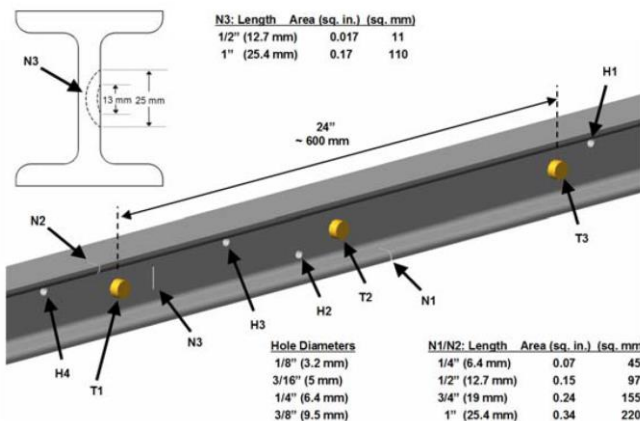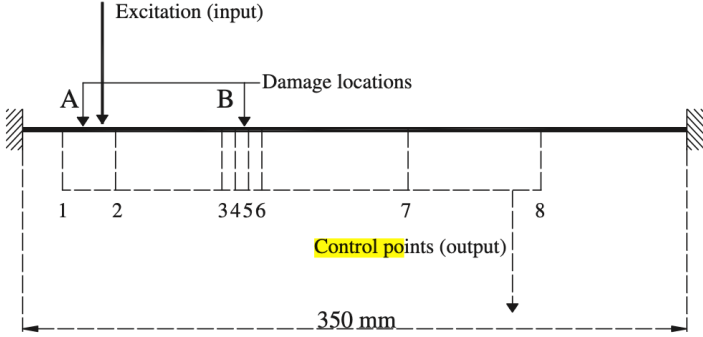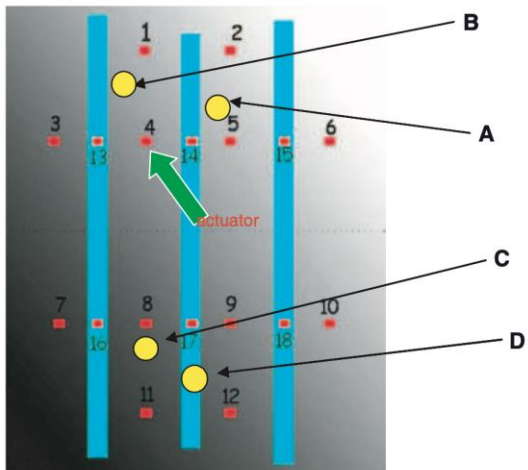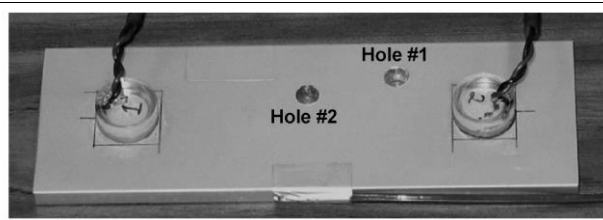
Common transmitter receiver configurations used by these researchers are summarized in Table V. They showed the transmitters and receivers across from each other with the crack in the

middle or lined up with/near the cracks (or other type of damage) throughout the entire structure. The more transmitter-receiver paths used, the more sensitive the damage detection may be because the sensors gather the damage information from multiple angles.

Table V: COMMON TRANSMITTER RECEIVER CONFIGURATIONS USED BY RESEARCHERS

Researcher(s)	Transmitter Receiver Configuration	Details
Yan et al. [3]		Actuators and sensors were across from each other. Single actuator-sensor paths were used.
Jin et al. [5]		Actuators were sensors are across from each other. Multiple actuator-sensor paths were used.
Zhu et al. [4]		PZT patches placed on either end of the beam as an actuator and sensor.

T. Michaels and J. Michaels [19]		T is the transducer, N is the notch and H is the hole. Holes and notches were placed throughout the beam and transducers spaced in between them.
Mal et al. [22]		The control points were used to record the signal in a beam. Most of them were concentrated around the damage location.
Banerjee et al. [23]		The red circles represent PZT sensors on the panel (except #4 which was the actuator), which were near the impact locations (yellow circles).
Michaels et al. [24]		Ultrasonic sensors located on either side of the plate with damage in the middle.

This research used DIs based on amplitude, energy, frequency and phase shift. Amplitude and energy DIs were used from Table II because they were made for a single actuator-sensor path, and signals for the baseline and crack condition were available. All these conditions apply to this research, so these DIs were chosen for further analysis. However, this research will present the equations differently, with subscripts referring to different waveforms or different windows (discussed further in Section 3.4). The most effective DIs will be summarized and compared to experimental results.

2.3.2 Prior Study on Detecting Fatigue Damage in Metals

In a previous study of the UIC Civil, Materials and Environmental Engineering research group, an idealized spline section of a gearbox was tested using AE and UT arrays. Acoustic emission is generated from mechanical deformations and fractures. Transient elastic waves form due to a rapid energy release when the stress in the material increases [28]. Using sensors to detect AE signals allows for continuous SHM and crack detection/localization since there are sudden changes in stress and displacement in the crack region. Most short events (e.g., crack jump) contribute to bursts of energy while longer events are categorized as continuous even though these are likely just many overlapping burst events [29]. A novel method of identifying AE signatures to locate fatigue damage in a flattened bevel gear spline was developed [1]. The new piezoelectric sensors that could also function as UT shown as the Metis sensor array in Figure 6 were able to detect crack growth events and after 237,000 cycles the continuous emission increased which signified sudden crack jumps. In this research, a similar sensor array was used and a modified compact tension specimen was tested to detect the fatigue crack with a phase-array configuration and access from one side of structure.

25
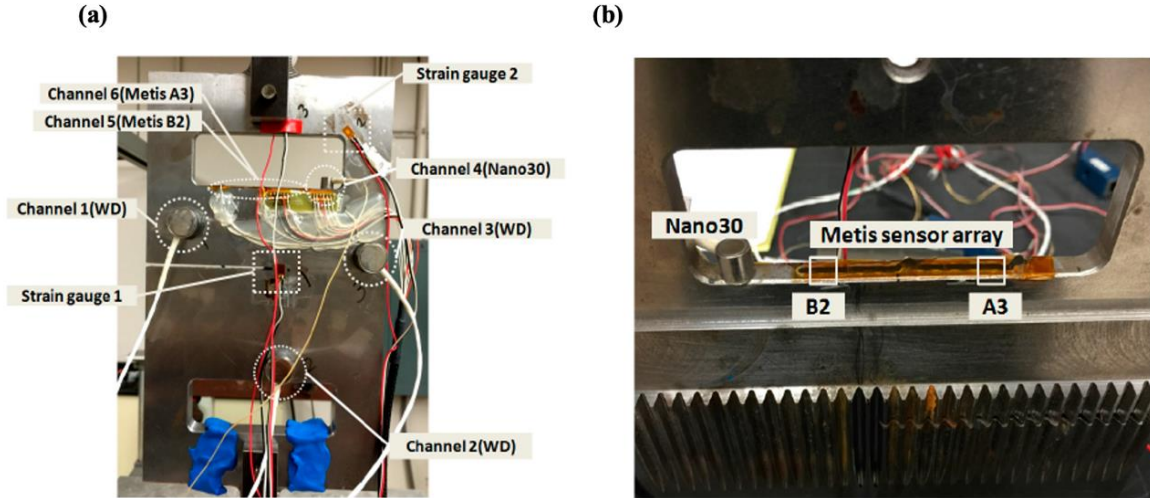
Figure 6. Idealized flattened bevel gear spline showing (a) test geometry wiht AE sensors, channels 1 to 4 and (b) Metis sensor array used as AE and UT sensors [1].

With the capability of detecting the fatigue crack in real time without the requirement of close proximity to the crack, AE has been applied to detect defects in metallic structures. For instance, Elasha et al. also applied AE to detect bearing faults in helicopter gearbox systems [30]. The experiment was completed using the following conditions: fault-free, minor bearing damage and major bearing damage. AE detected minor and major defect conditions, which was outstanding because typically AE was used for static structures instead of moving helicopter components. Strantza et al. considered AE to monitor crack propagation in additive manufacturing components prone to fatigue failure [31]. TI6Al4V components under four-point bending with and without notches were tested to detect, characterize and localize any cracks. AE signals and parameters were evaluated, and it was found that they were sensitive enough to predict fracture. Kral et al. used AE in combination with artificial neural networks to detect damage before it occurs in a flat aluminum panel [32]. Two AE sensors recorded the signals, and

the artificial neural network was used to instantly identify them as crack growth or noise.

Holford et al. investigated AE for damage location in steel bridges [33]. The most AE events were recorded in the inner web and a shear stud in the upper flange. These regions usually correspond with the highest stress amounts, so this can likely be correlated to a fatigue crack. In this study, while the AE data was recorded during fatigue testing, the results will not be reported.

2.4 Probability of Detection Curves for Ultrasonics

Probability of detection curves can be used to assess the reliability of NDE methods. There are two main methods of obtaining a PoD curve: 1) Hit/Miss, where the results simply state if a defect was found or not and 2) Signal Response, also known as $\hat{a}$ vs. a. Equations 2.1-2.5 are necessary to formulate a PoD curve [34]. The signal response is $\hat{a}$, while the defect size is a. The parameters β_0 and β_1 are obtained from the linear regression of the $log(\hat{a})$ vs. $log(a)$ plot. δ is random error, $\hat{a}_{th}$ is the decision threshold, μ is the mean and σ is the standard deviation. It is assumed that Equation 2.1 follows a normal distribution.

$$\ln(\hat{a}) = \beta_0 + \beta_1 \ln(a) + \delta \tag{2.1}$$

$$PoD(a) = Probability(\ln(\hat{a}) > \ln(\hat{a}_{th})) \tag{2.2}$$

$$PoD(a) = 1 - \phi \left[\frac{\ln(\hat{a}_{th}) - (\beta_0 + \beta_1 \ln(a))}{\sigma_\delta} \right] \tag{2.3}$$

$$\mu = \frac{\ln(\hat{a}_{th}) - \beta_0}{\beta_1} \tag{2.4}$$

$$\sigma = \frac{\sigma_\delta}{\beta_1} \tag{2.5}$$

The $\hat{a}$ vs. a method is more commonly used with NDE because it correlates the defect response $\hat{a}$ with the defect dimension a, as shown in Figure 7 [14, 34].
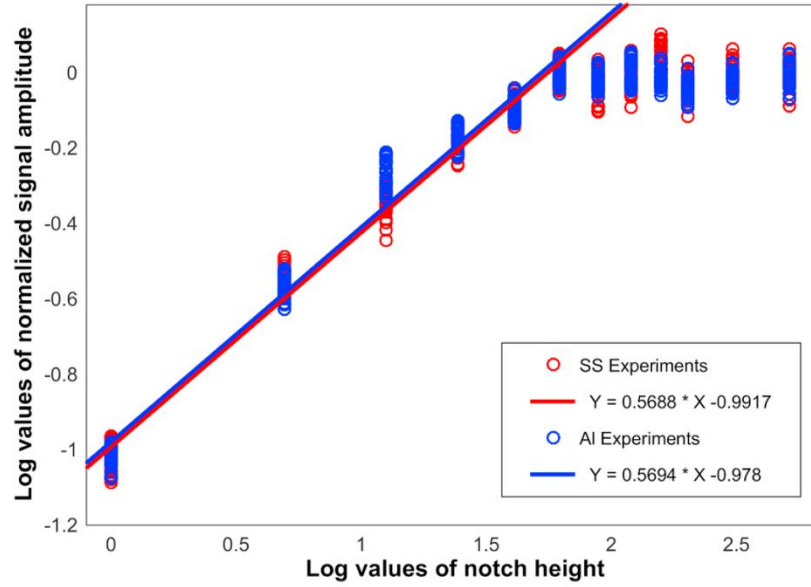
Figure 7. $Log(\hat{a})$ vs. $log(a)$ plot where $\hat{a}$ is the normalized signal amplitude (can be any defect response) and a is the notch height (can be any defect type) [14].

The PoD curves were validated by an experiment using the UT pulse-echo method on a structural steel plate [34]. Twelve notches were created in the plate and the excitation signal consisted of a 3 cycle Hanning windowed tone burst. Before the PoD curves were created, the linearity of $log(\hat{a})$ vs. $log(a)$ was confirmed and the final PoD results are shown in Figure 8 for the decision threshold of 15 times the signal noise amplitude. It shows that the probability of detection is about 100% for all notch heights passing 0.7 mm [34].
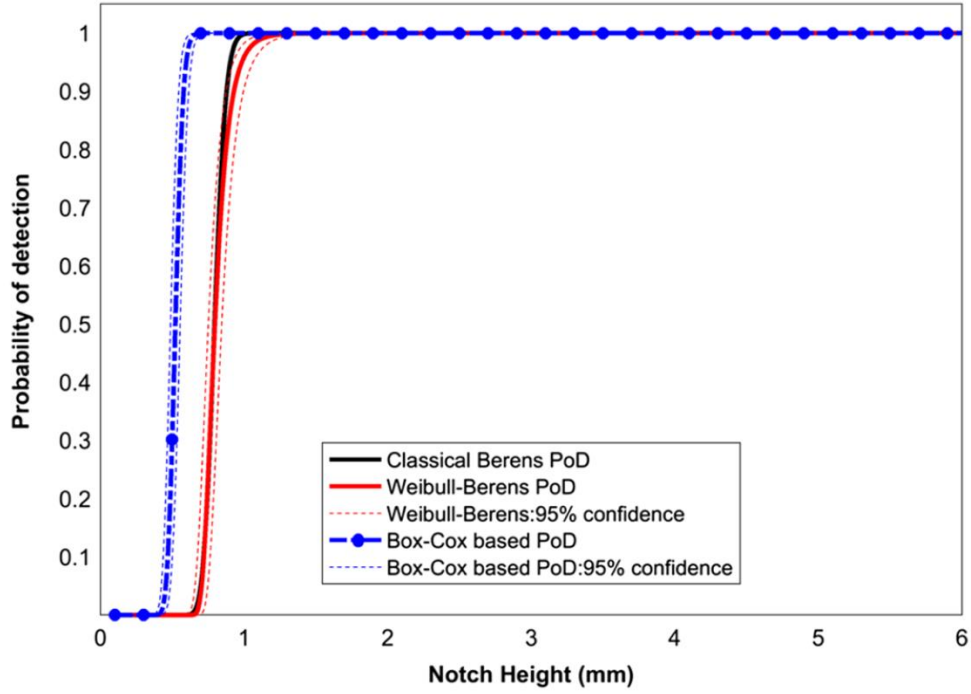
Figure 8. Comparison of multiple PoD curves for the chosen decision threshold [34].

Guan et al. investigated a systematic method to predict structural fatigue life of a steam turbine using NDE data [35]. They used a PoD model that compared recorded flaw size with the actual size. In addition, a probability of failure curve depending on fatigue life was developed to predict the fatigue life after a certain number of cycles. This is useful especially in aerospace structures, where any maintenance could be made before significant damage occurs. Virkkunen et al. compared the two typical PoD methods as mentioned earlier, for an aerospace eddy-current inspection and nuclear industry ultrasonic weld inspection [36]. It was found that the eddy-current inspection hit/miss analysis gave acceptable results and even small cracks were detected. The $\hat{a}$ vs. a method was recommended for inspections. Ali et al. experimented with PoD curves for materials with different signal to noise ratios. Materials with a low signal to noise ratio were

difficult to analyze with UT since the higher the signal noise, the more possible errors there were [14]. The experiment used a thick aluminum plate to conduct bulk UT inspection. The results showed that the PoD curves were within a 95% confidence level so it was concluded that they could be used to detect the notch height in the material. However, this method was limited to specific crack configurations and material types. Pilyugin and Lunin tested for flaws in a weld joint using an acoustic phased array [37]. PoD curves were calculated for 50%, 90% and 90% (confidence interval of 95%) and the results showed that a crack length of 1.056 mm could be detected at a 95% confidence interval, which suggested acceptable results that should still be validated with more experiments.

Therefore, PoD curves are important tools for determining the reliability of NDE methods and data. They are mostly used for predicting fatigue life and crack size after a certain number of cycles. This is especially beneficial for large structures that can be repaired early if fatigue crack conditions are known. PoD curves were not rigorously used in this research, but some beginning work is presented in Section 5.3. Further research must be done to choose the right decision threshold to predict crack detection.

3. NUMERICAL EVALUATION OF FATIGUE CRACK AND ULTRASONIC RELATIONSHIP

3.1 Introduction

In this chapter, the crack growth rate calculations, specimen geometry and numerical model results from the COMSOL Multiphysics software are presented. A modified version of the ASTM E647 compact tension specimen [38] was created, and the material used was structural steel. It was vital for the steel geometry to have a notch to ensure a fast crack growth rate in that high-stress area. In COMSOL, this damage was reflected in the y-displacement values that came from the ultrasonic waves. This was used to demonstrate fatigue crack detection with *in-situ* phase-arrayed ultrasonic sensors. Stress checks in COMSOL were completed along with bearing strength calculations to ensure that there would be no premature failure in the loading zones, and that the crack would form at the notch tip first.

3.2 Sample Design for Fatigue Testing

An idealized test specimen was designed so that the fatigue crack's length reached 10 mm in 6-8 hours of testing using the Instron machine at the University of Illinois at Chicago laboratory. In Section 2.3.2, the previous geometry of a similar project that tested an idealized spline section of a gearbox using AE and UT arrays was reported. In this research, that geometry was modified, and an array of ultrasonic sensors was used to detect the fatigue crack from one position. The number of cycles and time to reach the desired 10 mm crack was calculated.

From Seitl et al. [39], and considering a constant amplitude fatigue loading, the crack growth rate was characterized by K_{min} and K_{max} as:

$$\frac{da}{dN} = f_1(\Delta K, R) \tag{3.1}$$

$$\Delta K = K_{max} - K_{min} \tag{3.2}$$

$$R = K_{min}/K_{max} \tag{3.3}$$

where $\frac{da}{dN}$ is the crack growth per cycle, ΔK is the stress intensity range and R is the ratio of minimum to maximum stress intensity factors. The number of fatigue cycles for crack to grow from initial length to a final length is:

$$N = \int_{a_o}^{a_f} \frac{da}{f_1(\Delta K, R)} \tag{3.4}$$

The linear region of log-log curve of fatigue is represented by a power law as:

$$\frac{da}{dN} = C\Delta K^m \tag{3.5}$$

where C and m are material constants determined experimentally. From ASTM E647-15 [38], the stress intensity factor for compact tension specimen is:

$$K_I = \frac{P}{B\sqrt{W}} f\left(\frac{a}{W}\right) \tag{3.6}$$

where

$$f\left(\frac{a}{W}\right) = \frac{2 + \frac{a}{W}}{\left(1 - \frac{a}{W}\right)^{3/2}} \left[0.886 + 4.64\left(\frac{a}{W}\right) - 13.32\left(\frac{a}{W}\right)^2 + 14.72\left(\frac{a}{W}\right)^3 - 5.6\left(\frac{a}{W}\right)^4\right] \tag{3.7}$$

In equations 3.6 and 3.7, P is the load, B is the specimen thickness, W is the specimen width and a is the notch length.

Figure 9 and Figure 10 show a comparison of the CT specimen from ASTM E647 [38] and the modified version used for the numerical simulations. The specifications of the modified CT specimen including the geometric and loading properties are shown in Table VI below.
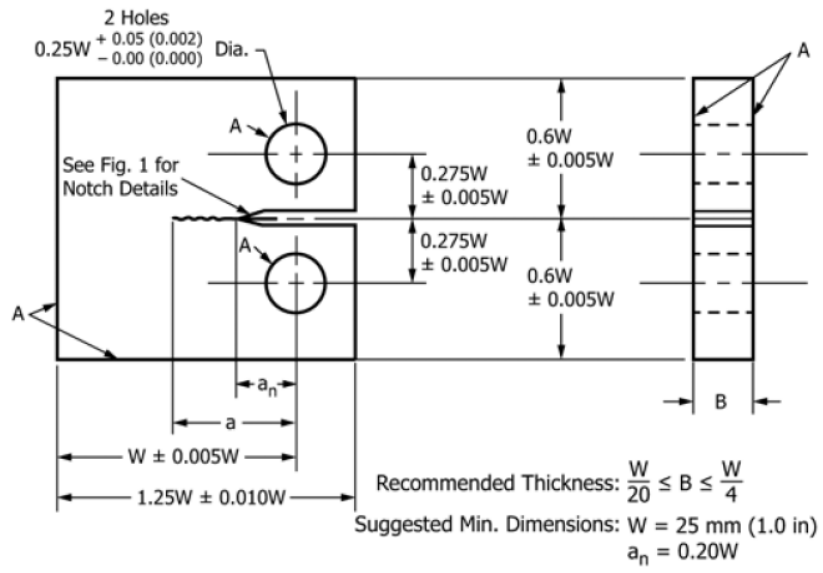
Figure 9. ASTM E647 compact tension specimen [38].
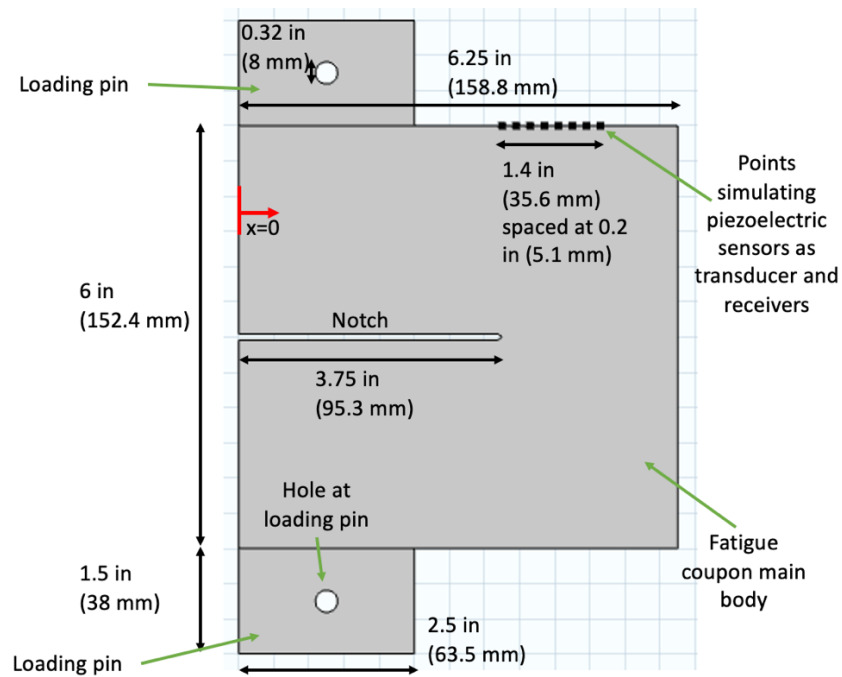
Figure 10. The modified CT geometry.

Table VI: CT SPECIMEN SPECIFICATIONS

Property	*Physical Value*	*Calculated Value*
Specimen thickness B	0.5" (0.0127 m)	-
Specimen width W	6.25" (0.159 m)	-
Notch length, a	3.75" (0.0953 m)	-
Max load P_{max}	13 kN	-
Min load P_{min}	1.8 kN	-
f fatigue frequency	4 Hz	-
R ratio	-	0.139
K_{max} calculated	-	$35.08\ MPa - m^{1/2}$
K_{min} calculated	-	$4.86\ MPa - m^{1/2}$
ΔK calculated	-	$30.22\ MPa - m^{1/2}$

The relationship between ΔK and $\frac{da}{dN}$ for steel is extracted from the study by Seitl et al.

[39] as shown in Figure 11. For $\Delta K = 30.22\ MPa - m^{1/2}, \frac{da}{dN}$ is approximately

$1E - 04\ mm/cycle$. Reaching the 10 mm crack length requires $\frac{10}{1E-04} = 100,000\ cycles$.

Assuming the cyclic frequency as 4 Hz, the total experimental duration is $\frac{100,000}{4} = 25,000\ s =$

$7\ hr$.
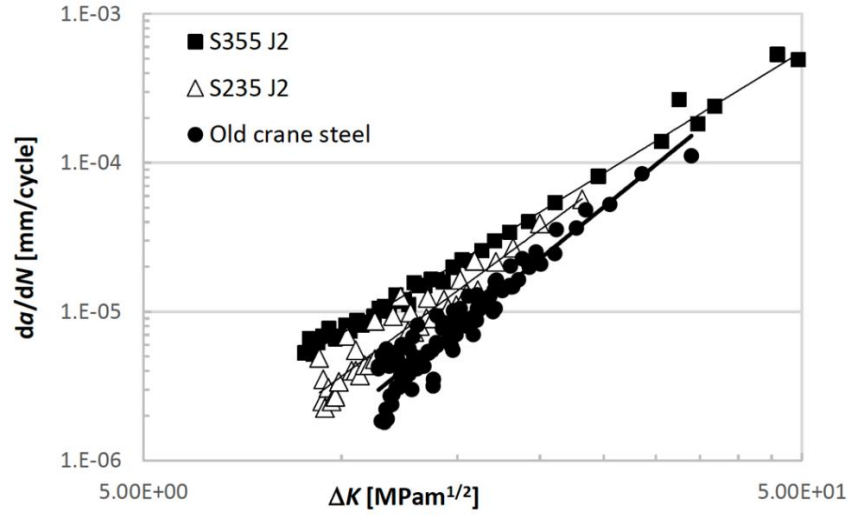
Figure 11. Fatigue crack growth curves for S355J2, S235J2 and old crane way steel from Seitl et al. [39].

After the geometry and time to grow the desired crack were known, static and dynamic two-dimensional models of the modified CT sample were created in the COMSOL Multiphysics software. The software was chosen because it allowed the combination of multiple physics to simulate real world phenomena [40]. The solid mechanics physics was used for both the static and dynamic models since the deformation under different loadings was analyzed. The static model used a stationary study for the steady-state condition to determine the stresses and volumetric plastic strain at the notch tip and loading pin holes. The dynamic models used a time-dependent study for seven different crack lengths.

35

3.3 Static Model in COMSOL Multiphysics

First, the static numerical model was built. It was approximated as a two-dimensional plain strain model with a thickness of 0.5" (12.7 mm). The overall geometry and constraints are shown in Table VII and Table VIII, which coincide with Figure 10.

Table VII: DIMENSIONS OF CT SPECIMEN

Component	*Property*	*Value*
Fatigue coupon main body	Width	6.25" (158.8 mm)
	Height	6" (152.4 mm)
	Thickness	0.5" (12.7 mm)
Loading pins	Width	2.5" (63.5 mm)
	Height	1.5" (38 mm)
	Thickness	0.5" (12.7 mm)
Holes at loading pins	Diameter	0.32" (8 mm)
Notch	Length	3.75" (95.3 mm)

Table VIII: CONSTRAINTS OF CT SPECIMEN

Constraint	Value
Sensor spacing	0.20" (5.08 mm)
Thickness of specimen where sensors will be placed	0.50" (12.7 mm)
Maximum crack length	0.40" (10 mm)

Starting from the notch tip, eight points located at the top surface of the model, spanning 1.4" (35.6 mm) and separated by 0.2" (5.1 mm) were defined as the measurement points simulating the piezoelectric sensors as the transmitter and receivers as shown previously in Figure 10. Table IX defines the "sensor" position relative to the left side of the specimen.

Table IX: SENSOR POSITIONS RELATIVE TO LEFT SIDE OF SPECIMEN

Sensor Number	Position, inch (mm)
1 (transmitter)	3.75 (95.25)
2	3.95 (100.3)
3	4.15 (105.4)
4	4.35 (110.5)
5	4.55 (115.6)
6	4.75 (120.7)
7	4.95 (125.7)
8	5.15 (130.8)

The entire CT specimen was first assigned an isotropic, linear elastic structural steel material. Once the stress results were obtained then the model was assigned a plasticity property to find the volumetric plastic strain. The isotropic tangent modulus was taken as 0.5% of Young's Modulus. The material defined by COMSOL had the following properties shown in Table X.

Table X: STRUCTURAL STEEL MATERIAL PROPERTIES OF CT SPECIMEN

Property	Value
Density	7850 kg/m^3
Young's Modulus	200 GPa
Poisson's Ratio	0.33
Plasticity Model Material Properties	
Initial Yield Stress	345 MPa
Isotropic Tangent Modulus	1 GPa

For the linear elastic analysis, all the boundaries were assigned as free, and the initial values included zero displacement fields in all directions. A prescribed displacement of 0" in the x-direction was assigned to the bottom loading pin hole. It was also assigned in the x- and y-directions to the top loading pin hole to allow only the bottom loading pin to displace in the y-direction. These y-displacements were recorded later in the dynamic models and used to calculate the DI. A downwards boundary load of 12 kN was applied to the bottom half of the

bottom hole. The plasticity material model was assigned to check that the stress at the notch was higher than the stresses at the loading pin holes without having any plastic deformation and that the fatigue crack would form at the notch tip.

3.3.1 Mesh Convergence for Static Model

To obtain accurate stress results from the static model, a mesh convergence study was conducted with properties and different mesh sizes as shown in Table XI and Figure 12, respectively. COMSOL allows the user to build a custom mesh which was chosen over the automatic physics-controlled mesh since the size could be changed in case of any inaccuracies. For this model, the mesh study was conducted using the von Mises stresses for the notch tip. As clearly shown in Figure 12b, the stress values agreed when the maximum and minimum mesh sizes were: $dx * 1$ and $dx * 1$ as well as $dx * 1$ and $dx * 0.75$. Since COMSOL Multiphysics had problems with memory when the mesh size multiplier was less than 1, the final mesh size chosen was $dx * 1$ and $dx * 1$. The convergence study was only conducted for the 400 kHz frequency, even though other frequencies were used for the numerical simulations. This is because the wave traveled with velocity, v, so the mesh was proportional to that.

Table XI: MESH PROPERTIES

Property	Equation	Value
Velocity, v	-	5000 m/s
Frequency, $Freq$	-	400 kHz
Change in time, dt	$dt = \dfrac{1}{10}/Freq$	0.25 μs
Mesh size, dx	$dx = v * dt$	5 mm
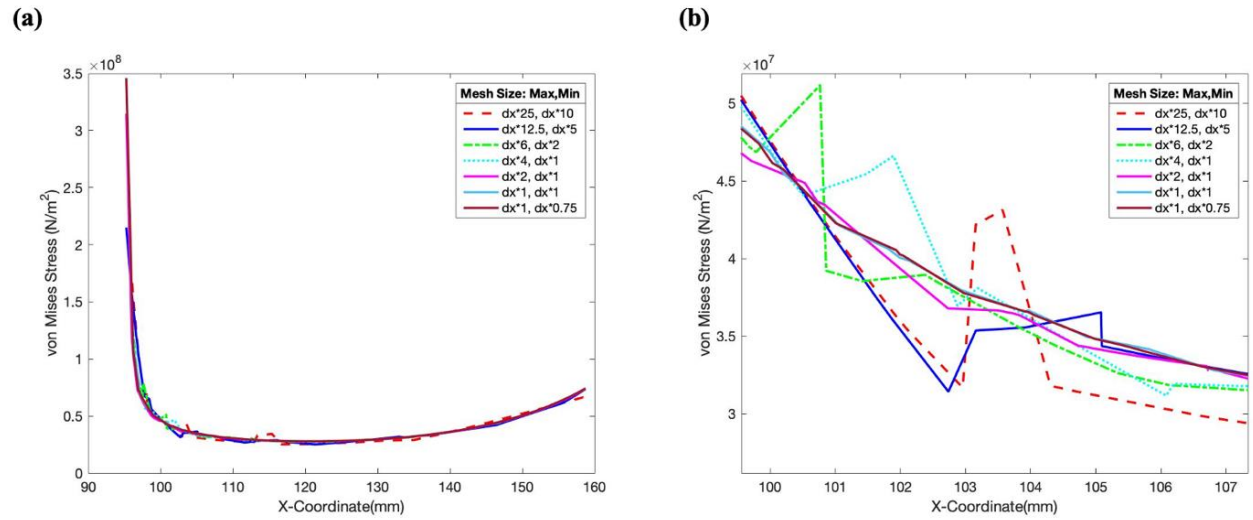
Figure 12. Example of static mesh study (a) completed on the notch von Mises Stresses and (b) zoomed in to the area with the most differences between mesh sizes.

3.3.2 Static Model Numerical Results

The static model simulation provided information about the von Mises stresses and volumetric plastic strain in the entire CT specimen, while focusing on the notch tip and the loading pin holes. The data was processed directly in COMSOL since it was capable of plotting stresses for arc lengths. The stresses were calculated along the notch tip and through the top and bottom holes. A schematic of this is shown in Figure 13. Figure 14 shows the two-dimensional surface plot of the von Mises stresses for the entire CT specimen, the notch and the holes at the loading pins. These stresses were compared to the endurance limit of steel which is about 30 ksi (207 MPa) as presented in Figure 15.
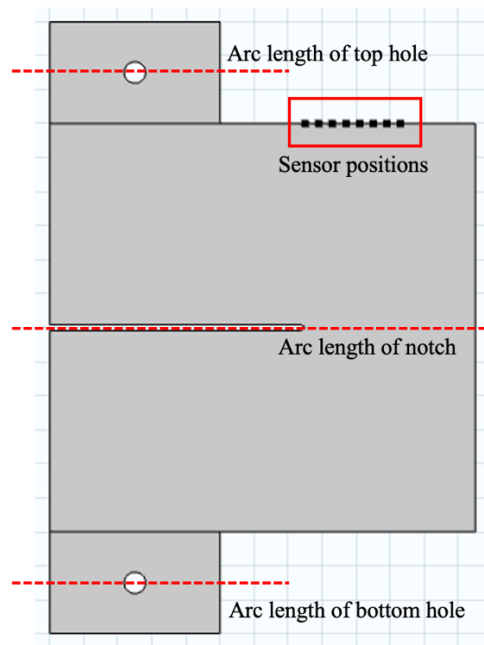
Figure 13. Geometry of sample and locations of vital arc lengths where the stresses were calculated.
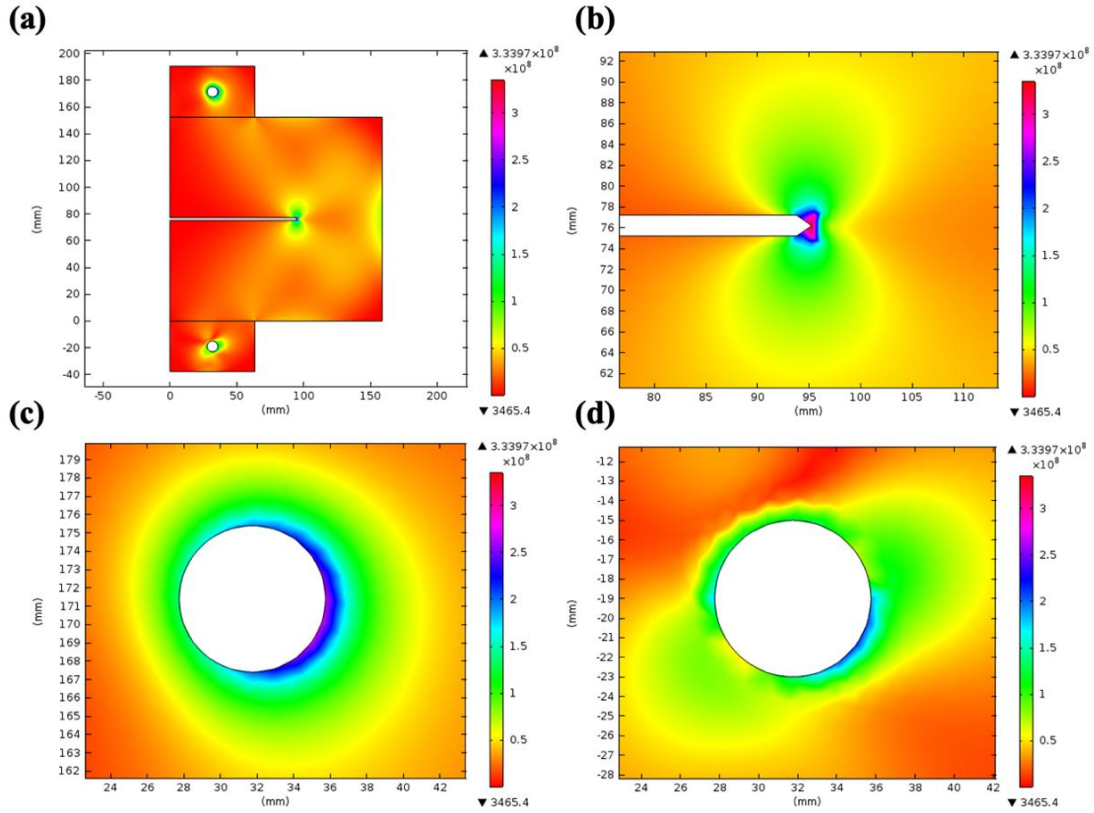
Figure 14. von Mises stress (N/m^2) for (a) entire CT specimen, (b) zoomed in to notch tip, (c) zoomed in to top hole at loading pin and (d) zoomed in to bottom hole at loading pin.
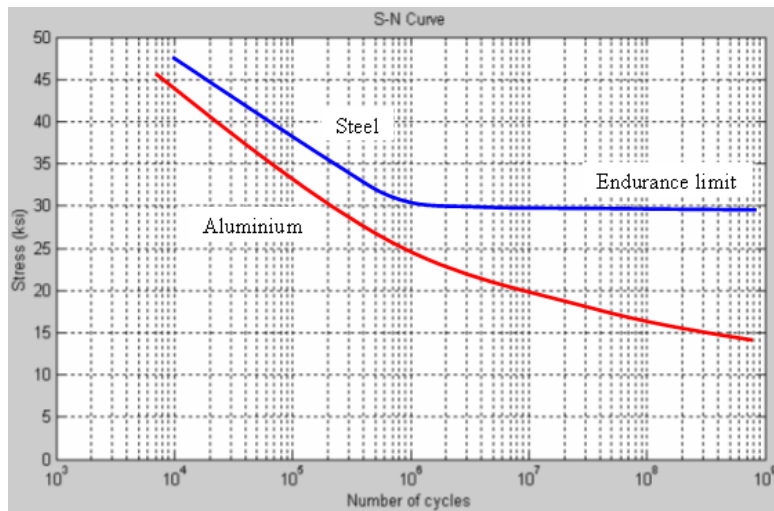
Figure 15. Endurance limit of steel compared with aluminum [41].

It was verified that the highest stress at the notch tip was about 340 MPa as shown in Figure 16a while the highest stress at the top hole was approximately 210 MPa as shown in Figure 16b, which was expected since the notch area is smaller. Therefore, since the stress around the loading pin holes are at the boundary of steel's endurance limit and the stress at the notch was larger, no crack was expected to form at the loading pin holes before the fatigue crack at the notch tip started to grow. The overall purpose of this model was to ensure that the von Mises stresses at the notch tip were above the endurance limit of steel, which is about 30 ksi (207 MPa) and that the fatigue crack would form at the notch tip.
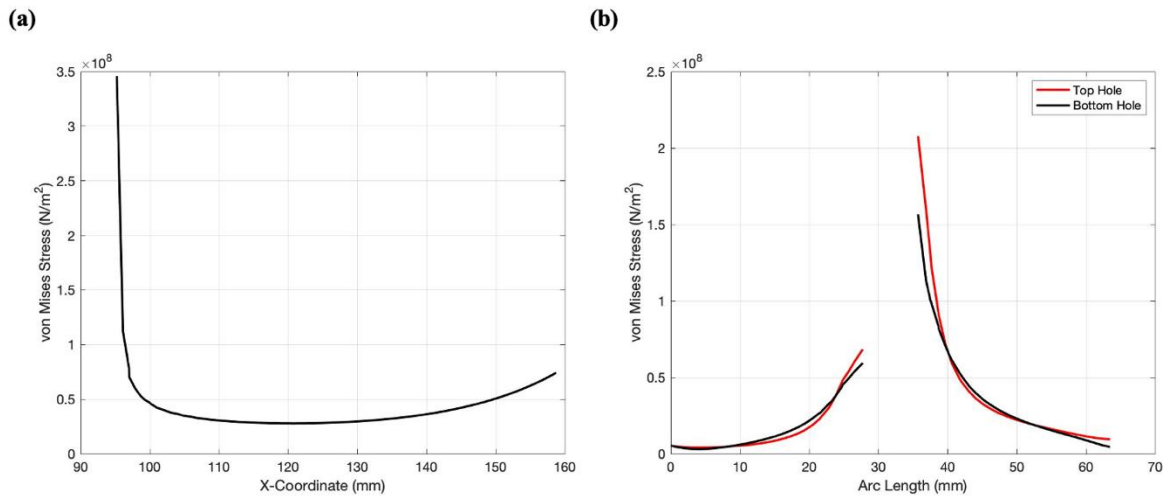
Figure 16. von Misses stresses along (a) notch and (b) holes at loading pins.

The model also introduced a plasticity model to check the volumetric plastic strain and ensure that the stress values at the holes did not exceed the yield point. The initial yield stress and isotropic tangent modulus were defined for this model as shown in Table X. The maximum

volumetric plastic strain at the notch tip was 1.35E-20 (unitless) as shown in Figure 17 while the

holes at the pins stayed elastic. This model confirmed that there was no plastic deformation.
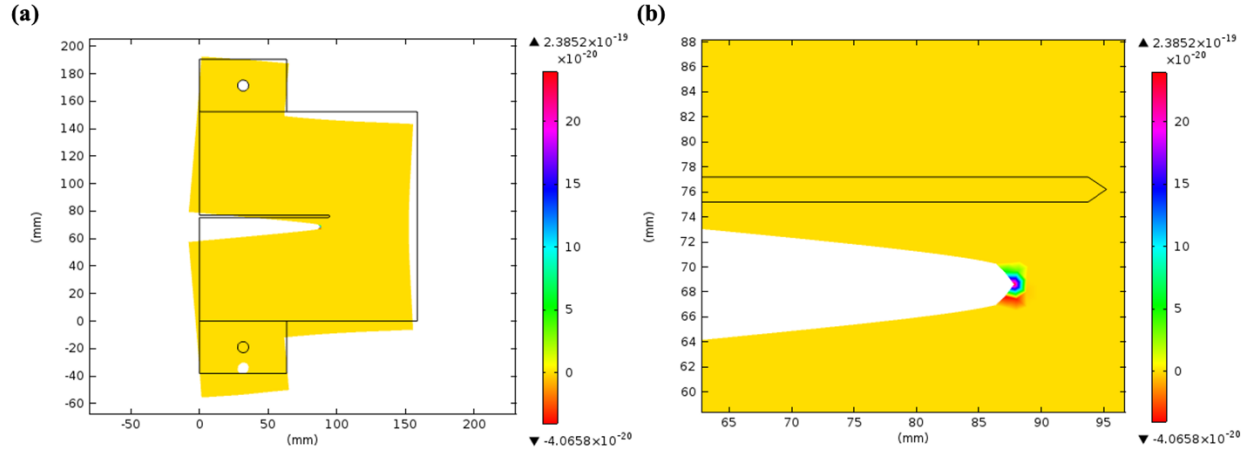
Figure 17. Surface volumetric plastic strain for (a) entire CT specimen and (b) notch tip.

Since the holes at the loading pins acted as "bolt holes" that carry shear loads, the bearing

strength was also calculated to ensure that the holes would not experience bearing failure. The

bearing strength per bolt is:

$$r_n = 2L_c t \tau_u^{plate} \approx 1.2 L_c t F_u^{plate} < 2.4 d_{bolt} t F_u^{plate} \tag{3.8}$$

where L_c is the clear distance from the free end to the bolt, t is plate thickness and τ_u^{plate}

is the ultimate shear strength of the plate $= 0.625 F_u^{plate}$, according to Chapter J, Part 16-1,

Section 10 of the American Institute of Steel Construction Manual [42]. This was used assuming

a standard bolt type, short-slotted holes and with deformation considered in the design.

The Load and Resistance Factor Design (LRFD) equations comparing the nominal strength to design strength for a bolt of simple connection is:

$$n\phi r_n \geq P_u \qquad (3.9)$$

where n is the number of bolts, ϕ is the resistance factor (0.75 for bearing), r_n is the nominal strength of one bolt and p_u is the factored load per bolt $= \frac{P_u}{n}$ according to Chapter J, Part 16-1, Section 10 of the American Institute of Steel Construction Steel Construction Manual [42]. The bearing strength calculations are shown in Table XII below.

Table XII: BEARING STRENGTH PARAMETERS AND CALCULATIONS

Property	*Physical Value*	*Calculated Value*
F_u^{plate}	65 ksi (448 MPa) [43]	-
t	0.5" (12.7 mm)	-
L_c	0.59" (15 mm)	-
n	1	-
d_{bolt} or d_{hole}	0.31" (8mm)	
ϕ	0.75	-
r_n	-	23.0 kips (102.3 kN)
$2.4 d_{bolt} t F_u^{plate}$	-	24.2 kips (107.6 kN)
$n\phi r_n$	-	17.3 kips (76.9 kN)
P_u	-	2.7 kips (12.0 kN)
p_u	-	2.7 kips (12.0 kN)

From Equations 3.8 and 3.9, it can be seen that $23.0 \, kips < 24.2 \, kips$ and $17.3 \, kips \geq$ $2.7 \, kips$, respectively. The requirements are met which means that the bolt will not endure bearing failure. This result was desired since the crack should form at the notch first.

3.4 Numerical Model for Ultrasonic Simulation

The dynamic models were built to test different excitation frequencies and their sensitivities to different crack lengths at the sensing points. The frequencies tested were 400 kHz and 300 kHz, while the crack lengths assessed were 0 mm, 1 mm, 2 mm, 3 mm, 5 mm, 7 mm and 10 mm. It was important to test a higher frequency because if it was too low, the wavelength would increase and therefore would become less sensitive to changes in the structure, including damage.

A total of seven dynamic models were created using the fatigue coupon. The geometry stayed the same between the static and dynamic models while only the crack length changed. The excitation waveform was created in MATLAB by defining the frequency, number of cycles, time information and window function. The Hilbert transform was used to form an analytic signal to find characteristics of time domain data [44]. The result was a 4 cycle sinusoidal wave, sine shape, tested at the central frequencies of 400 kHz and 300 kHz as shown in Figure 18.
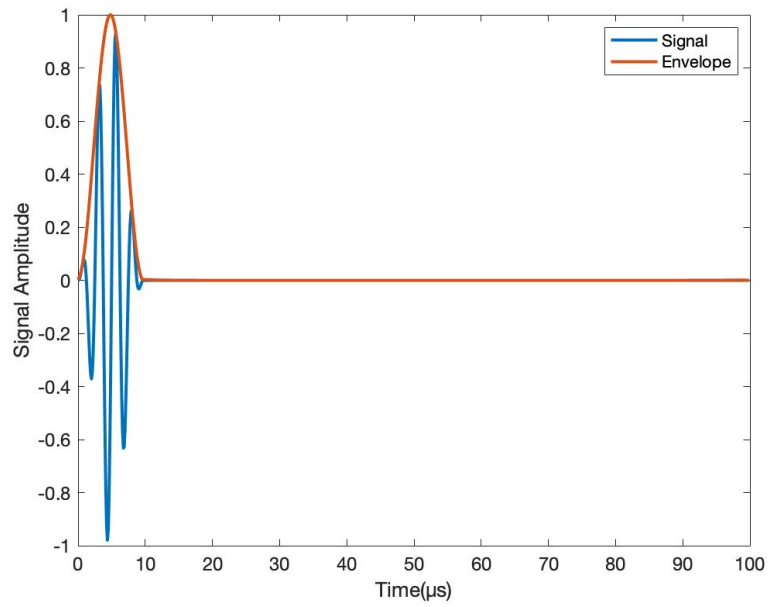
Figure 18. Excitation signal created in MATLAB.

This load was applied to the point closest to the notch tip (referred to as end load) as a point load, as shown in Figure 19. This simulated the location of the transmitter. The maximum crack dimensions are detailed in Figure 20.
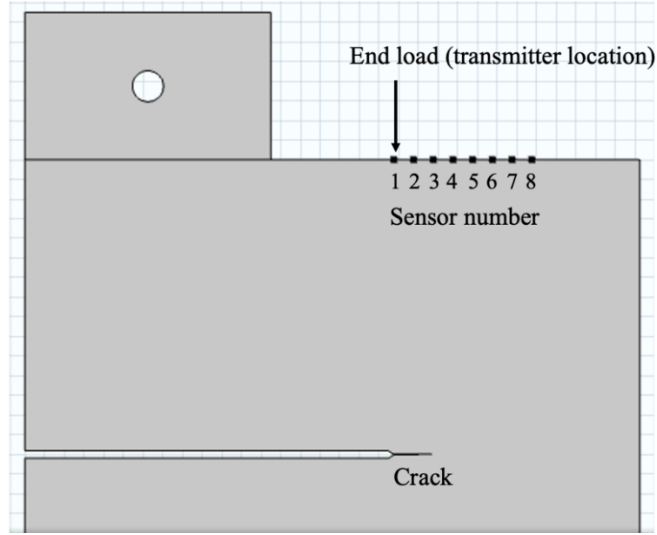
Figure 19. Dynamic loading point.
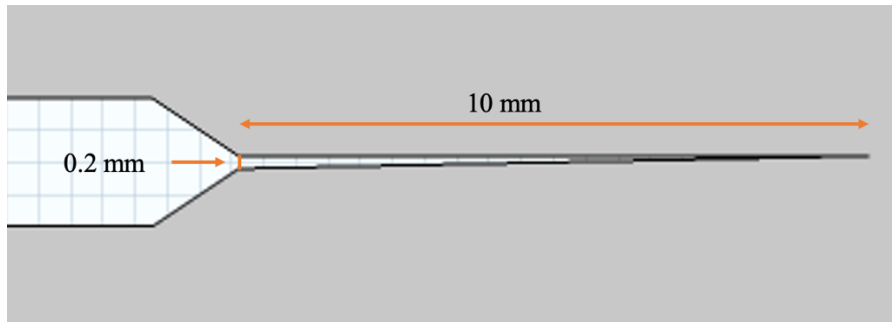
Figure 20. Crack dimensions.

The time-dependent study was performed over the entire domain. The y-displacements were extracted from the model by completing a point evaluation at each of the seven receiver points (sensor 2 through 8), which were used to develop plots of damage index vs. crack length and damage index vs. sensor. Late arrival signals located around 30 μs hold important crack-

related information because that was the first expected arrival time from the crack position, as calculated in Table XIII. A schematic is also shown in Figure 21.

Table XIII: ARRIVAL TIME PARAMETERS

Property	*Equation*	*Value*
Velocity, v	-	5000 m/s
Fatigue coupon main body height, h	-	6" (152.4 mm)
Distance to notch, d	$d = \dfrac{h}{2}$	3 inch (76.2 mm)
Arrival time, $t_{arrival}$	$t_{arrival} = \dfrac{d * 2}{v} * 10^6$	30.48 µs
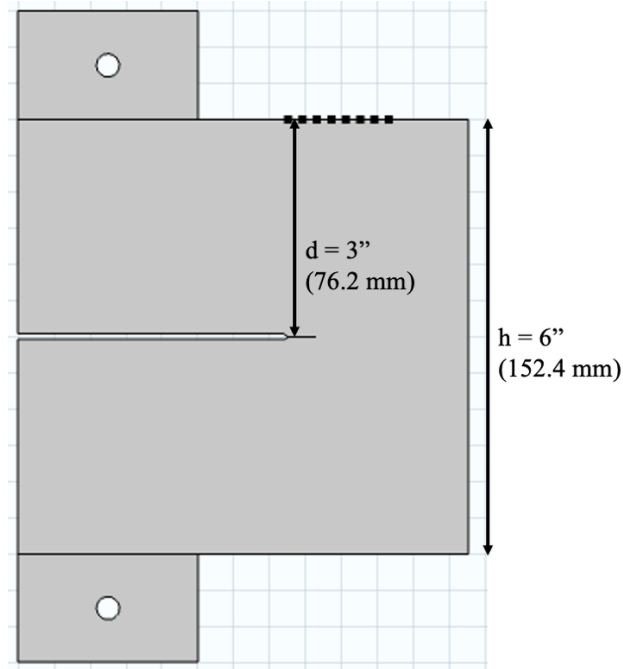
Figure 21. Schematic of arrival time parameters.

3.4.1 Mesh Convergence for Dynamic Model

To obtain accurate y-displacement results from the dynamic models, a mesh convergence study was conducted with different mesh sizes. The amplitudes of the surface wave arrivals at sensor 2 were compared to finalize the mesh size. It was determined that the mesh converged when the initial arrival surface wave amplitudes were the same for each crack length. The y-displacement was not expected to change for the first surface wave no matter the crack size because the wave only travels on the surface and does not interact with the different crack lengths. The same mesh properties used from the static model applied to the dynamic models which were shown earlier in Table XI.

50

The convergence study consisted of testing the maximum and minimum element sizes until acceptable results were obtained. Figure 22 shows the different mesh sizes tested and the results of the convergence study. The displacement field (y-component) became consistent when the maximum mesh size was $dx * 1$ and the minimum mesh size was $dx * 1$. As the mesh sizes became even smaller, the same results were obtained. Therefore, the final mesh size chosen was $dx * 1$ and $dx * 1$ since COMSOL had memory problems with smaller mesh sizes. Figure 23a shows an example of the initial surface wave arrival varying with different crack lengths. For example, at 6.75 µs, the y-displacement is 3.18E-07 mm at the 7 mm crack, but at the 3 mm crack, the y-displacement is 3.05E-07 mm. These values should be the same, which is the case for Figure 23b. Figure 23b clearly shows the crack signal at around 30 µs, but this is not visible at all in Figure 23a.
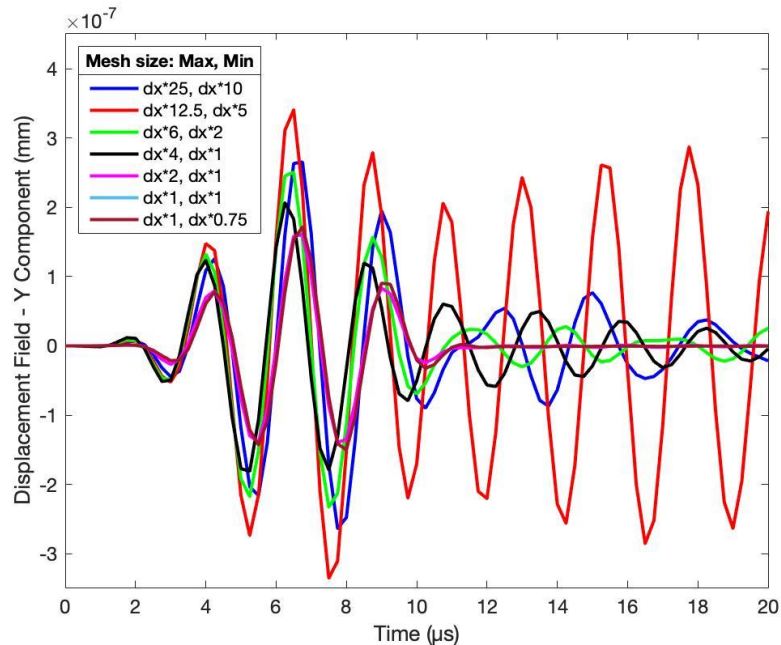
Figure 22. Example of static mesh study completed for sensor 2 at 400 kHz and 1 mm crack size.

51
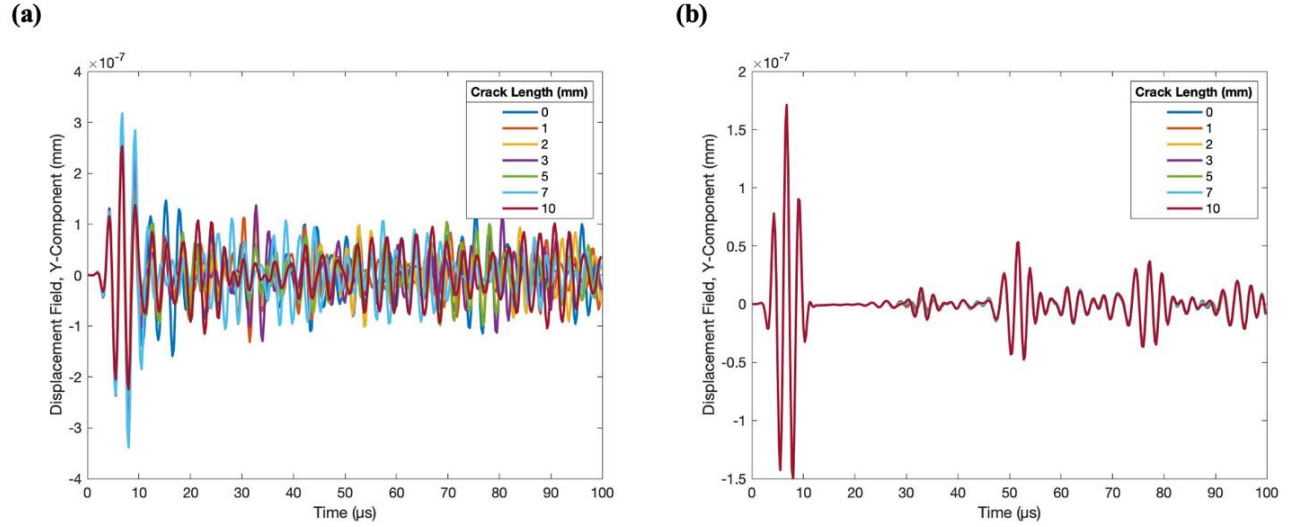
Figure 23. Waveform for sensor 2 at a 400 kHz frequency with maximum and minimum mesh size as (a) $dx * 25$ and $dx * 10$ and maximum and minimum mesh size as (b) $dx * 1$ and $dx * 1$.

3.4.2 The Correlation of Ultrasonic Data with Fatigue Crack Length

The damage index can be used to characterize the crack length, identify crack propagation, monitor fatigue crack growth, determine crack length and visualize the correlation of ultrasonic data related to crack length and distance from excitation signal [3]. The most critical ultrasonic wave features are amplitude and wave energy [3] which is why most of the DI equations in Table XIV are based on amplitude and energy. Equations 1-7 were obtained from Yan et al. because they were made for one actuator-sensor pair and guided waves were used for a steel specimen, which is similar to this research [3]. Equations 8 and 9 were new since they referenced the surface wave instead of the crack-free baseline condition. In addition to amplitude and energy-based DIs, frequency and phase shift-based DIs were used to see if there were any correlations between them and the classic amplitude/energy DIs. All the considered DI equations are shown in Table XIV.

52

Table XIV: DAMAGE INDEX EQUATIONS

DI Number	Equation	Description
1	$DI_1 = |A_{m1} - A_{m2}|/A_{m1}$	Amplitude-based
2	$DI_2 = \ln A_{m2}/A_{m1}$	Amplitude attenuation-based
3	$DI_3 = \sqrt{\int [f_{m2}(t) - f_{m1}(t)]^2 \, dt / \int [f_{m1}(t)]^2 \, dt}$	Root mean square deviation-based
4	$DI_4 = (\int |f_{m1}(t)|^2 \, dt)/(\int |f_{m2}(t)|^2 \, dt)$	Energy-based
5	$DI_5 = (\int |f_{m1}(t) - f_{m2}(t)|^2 \, dt)/(\int |f_{m1}(t)|^2 \, dt)$	Energy-based
6	$DI_6 = |\int [f_{m2}(t)]^2 \, dt - \int [f_{m1}(t)]^2 \, dt|/(\int [f_{m1}(t)]^2 \, dt)$	Energy-based
7	$DI_7 = (\int |f_{m1}(t)|^2 \, dt - \int |f_{m2}(t)|^2 dt)/(\int |f_{m2}(t)|^2 \, dt)$	Energy-based
8	$DI_8 = \left|\dfrac{A_{2n}}{A_{1n}}\right|$	Amplitude-based
9	$DI_9 = \left|\dfrac{E_{2n}}{E_{1n}}\right|$	Energy-based
10	$DI_{10} = A_{2n}/A_{1n}$	Frequency amplitude-based
11	$DI_{11} = A_{2n}$	Frequency amplitude- based
12	$DI_{12} = 1 - |r|$	Phase shift-based (Signal difference coefficient)
13	$DI_{13} = \dfrac{\Delta t}{t_o} = \dfrac{\Delta \phi(f)}{2\pi f d/v_o}$	Phase shift-based (Relative time delay) [45]
14	$DI_{14} = F_{2n}/F_{1n}$	Frequency-based

$A_{mn}, f_{mn}(t), E_{mn}$ and F_{mn} are the maximum amplitude of the signal, current signal, energy and frequency corresponding to the maximum amplitude in the frequency spectra. The subscripts m and n refer to the window within one signal or waveform (based on the different crack lengths) and the waveform within one window, respectively. When $n = 1$, this always references the baseline signal (0 mm crack length) and when $n = 2$, this references any other signal where the crack length is larger than zero. When $m = 1$, this refers to the time window for the first surface arrival wave. When $m = 2$, any other time window can be used; in this case the window with the crack arrival time from the notch tip was used. A schematic is shown in Figure 24. In DI_{12}, r is the Pearson correlation coefficient. In DI_{13}, $\frac{\Delta t}{t_o}$ is the relative time delay, d is the distance between the transmitter and receiver, f is the peak frequency and $\Delta\phi(f)$ is the phase shift in the signal's frequency spectrum [45].
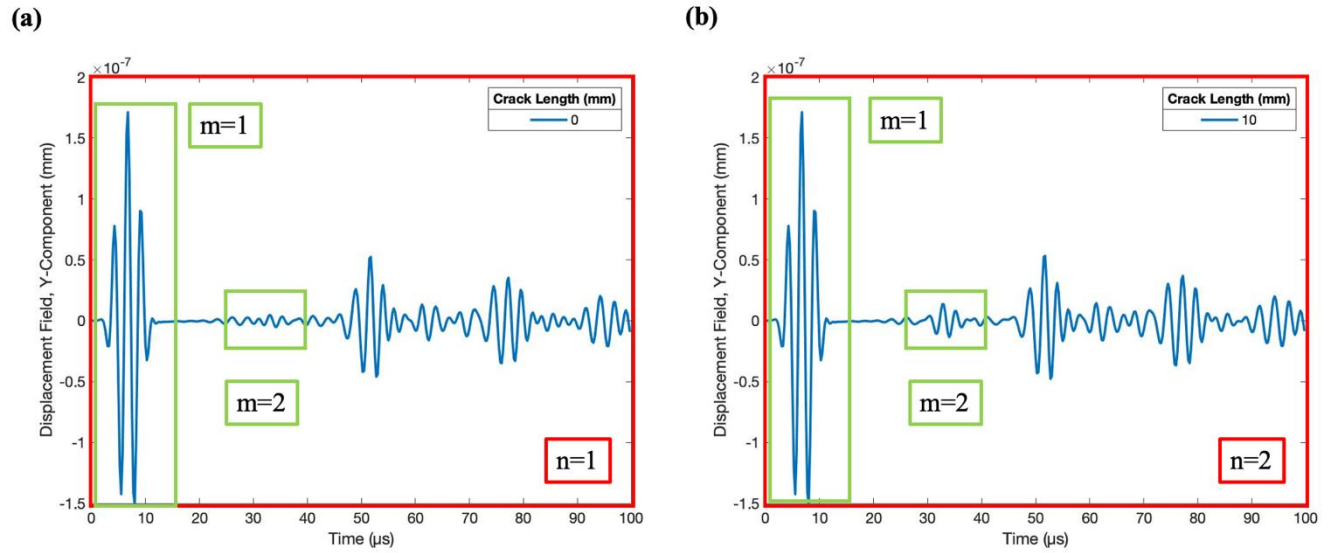

Figure 24. Example of (a) 0 mm crack waveform and (b) 10 mm crack waveform with subscripts m and n defined.

DI_1 through DI_7 reference the baseline crack-free condition while DI_8 through DI_{10} and DI_{14} reference two time periods within the same waveform by using two signal envelopes. They are the first surface arrival wave and the first crack arrival. In general, DI_1 through DI_7 are expected to increase as the crack length increases. This is because the amplitude and subsequently energy of the crack arrival signal should increase as the crack length becomes larger, as demonstrated in Figure 25.

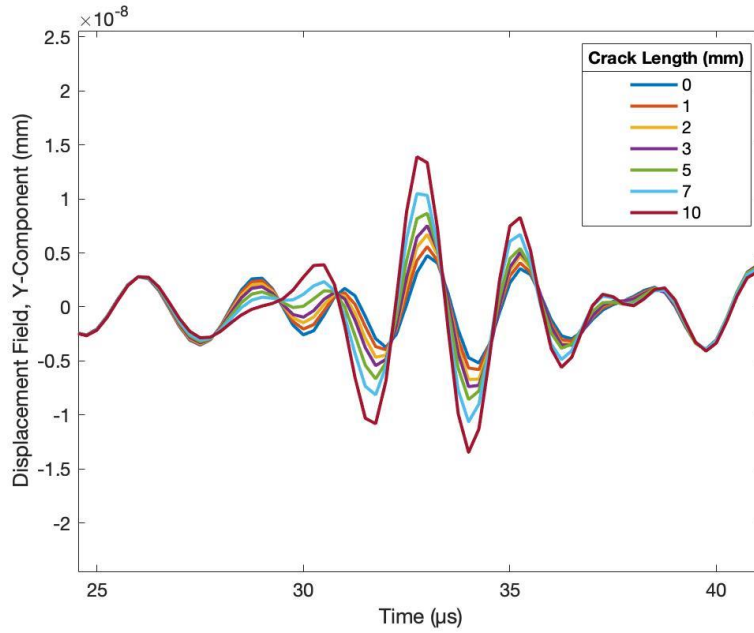Figure 25. Example of 400 kHz waveform for sensor 2 for all crack lengths at the expected time of arrival.

For DI_8 through DI_{10}, it is expected that the reflection from the crack tip would increase A_{2n} and E_{2n} relating to the surface wave arrival parameters, A_{1n} and E_{1n} as the crack length increases when sensors from further from the notch tip are analyzed. DI_{11} is also expected to

increase with crack length, as this is simply the maximum amplitude in the frequency domain

and it is expected to follow a similar trend as the maximum amplitude in the time domain. DI_{12}

should increase as well because as the sensor is located farther from the transmitter, r decreases

which makes the overall DI value larger. DI_{13} is expected to follow a similar trend if $\Delta\phi(f)$, or

the phase shift, increases. DI_{14} should also increase if the surface wave frequency is constant and

the frequency for the crack arrival signal increases slightly with crack length.

The equations from Table XIV were used to plot DI vs. crack length. The waveforms

were plotted first to determine the fundamental time window. The time window was based on

where the surface arrival signal ended and the crack arrival signal began, which was around 30

μs. The results in Figure 26 were calculated in the time domain at 400 kHz and were used to

characterize crack propagation. The damage index was plotted for sensors 2-8 since they were

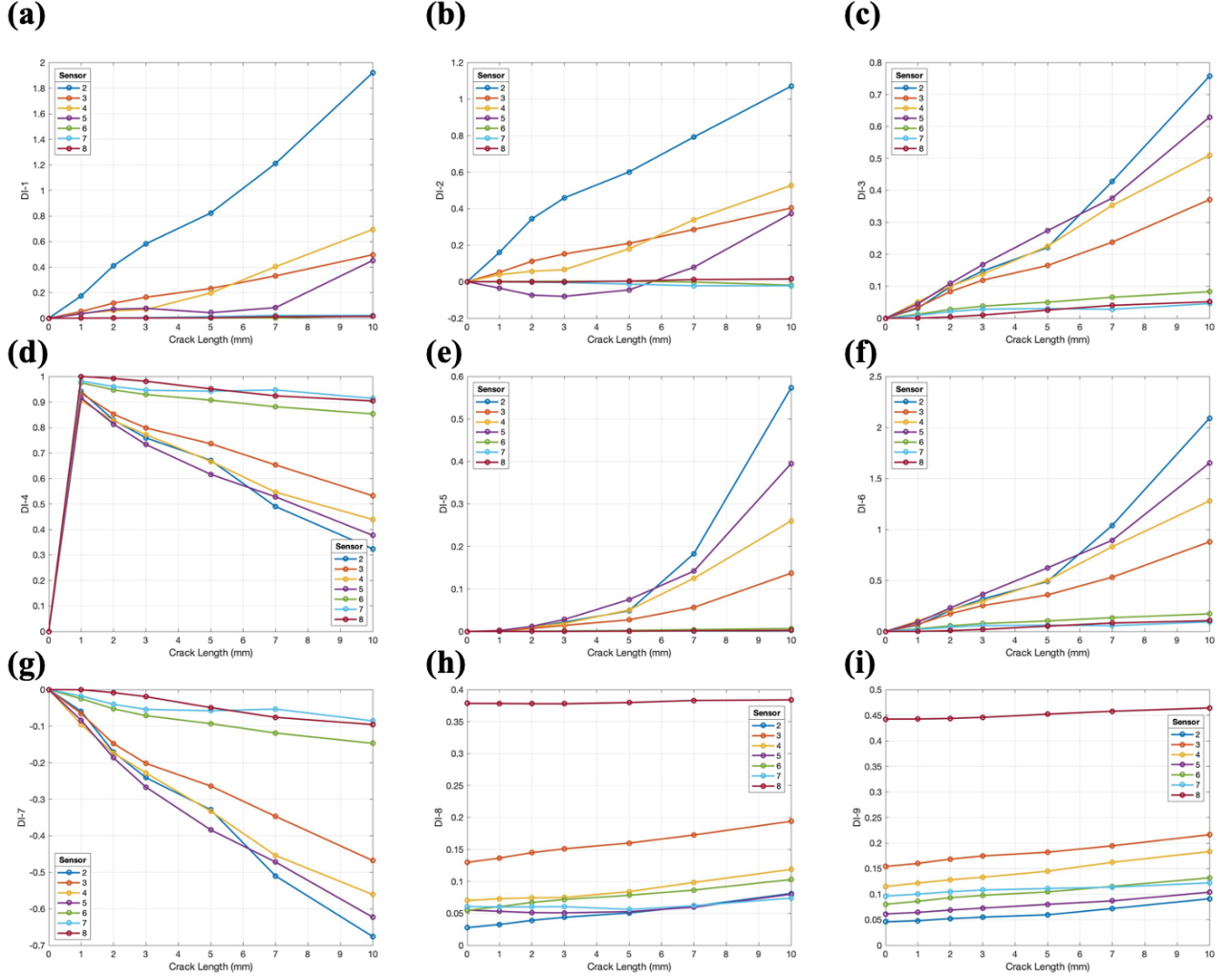the receivers and sensor 1 was the transmitter.

Figure 26. Damage index for sensors 2-8 at 400 kHz based on the different equations (a) DI_1 based on amplitude, (b) DI_2 based on amplitude attenuation, (c) DI_3 based on root mean square deviation, (d) DI_4 based on energy, (e) DI_5 based on energy, (f) DI_6 based on energy, (g) DI_7 based on energy, (h) DI_8 based on amplitude and (i) DI_9 based on energy.

From Figure 26, it can be seen that DI_1, DI_2, DI_3, DI_5, DI_6, DI_8 and DI_9 follow a similar trend where the DI increases as the crack length increases. This is also seen in Yan et al. [3] and Jin et al. [5], which was shown earlier in Section 2.3.1. DI_4 increases sharply up to the 1 mm crack, and then decreases rapidly. Since the calculated energy increased as the crack length

increased, the equation was set up so that the larger energies in the denominator make the overall damage index smaller, as the baseline signal is constant. The same explanation can be used for DI_7 because the damage index decreases as the crack length increases. However, this DI is also negative because the current signal with crack is being subtracted from the baseline signal, and the crack signal is always bigger. A similar trend was reported by Ushakov et al., where the crack depth could not be measured because the amplitude of the signal with the crack was larger than the amplitude of the signal without the crack [12].

From Figure 26, DI_1, DI_2, DI_3, DI_5 and DI_6 show that sensor 2 always had the largest DI. DI_8 and DI_9 show that sensor 2 had the lowest DI because the reflection from the crack tip was not as large as for the sensors farther from the crack, but it was increasing as expected. Therefore, sensor 2 was the most sensitive receiver, which was expected because it was right next to the transmitter, sensor 1. Also, the first crack arrival signal was most prominent in sensor 2's waveform. Sensor 2 was also more sensitive to larger cracks because it was located right above them. However, the 1 mm crack may have been too small. Along with sensor 3, it was located right above the 10 mm crack, unlike sensors 4-8 as shown in Figure 27. Sensor 3 was the next sensitive receiver, and the DIs for the sensors after that were very low or almost zero. Sensor 3 was located at about 10 mm from the notch tip, so it was still able to receive any signal reflecting from the crack. However, sensor 4 was located at about 15 mm from the notch tip, which explained why its DI was very low. Figure 28 demonstrates an example of the difference in waveforms between sensor 2 and sensor 8, where sensor 2 can clearly separate the crack signal at 30 μs while sensor 8 cannot because the next signal merged with the crack signal. The surface waves did not change, however. Therefore, the sensors further from the notch tip are less reliable and for further DI testing, only sensors 2 and 3 will be used.
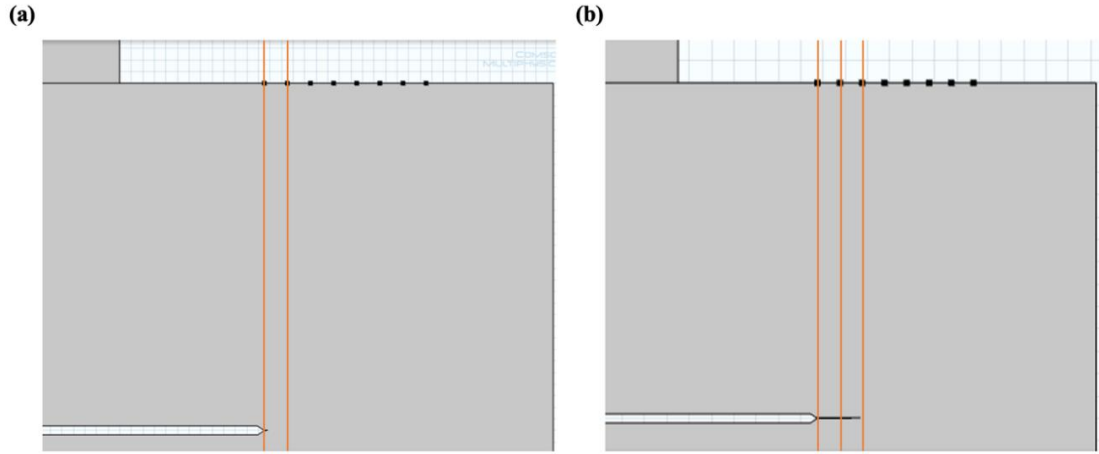
Figure 27. Location of sensors relative to crack length for the extremes (a) 1 mm crack and (b) 10 mm crack.
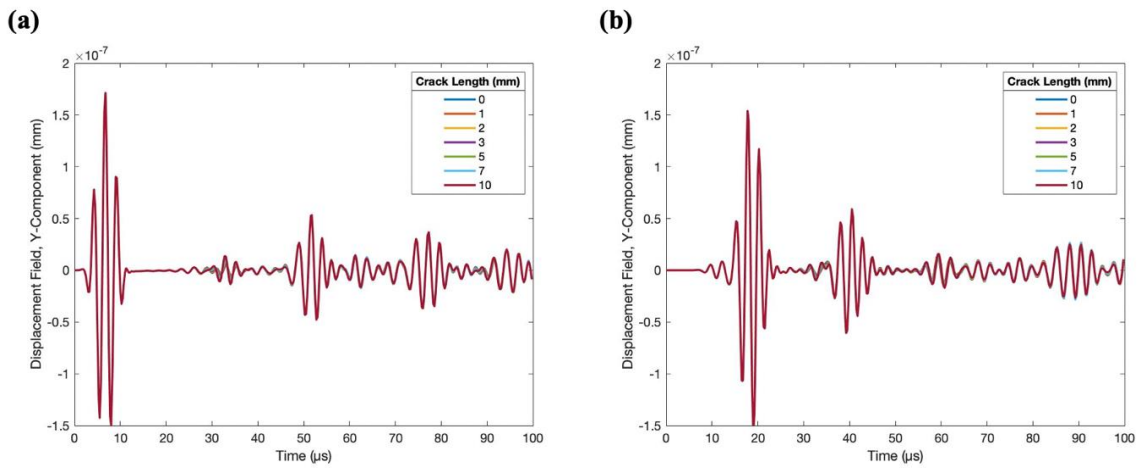

Figure 28. Waveforms for (a) sensor 2 and (b) sensor 8 at 400 kHz.

Figure 29 and Figure 30 show the frequency and phase shift-based DIs. The

normalization of the data was also included to better compare the results for sensors 2 and 3, and

because the actual DI was very small in many cases.
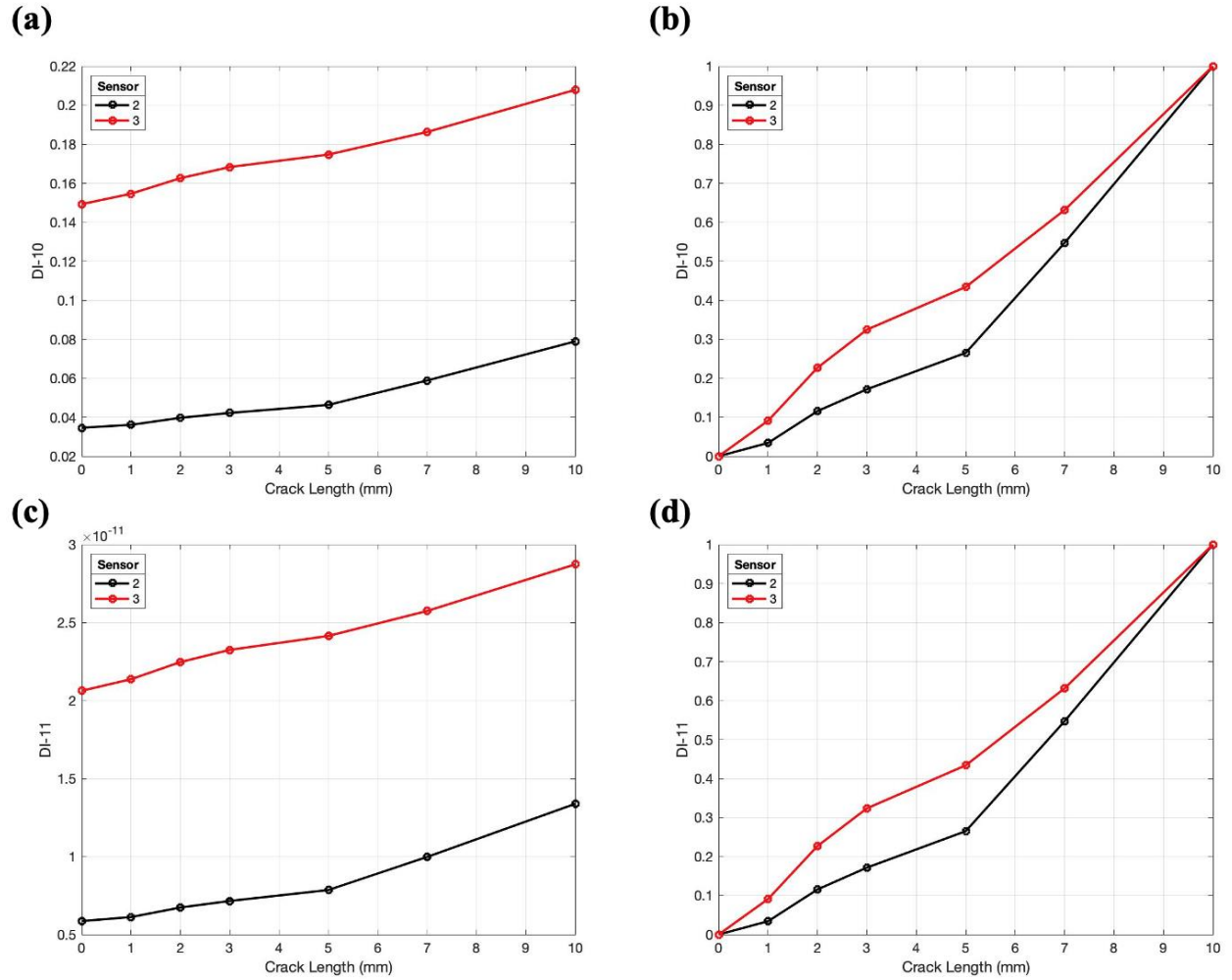

Figure 29. Damage index for sensors 2 and 3 at 400 kHz based on the different equations (a) DI_{10} based on frequency amplitude, (b) DI_{10} normalized, (c) DI_{11} based on frequency amplitude and (d) DI_{11} normalized.
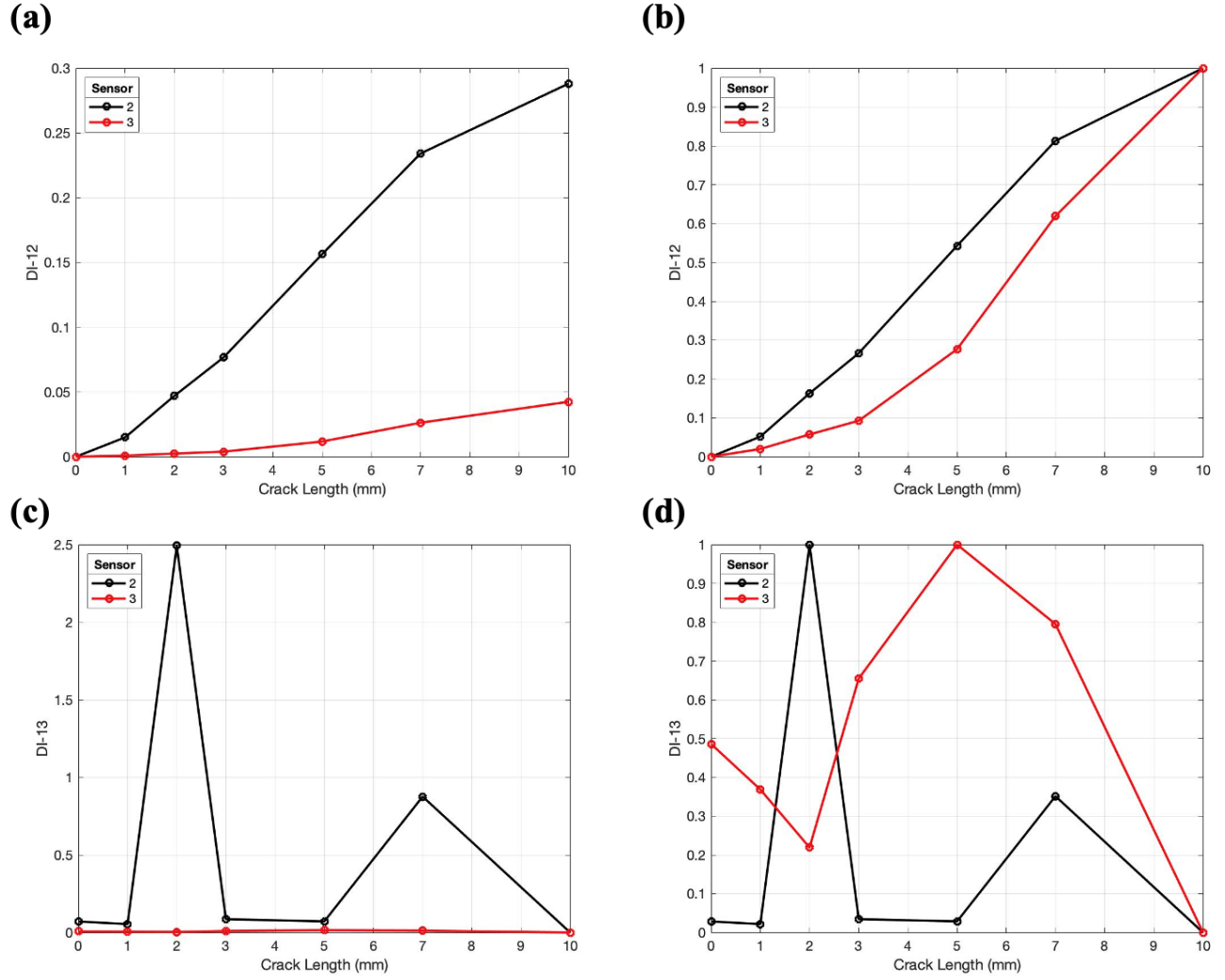
(a)

(b)

(c)

(d)

Figure 30. Damage index for sensors 2 and 3 at 400 kHz based on the different equations (a) DI_{12} based on phase shift (signal difference coefficient), (b) DI_{12} normalized, (c) DI_{13} based on phase shift (relative time delay) and (d) DI_{13} normalized.

Figure 29 and Figure 30 show DI_{10}, DI_{11} and DI_{12} increasing as the crack length increased. However, DI_{13} did not show a similar trend. In fact, DI_{13} (non-normalized) was almost constantly zero for sensor 3 while for sensor 2 it increased to its maximum peak, decreased, and increased to the second smaller peak before returning to zero. When normalized,

DI_{10}, DI_{11} and DI_{12} demonstrated effectively the same increasing trend. For DI_{10} and DI_{11},

sensor 3 had a larger DI than sensor 2 since the amplitude in the frequency domain for the crack

arrival time window was larger as shown in Figure 31, where "Window 1" was the surface wave

arrival window and "Window 2" was the time window for the first crack arrival. These

frequency spectra were created by using the Fast Fourier transform (FFT) in MATLAB for the y-

displacement waveforms to show the signal's energy distribution over a frequency range [46].

By completing a transformation from time domain to frequency domain, the main frequency

components in the time domain signal were identified. The side bends visible were likely from

reflections at the specimen's boundaries. Therefore, the hypotheses for DI_{10}, DI_{11} and DI_{12} were
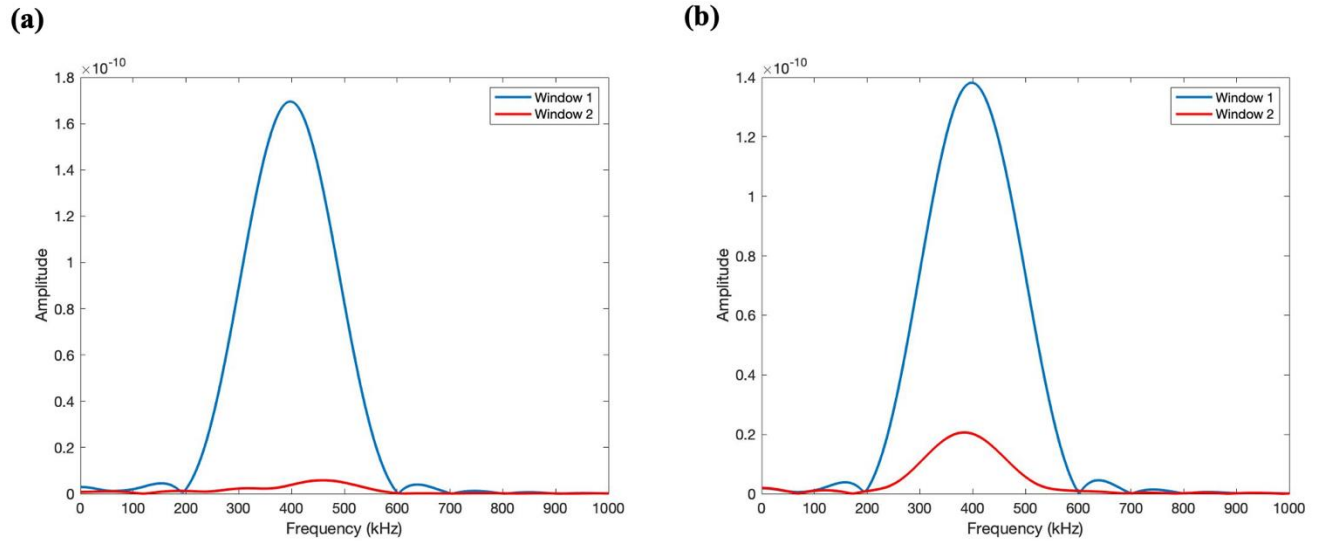
correct.

Figure 31. Frequency spectra of 400 kHz data for (a) sensor 2 and (b) sensor 3.

The frequency spectra were also used to calculate DI_{14}. The frequency at the maximum amplitude was compared for the two windows to obtain the results shown in Figure 32. The DI value for sensor 2 increased as expected while for sensor 3, the DI remained fairly constant. When normalized, the DI value for sensor 3 decreased then increased sharply which suggests that DI_{14} was not as effective for this sensor.
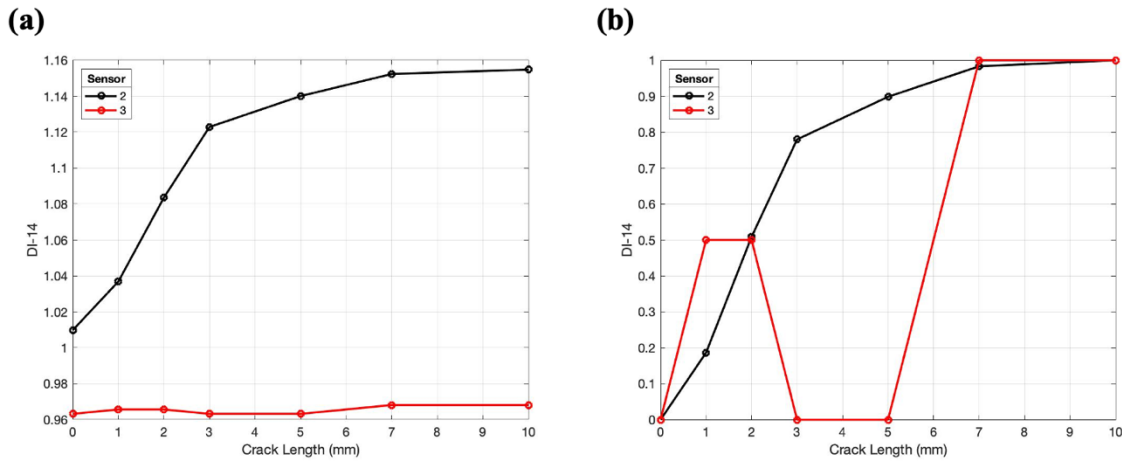

Figure 32. Damage index for sensors 2 and 3 at 400 kHz for (a) DI_{14} based on frequency and (b) DI_{14} normalized.

The damage index vs. sensor number was also plotted to confirm the sensitivity as shown in Figure 33. DI_1, DI_5, DI_8 and DI_9 were chosen because they showed favorable results and had results for all the sensors, which helped visualize the correlation between the sensor position and the DI value. Figure 33a and Figure 33b show the largest DI starting at sensor 2, followed by a sharp decrease and then a smaller peak at sensor 4 and 5, respectively. Sensors 6-8 showed little response and thus the DI was almost zero. From these figures, it can be seen that sensor 2

responded well and was the most sensitive. Figure 33c and Figure 33d display a peak DI at sensor 3, followed by a decrease. After that there was a steep jump at sensor 8. The equations for DI_1 and DI_5 considered the reference baseline signal while DI_8 and DI_9 did not, which may be the reason for these differences. The valued of DI_8 and DI_9 for sensors further from notch tip increased as the crack length increases. No significant change was observed for sensors 7 and 8 which were further from the simulated crack length. The DI equations were also tested for the 300 kHz frequency to determine any correlations between the data.
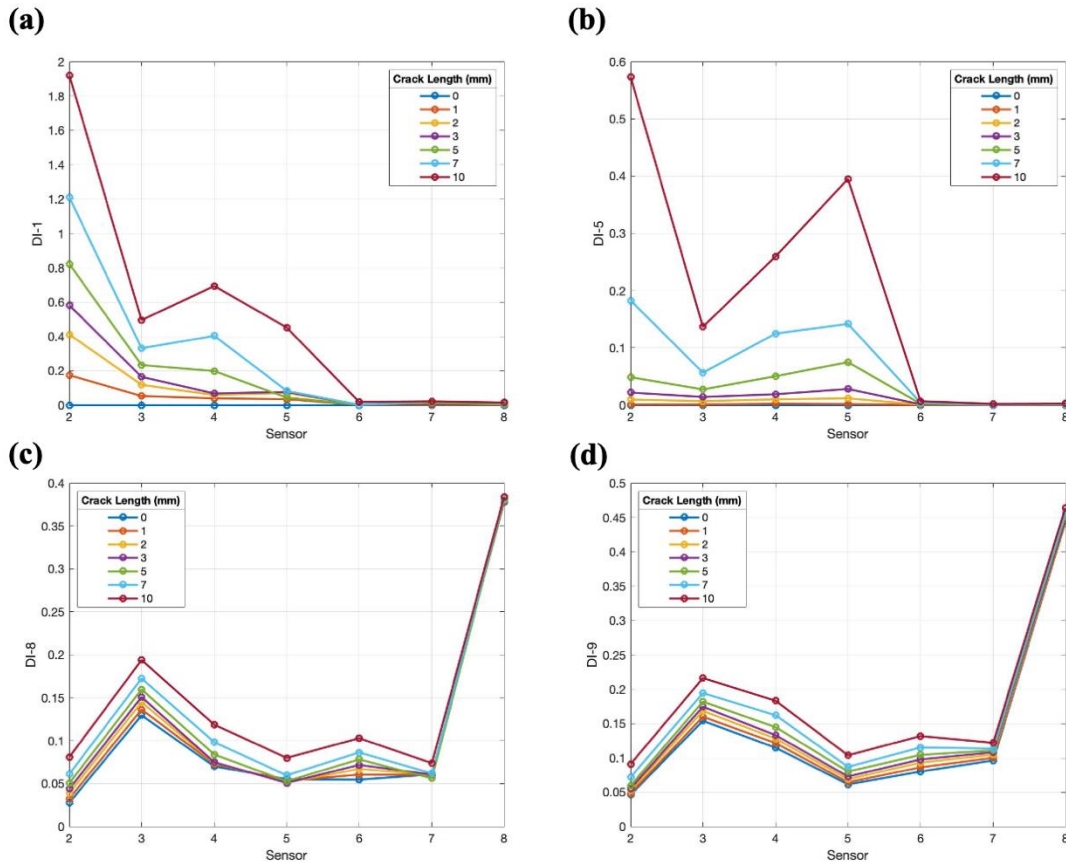

Figure 33. Damage index vs. sensor number for (a) DI_1, (b) DI_5, (c) DI_8 and (d) DI_9 at 400 kHz.

The equations from Table XIV were used to plot DI vs. crack length for a frequency of 300 kHz as shown in Figure 34, Figure 35 and Figure 36. The time window was based on where the surface arrival signal ended and the crack arrival signal began, which was around 30 µs, similar to the 400 kHz results.
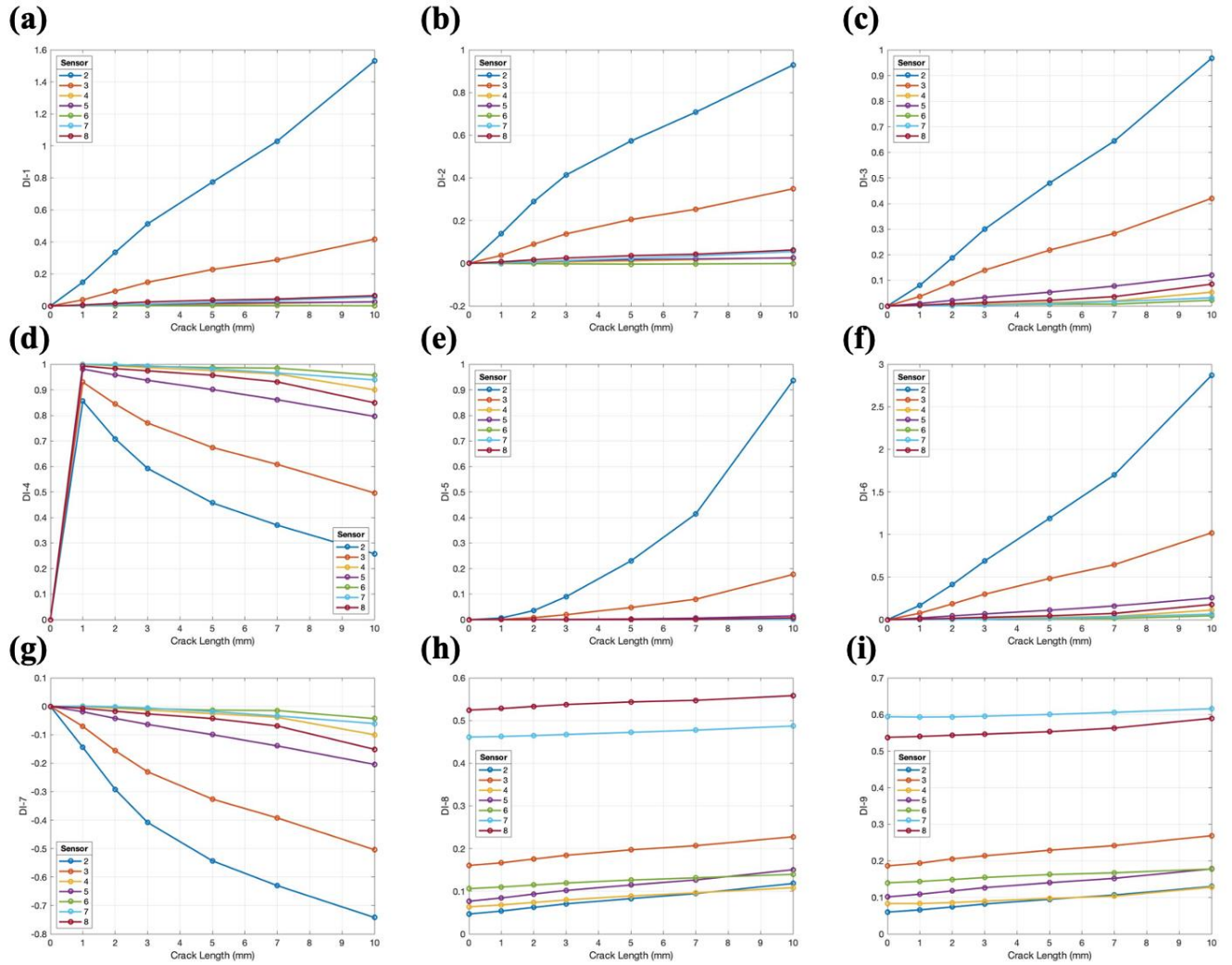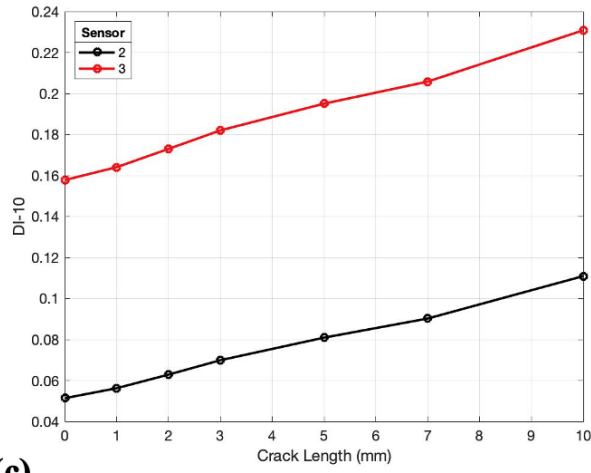

Figure 34. Damage index for sensors 2-8 at 300 kHz based on the different equations (a) DI_1 based on amplitude, (b) DI_2 based on amplitude attenuation, (c) DI_3 based on root mean square deviation, (d) DI_4 based on energy, (e) DI_5 based on energy, (f) DI_6 based on energy, (g) DI_7 based on energy, (h) DI_8 based on amplitude and (i) DI_9 based on energy.

From Figure 34, it can be seen that DI_1, DI_2, DI_3, DI_5, DI_6, DI_8 and DI_9 followed a similar trend to the 400 kHz data, where the DI increased as the crack length increased. DI_4 and DI_7 could not be used for further analysis because they did not show a clear correlation between the data. Between the 400 kHz and 300 kHz data there were slight differences in the DI values. The 300 kHz data showed most of the other sensors (besides sensor 2) having DI values of almost zero, while this was not the case for the 400 kHz data (e.g., sensor 3, 4 and 5). The 300 kHz frequency was less sensitive so anything past sensor 2 had trouble detecting the crack. Sensors 6, 7 and 8 were consistently unreliable to record any damage because they are too far from the crack.

Figure 35 and Figure 36 show the frequency and phase shift-based DIs and the normalization of the data.
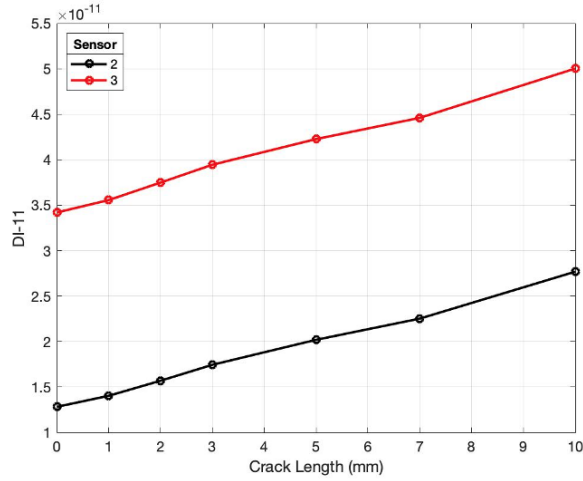
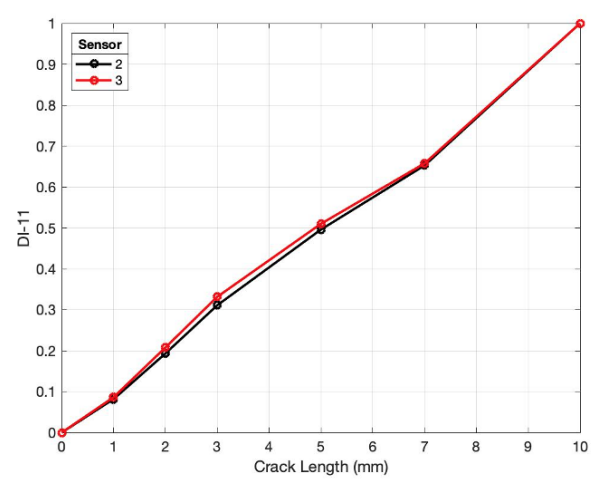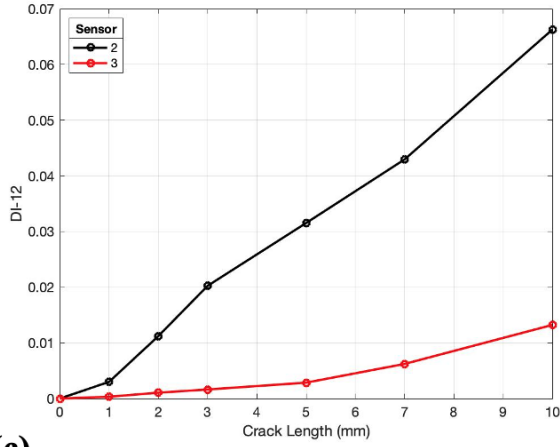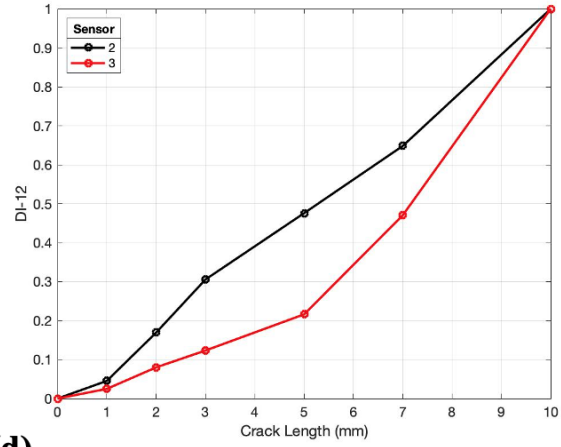**(a)**

(b)
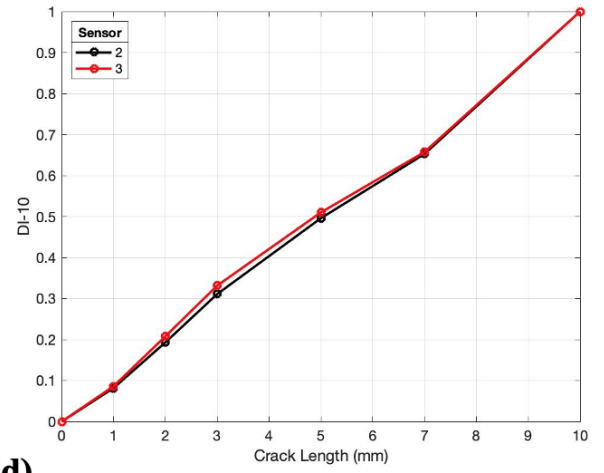
(c)

(d)

Figure 35. Damage index for sensors 2 and 3 at 300 kHz based on the different equations (a) DI_{10} based on frequency amplitude, (b) DI_{10} normalized, (c) DI_{11} based on frequency amplitude and (d) DI_{11} normalized.
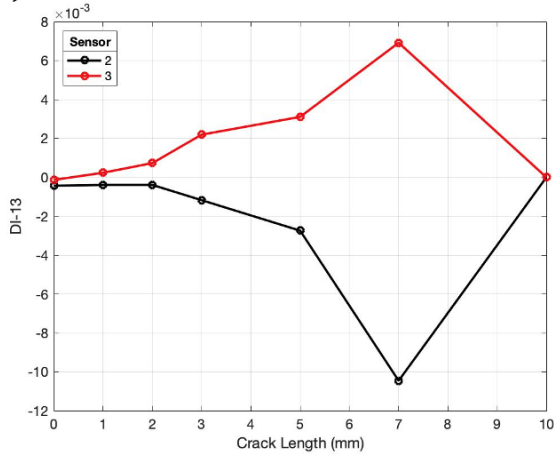
67

(a)

(b)

(c)

(d)
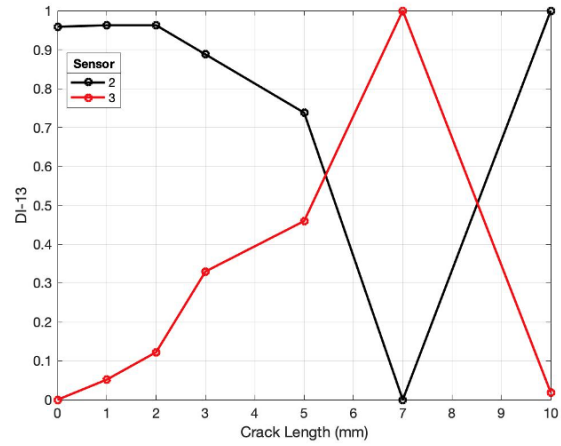
Figure 36. Damage index for sensors 2 and 3 at 300 kHz based on the different equations (a) DI_{12} based on phase shift (signal difference coefficient), (b) DI_{12} normalized, (c) DI_{13} based on phase shift (relative time delay) and (d) DI_{13} normalized.

Figure 35 and Figure 36 show DI_{10}, DI_{11} and DI_{12} increasing as the crack length increases, which was similar to the 400 kHz results. However, DI_{13} did not show a similar trend. In fact, the non-normalized results showed the DI values for sensor 2 and sensor 3 to be completely opposite of each other with respect to the line $x = 0$, with the maximum peak of sensor 2 being slightly larger. When normalized, DI_{10}, DI_{11} and DI_{12} demonstrated the same

increasing trend. However, the results for sensors 2 and 3 were almost the same which confirmed

that the 300 kHz frequency was not sensitive enough to separate the differences between the two

sensors. Even though this was the case, for DI_{10} and DI_{11}, sensor 3 had a slightly larger DI than

sensor 2 since the amplitude in the frequency domain for the crack arrival time window

("Window 2") was larger as shown in Figure 37.
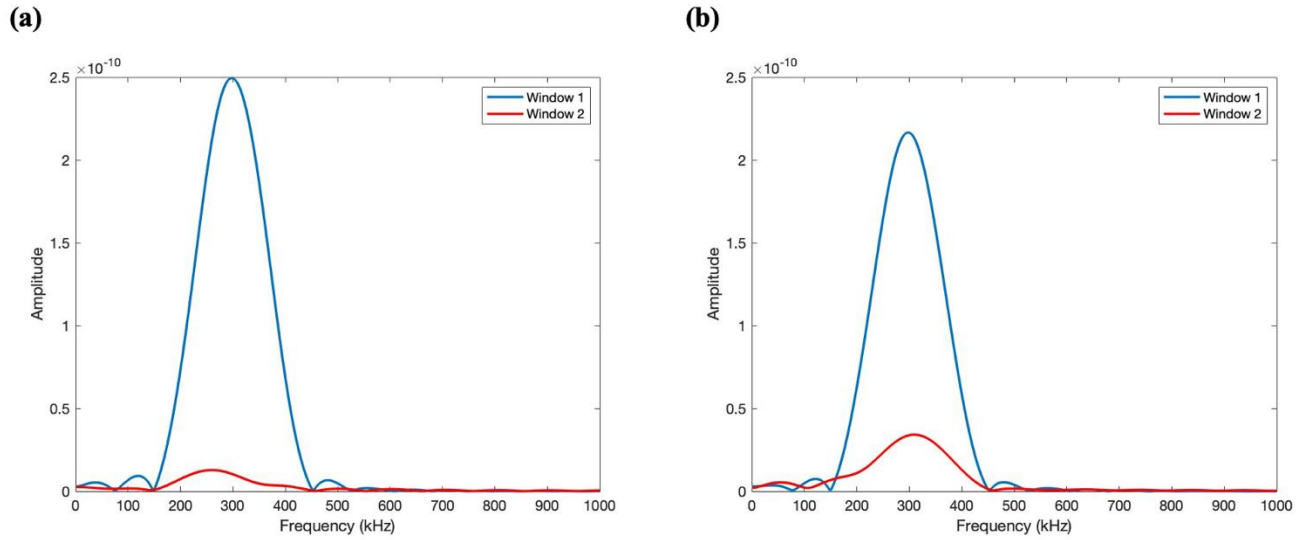
Figure 37. Frequency spectra of 300 kHz data for (a) sensor 2 and (b) sensor 3.

The 300 kHz frequency spectra were used to calculate DI_{14}. The frequency at the

maximum amplitude was compared for the two windows to obtain the results shown in Figure

38. The DI value for sensor 2 increased as expected. The DI for sensor 3 stayed mainly constant

but was higher than sensor 2. When normalized, the DI value for sensor 3 started at one, then

decreased and increased sharply which suggests that DI_{14} was not as effective for this sensor.

(a)

(b)

Figure 38. Damage index for sensors 2 and 3 at 300 kHz for (a) DI_{14} based on frequency and (b) DI_{14} normalized.
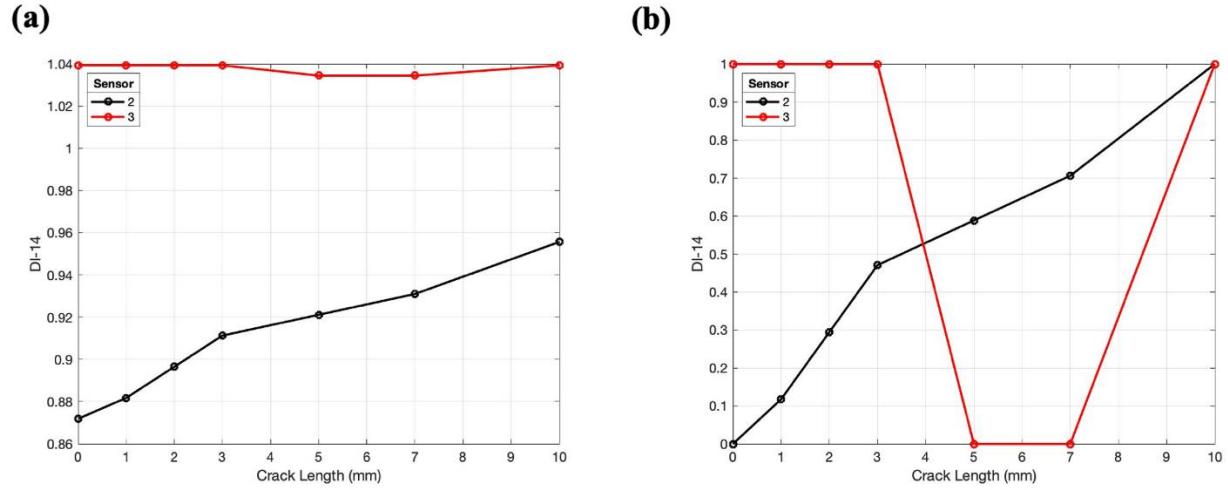
Similar to the 400 kHz results, the damage index vs. sensor number was also plotted as shown in Figure 39. Figure 39a and Figure 39b showed the largest DI starting at sensor 2, followed by a sharp decrease. The rest of the sensors did not register any significant DI values. As confirmed from the 400 kHz results, sensor 2 responded well and was the most sensitive. Figure 39c and Figure 39d display a peak DI at sensor 3, followed by a decrease and then a sharp increase at sensor 7. The highest DI always corresponded to the largest crack length, which was expected. The DI equations will be tested further using the experimental data.
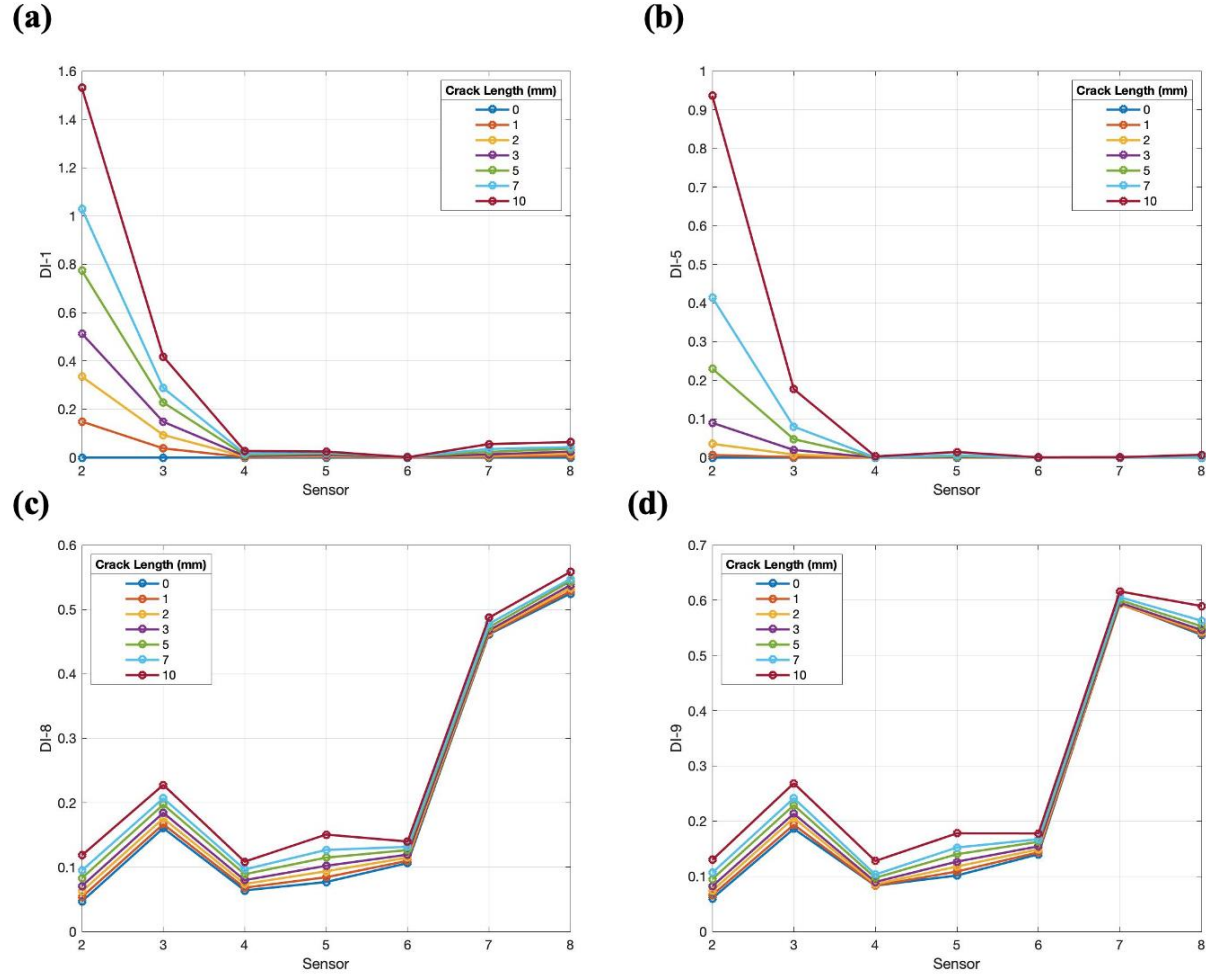
(a)

(b)

(c)

(d)

Figure 39. Damage index vs. sensor number for (a) DI_1, (b) DI_5, (c) DI_8 and (d) DI_9 at 300 kHz.

3.5 Summary

An idealized test specimen was designed so that the fatigue crack reached 10 mm in about 6-8 hours of testing in the laboratory. Once the geometry was determined, a static numerical model was built in COMSOL Multiphysics. It was approximated as a two-dimensional plain strain model with a thickness of 0.5" (12.7 mm). The stresses at the notch tip and top hole were 340 MPa and 210 MPa respectively. Since the notch tip stress was much larger than the endurance limits of steel (207 MPa), this confirmed that the crack would start growing at the

notch tip first. Then, the dynamic models were built to obtain y-displacement data and plot DI

vs. crack length and DI vs. sensor graphs. A total of 14 different DI equations were used based

on amplitude and energy in the time and frequency domains as well as phase shift. The DIs that

produced the best results were DI_1, DI_5, DI_8, DI_9, DI_{10}, DI_{12} and DI_{14}. Therefore, both crack-

free and surface wave referencing DIs were effective in detecting damage. They demonstrated

that a frequency of 400 kHz was more sensitive than 300 kHz. Also, sensor 2 was most sensitive

to damage detection because it was closest to the transmitter and the crack.

4. EXPERIMENTAL STUDIES

4.1 Introduction

In this chapter, experimental studies were performed using the modified steel compact tension geometry instrumented with *in-situ* phased-array ultrasonic sensors and an optical microscope. The aims of the experiments were to compare the damage results with the numerical model, demonstrate damage detection and measure the experimental crack length in MATLAB from photos taken through the optical microscope lens. The signal sent though the transmitter provided information about the time-dependent wave signals, which were used to correlate the fatigue crack severity to the ultrasonic signals. Damage indices were calculated based on the time-domain, frequency-domain and phase shift parameters which gave information about damage depending on the crack length.

4.2 Description of Experiment

The experimental setup consisted of the modified steel CT geometry detailed in Figure 40. It was mounted with eight piezoelectric disks at the top as shown in Figure 41.
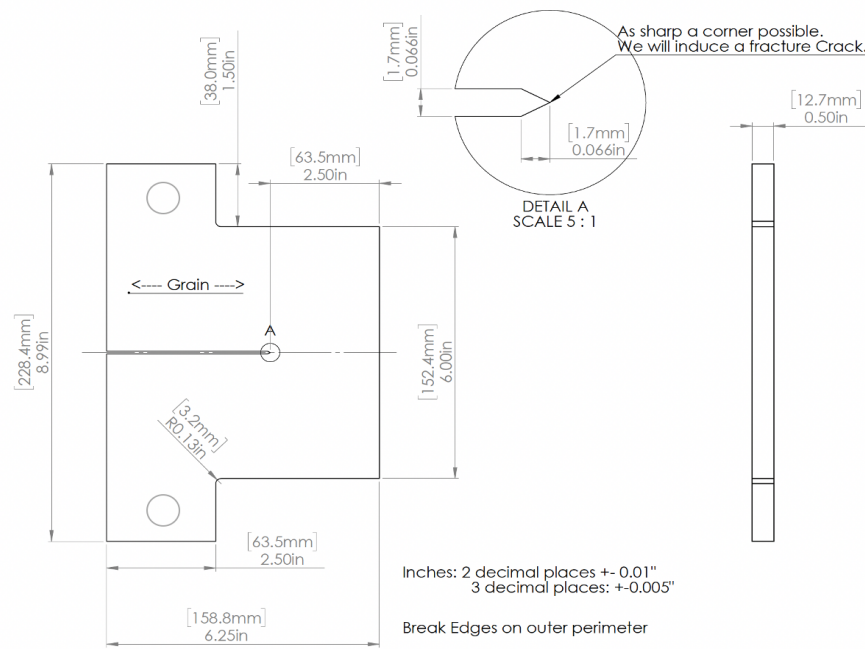
Figure 40. Finalized CT specimen geometry used to build the actual specimen.

Figure 41. Actual modified steel compact tension geometry.

The disks had a diameter of 5 mm and thickness of 0.4 mm and were manufactured by

Steminc. Channel 1 or sensor 1, which was located closest to the notch tip, was used as an AE

sensor during the fatigue loading and as a transmitter during the UT measurement, as shown in

Figure 42. The exact positions of the sensors relative to the left side of the entire specimen are

shown in Table IX in Section 3.2 since the same configuration was used for the numerical and

experimental geometries. The entire specimen was equipped with one to three AE sensors, but

these measurements were not reported nor analyzed in this thesis. An optical camera monitored

crack growth activity at the notch tip. The predicted stress intensity rate ΔK was about

$30.22\ MPa - m^{1/2}$ and the expected crack growth at the end of 100,000 cycles was about 10

mm as presented in Section 3.2. However, the experiment was stopped at 80,000 cycles which

theoretically corresponded to an 8 mm crack length. This was close to the experimental value of

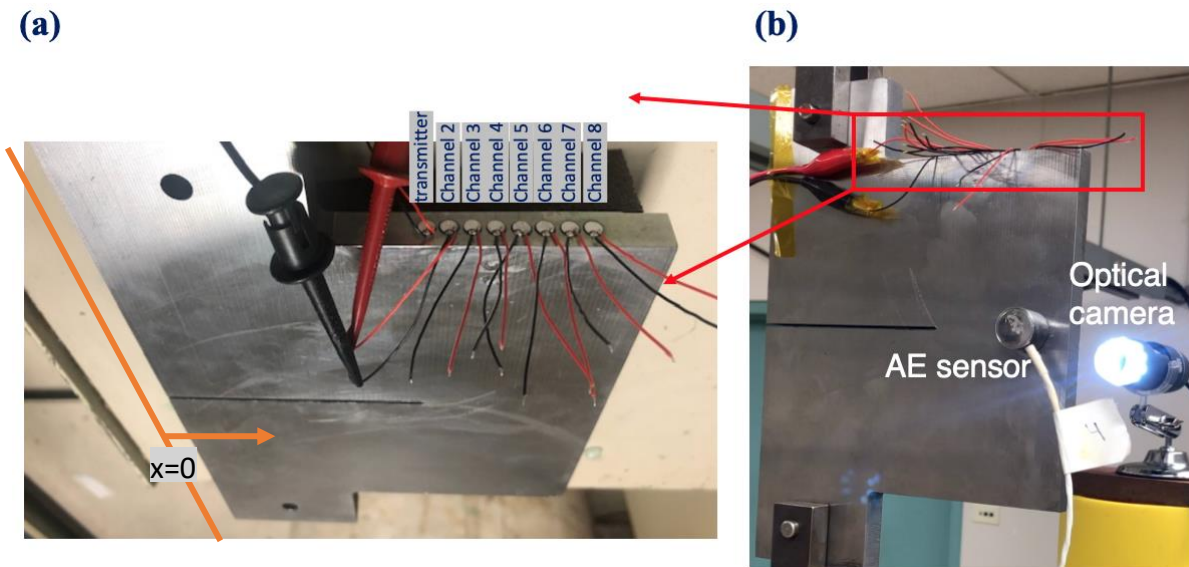8.53 mm at the end of 80,000 cycles.

(a)   **(b)**

Figure 42. Experimental setup showing (a) piezoelectric disks positions on top of the modified
CT sample and (b) positions of AE sensor and optical camera.

The loading machine used during the fatigue loading was the Instron 8500 servo-hydraulic fatigue testing machine. The fatigue specifications were minimum loading of 1.8 kN and maximum loading of 13 kN. The excitation signal was a 4 cycle sine wave shape generated by WaveGen. It was set to 400 kHz and later 300 kHz, with a 10 V constant amplitude. The data was collected at intervals, where after each 10,000 cycle interval, fatigue loading stopped. Then, the load was held at 8 kN to capture the image of the notch tip and crack with the optical camera. This was used to measure the crack length in MATLAB using the Image Processing Toolbox. Finally, the load was reduced to 0.5 kN for the measurement of ultrasonic data by the Mistras data acquisition (DAQ) system, since a small load would not significantly affect the data. The UT data was recorded from receiver sensors 2 to 8, while sensor 1 was the transmitter. The receiver specifications included a 100-400 kHz filter, 3 MHz sampling rate and 3k length. The DAQ involved a transmitter trigger connected to sensor 1 and a receiver connected individually to sensor 2. This loading process was repeated about 8 times, for a total of 80,000 cycles until the crack reached 8.53 mm. A schematic of the loading pattern is shown in Figure 43. A block diagram for the ultrasonic measurements is shown in Figure 44.
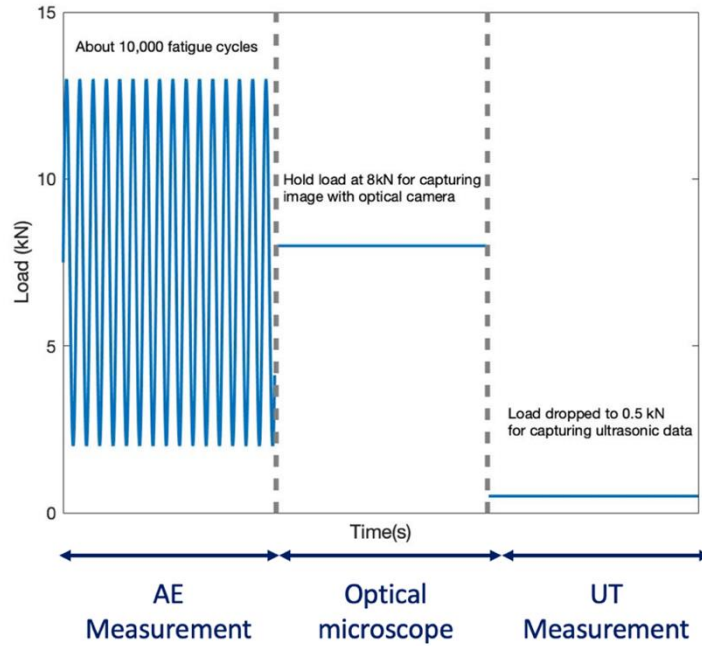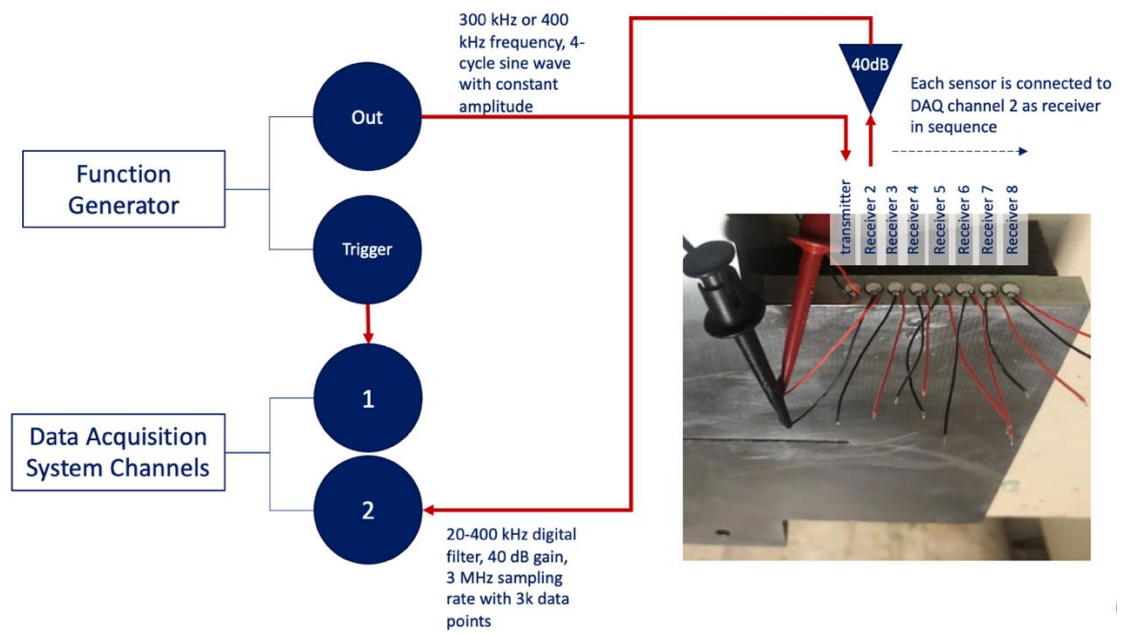
Figure 43. Loading patten for experimental studies.

Figure 44. Block diagram of UT measurements.

4.3 Optical Microscope Analysis

The optical microscope zoomed in to the notch tip, where the fatigue crack was growing. The camera specifications included a magnification of 1000x, 1080p resolution and 2 megapixels with 8 LED lights for better viewing of the subject. The camera was used to capture images at a constant 8 kN load, right after each 10,000 fatigue cycle interval as shown in Figure 45. It was clearly seen that the fatigue crack was progressing steadily. Once the fatigue crack quickly passed stage 1 (initiation stage), the remaining experiment was in stage 2 (propagation stage). These images were used to measure the length of the fatigue crack in MATLAB.
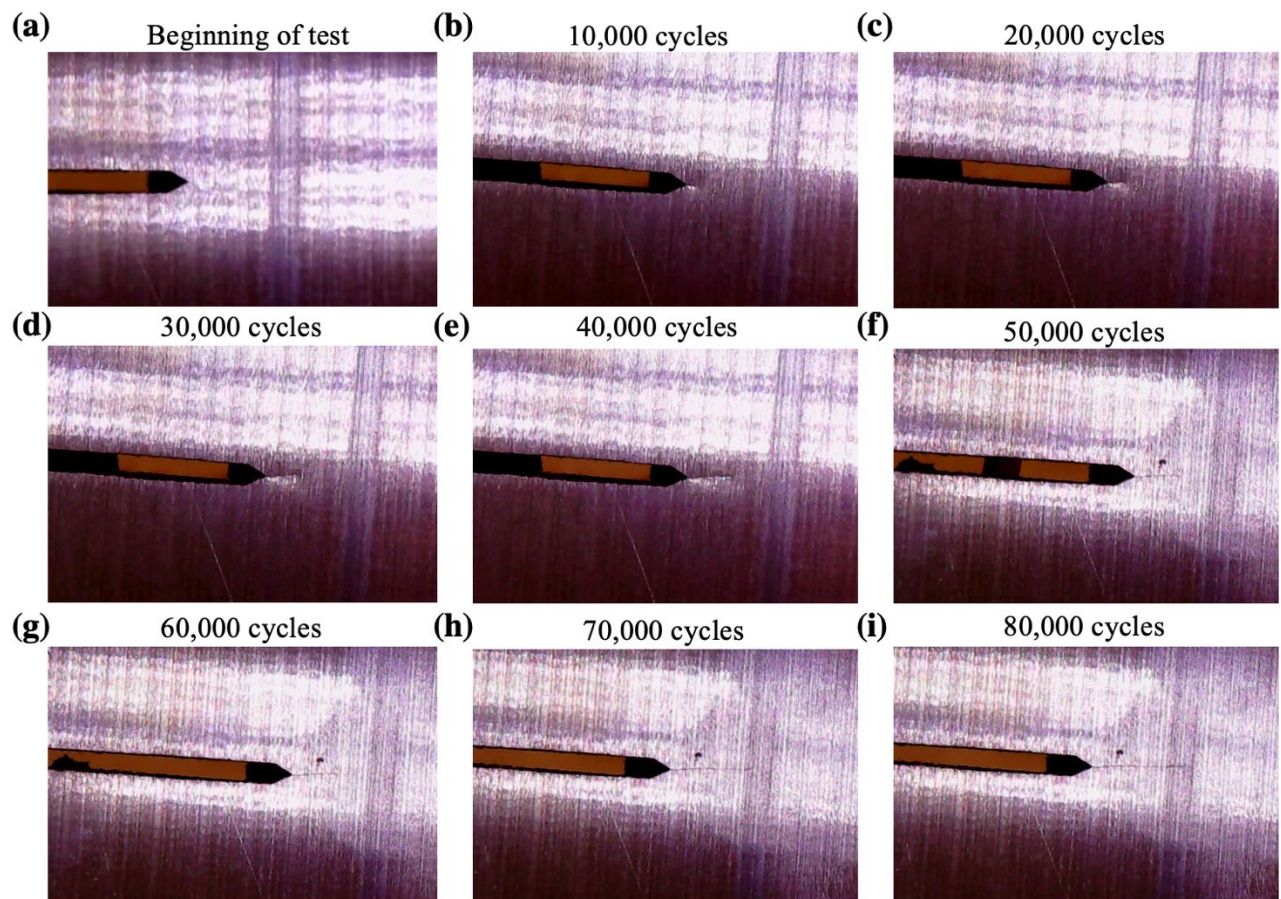

Figure 45. Fatigue crack propagation after each 10,000 cycle interval.

Since MATLAB's measuring tool in the Image Viewer App used pixels as the dimensions, a conversion was done between these units and the actual units (mm). In order to do this, two measurements were taken: one was the angled part of the notch tip and one was the crack length. The angled part of the notch tip's length was known, so a conversion factor was created using the actual length and the length obtained by MATLAB. This conversion factor was applied to the crack, and the length in mm was obtained. An example of MATLAB measurements at 20,000 cycles is shown in Figure 46 and the calculations for 20,000 cycles are shown in Table XV.
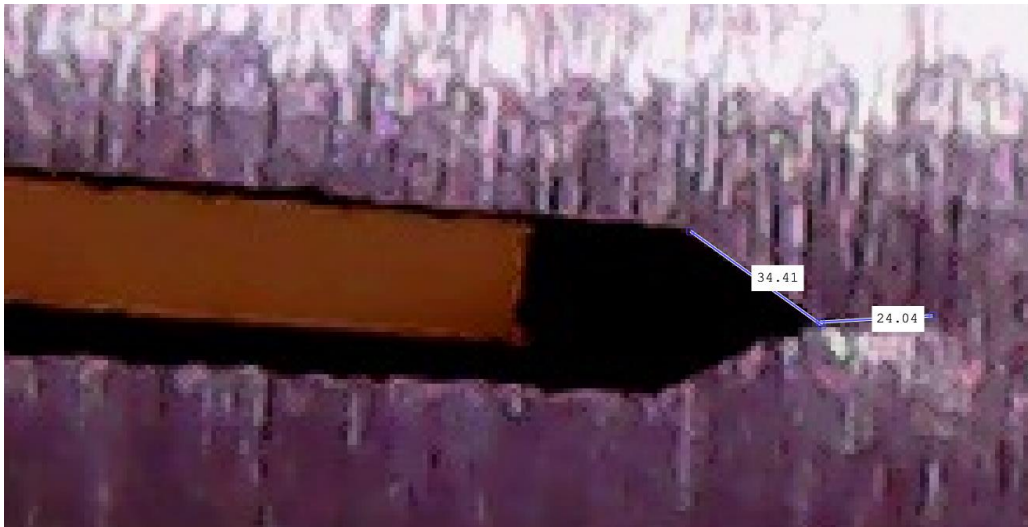

Figure 46. Demonstration of using MATLAB Image Viewer App to measure the crack length at 20,000 cycles.

Table XV: CALCULATIONS TO CONVERT CRACK LENGTH FROM PIXELS TO MM AT 20,000 CYCLES

Component being measured	Actual length (mm)	MATLAB length (pixels)
Angled part of notch tip	1.80	34.41
Crack	1.26	24.04

$$Conversion\ factor = \frac{1.80mm}{34.41\ pixels} = 0.0523\ mm/pixel$$

$$Actual\ crack\ length = 24.04\ pixels * 0.0523\frac{mm}{pixel} = 1.26\ mm$$

Once all the crack lengths corresponding to each cycle interval were known, the ultrasonic results were analyzed, and the corresponding damage analysis was completed. Figure 47 shows the crack length increasing as the cycles increase, which was expected in the experiment and in stage 2 of typical fatigue crack behavior.
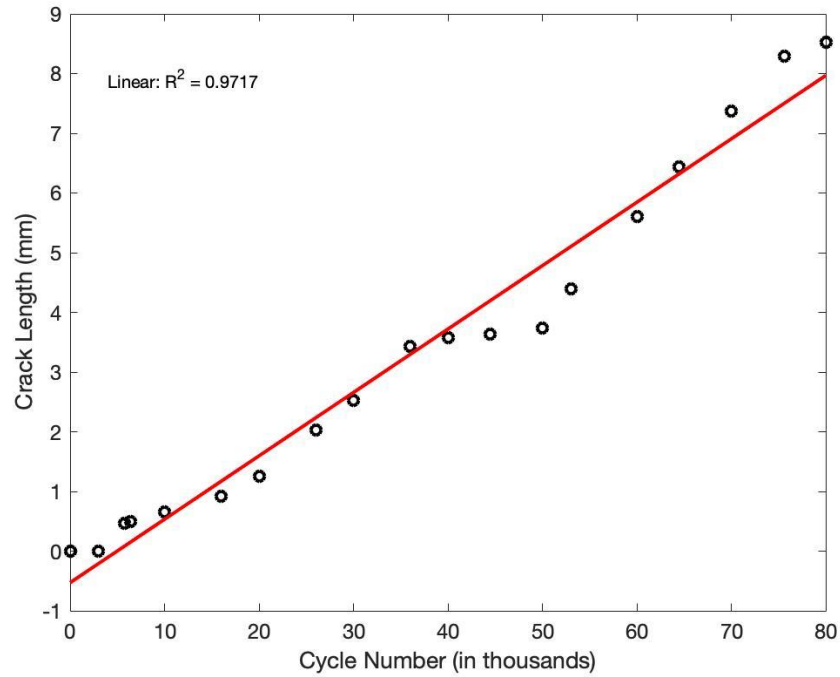
Figure 47. Crack length depending on cycle number.

4.4 Ultrasonic Results using Piezoelectric Wafer Sensors

The ultrasonic data was recorded by sensors 2, 3, 6, 7 and 8, and this was used to calculate damage indices. Sensors 4 and 5 were damaged after 40,000 cycles when the sample was taken from the load machine; therefore, they were not used for measurements. The DIs were calculated for all the sensors based on the classic time-domain equations from Table XIV, as well as the frequency domain and phase shift parameters. For the time-domain, figures were created for all available sensors to compare to numerical results. For frequency and phase shift-based DIs, figures were created only for sensors 2 and 3 because they were determined to be the most sensitive in Chapter 3. An example of an ultrasonic waveform detected by sensor 2 is shown in Figure 48 for 400 kHz and 300 kHz. Two time ranges were analyzed, 21.7-33 μs

(window 2 similar to numerical analysis) and 43-61 μs (window 3). Window 1 represents the

surface arrival wave, window 2 represents the first crack arrival and window 3 represents the

second reflection from the crack. The same windows were used for sensor 3. Window 3 was

added since the first arrival window could not clearly be separated as in the numerical results.

The waveforms were analyzed and the correlation with the crack length was expressed in the
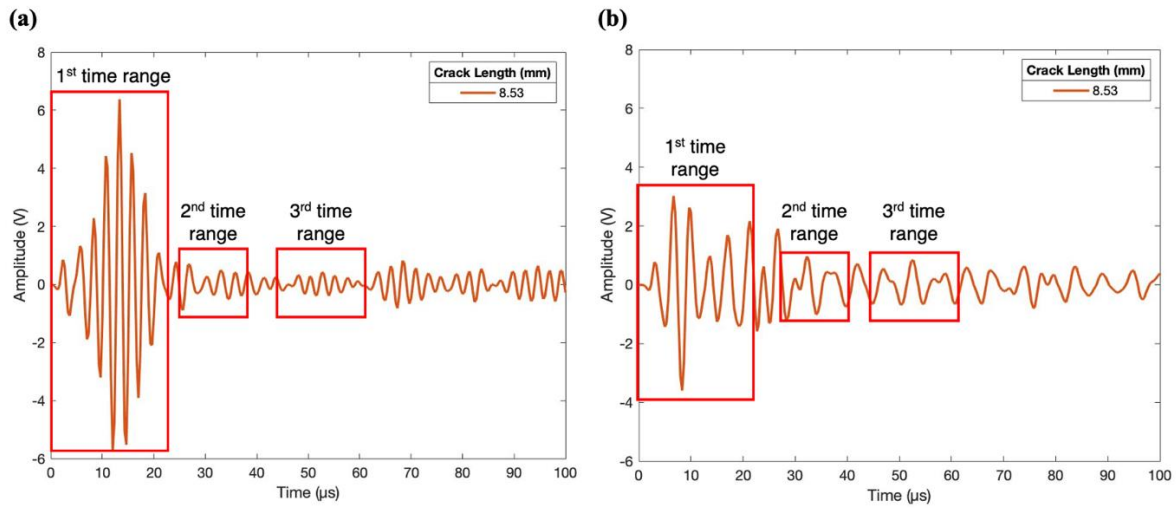
form of the damage index.

Figure 48. Sensor 2 ultrasonic waveform for (a) 400 kHz and (b) 300 kHz.

The FFT transforms of the waveforms were completed as shown in Figure 49 and Figure

50, where window 1 represents the time range for the first surface wave arrival, which is constant

for every data set. Window 2 is the chosen time range for where the crack was expected (21.7-33

μs). Window 3 is the second reflection from the crack (43-61 μs). Even though the time of flight

calculated earlier in Table XIII was about 30 μs, a second time range was included because the

separation of the crack signal at this time was not as apparent as in the numerical results, so both ranges were compared.

As seen in Figure 49, the main frequency was 400 kHz. However, in Figure 50, there was not a clear peak at 300 kHz for either of the time ranges because the wavelength for 300 kHz was longer than 400 kHz and there were not enough cycles within the chosen time range for the FFT to properly display the peak. The time to complete one cycle at 300 kHz is $\frac{1}{0.3*10^6\ Hz} = 3\ \mu s$ while at 400 kHz it was $\frac{1}{0.4*10^6\ Hz} = 2.5\ \mu s$. Therefore, it took less time to complete one cycle at 400 kHz, which proved there are more cycles in the same time period as compared to 300 kHz.
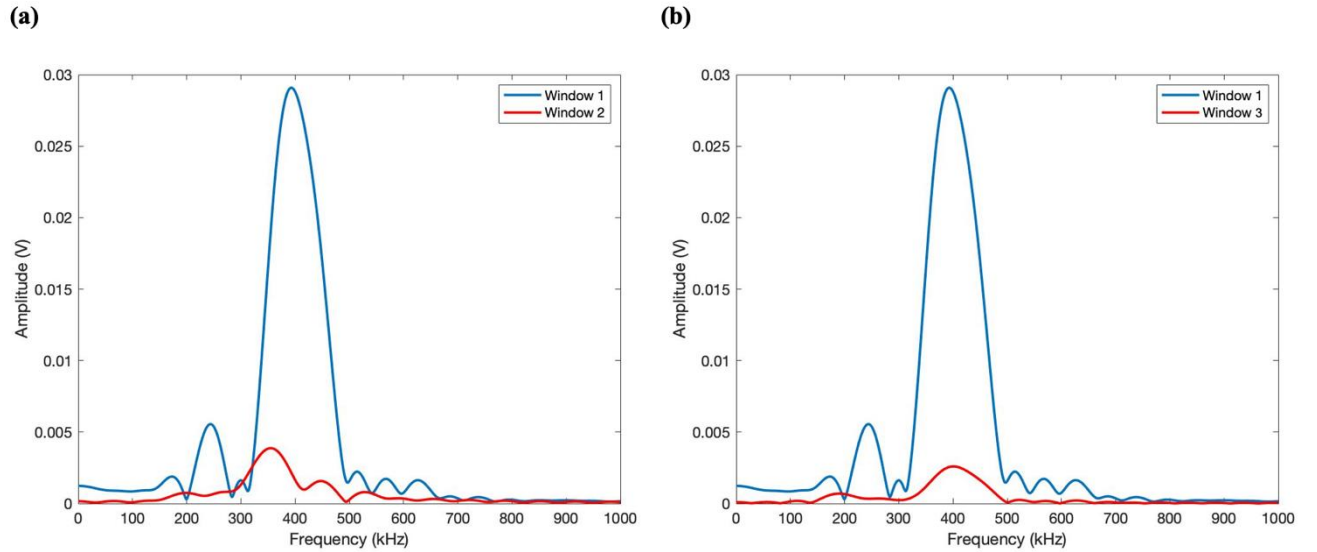
(a)

(b)

Figure 49. Frequency spectra of sensor 2 at 400 kHz ultrasonic waveform in the (a) 21.7-33 μs time range and (b) 43-61 μs time range.
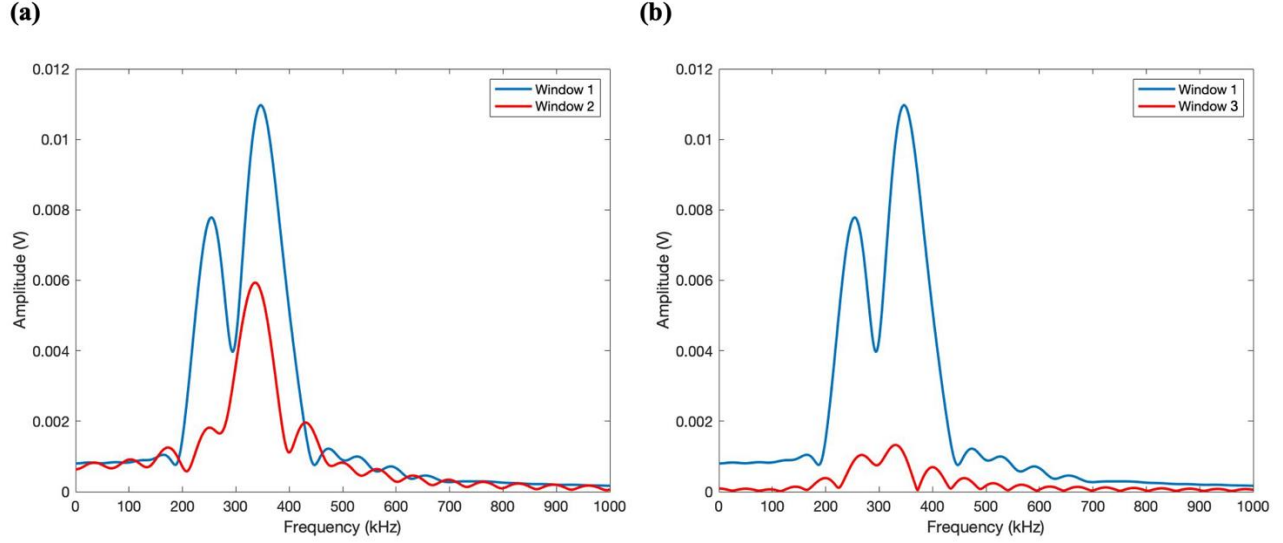
Figure 50. Frequency spectra of sensor 2 at 300 kHz ultrasonic waveform in the (a) 21.7-33 μs time range and (b) 43-61 μs time range.

Using the ultrasonic signal information in the time domain, the damage indices were calculated. Figure 51, Figure 52, Figure 53 and Figure 54 show the results for DI_1, DI_5, DI_8 and DI_9 for 400 kHz, which were determined to be the most effective in Chapter 3. Figure 51 and Figure 52 analyze window 2, while Figure 53 and Figure 54 analyze window 3. Figure 52 and Figure 54 show the results for sensors 2 and 3 only, since it was determined that the most favorable results appear when the transmitter and receiver are next to each other from the numerical results. Since there were not many obvious trends as in the numerical results and to reduce the amount of data fluctuation, Figure 52 and Figure 54 were plotted using only the data points.
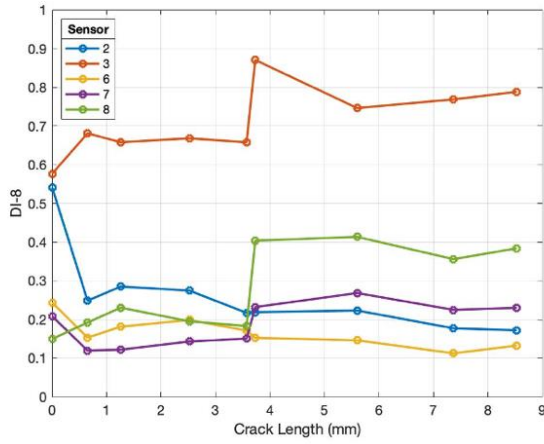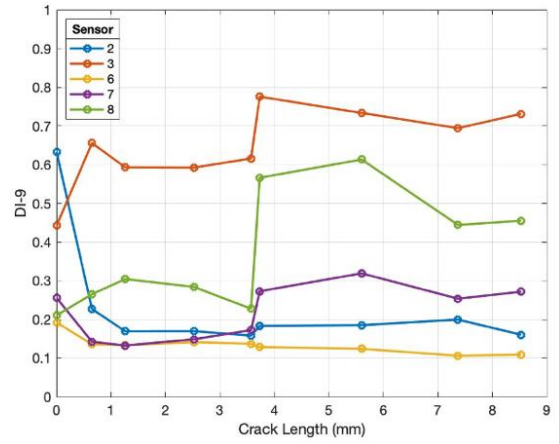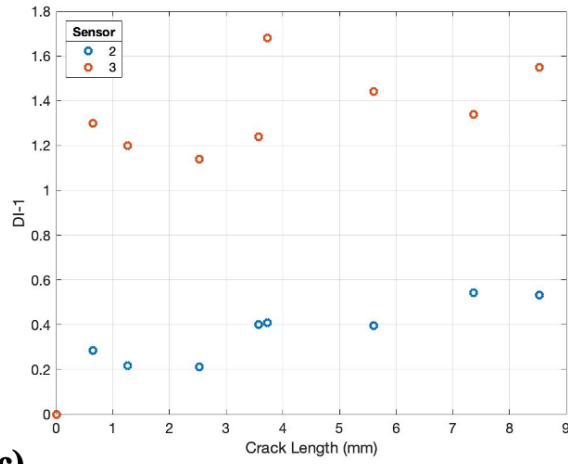
(a)
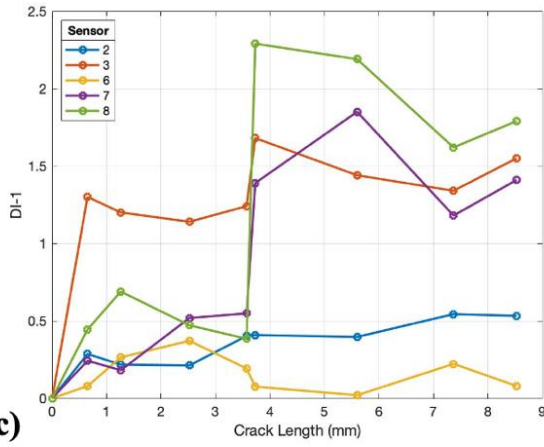
(b)
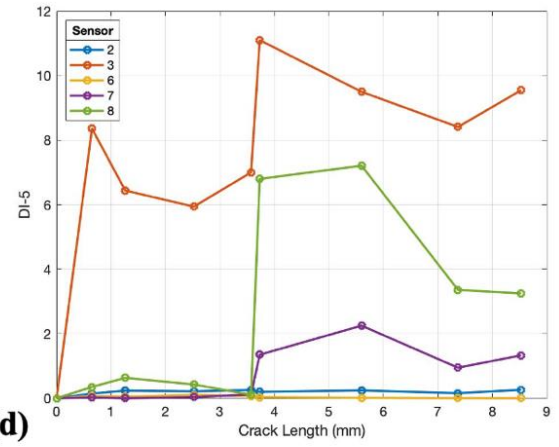
(c)

(d)

Figure 51. Damage index plot for (a) DI_1, (b) DI_5, (c) DI_8 and (d) DI_9 for all experimental sensors at a frequency of 400 kHz and a time range of 21.7-33 µs.

Figure 52. Damage index plot for (a) DI_1, (b) DI_5, (c) DI_8 and (d) DI_9 for sensors 2 and 3 only at a frequency of 400 kHz and a time range of 21.7-33 µs.
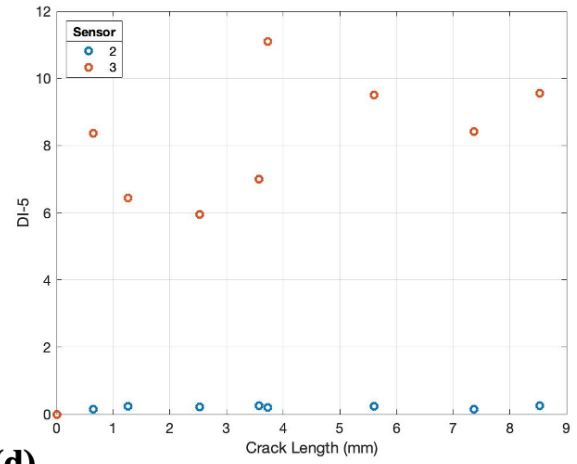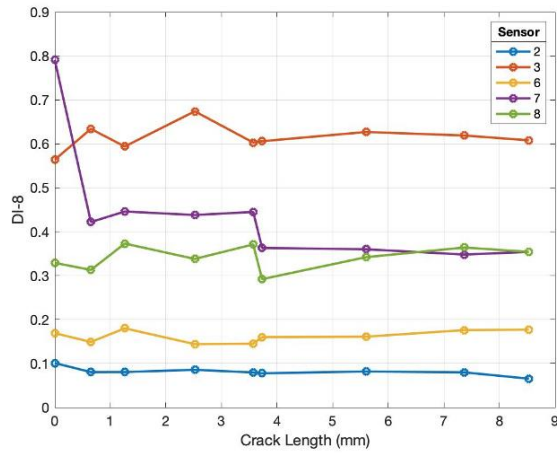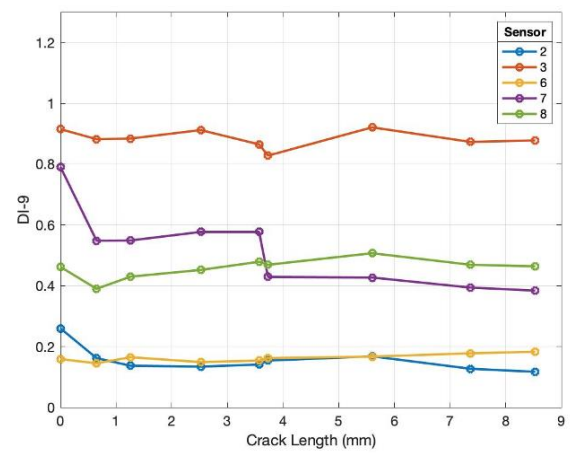
Figure 53. Damage index plot for (a) DI_1, (b) DI_5, (c) DI_8 and (d) DI_9 for all experimental sensors at a frequency of 400 kHz and a time range of 43-61 μs.
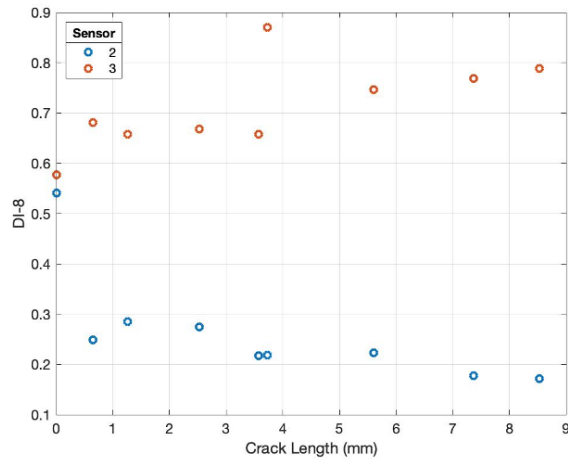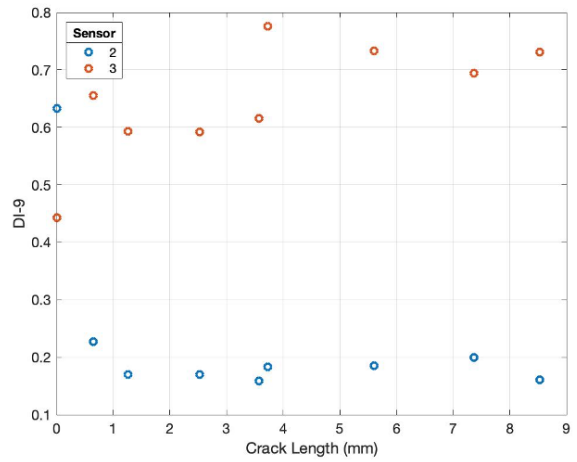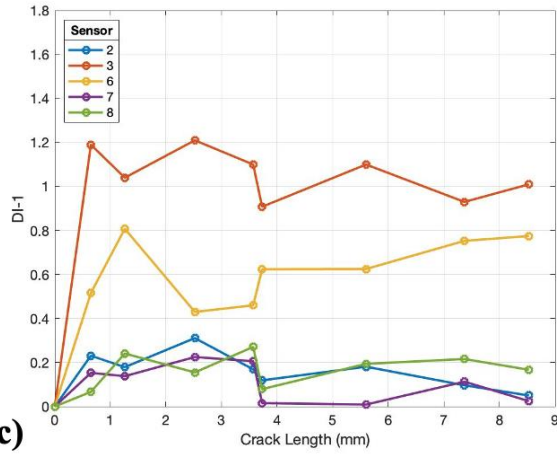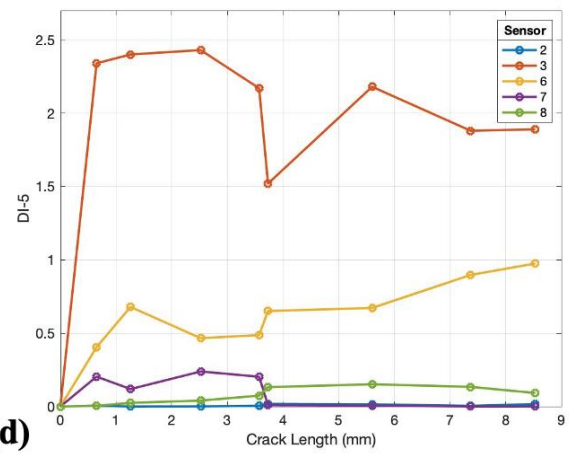
(a)
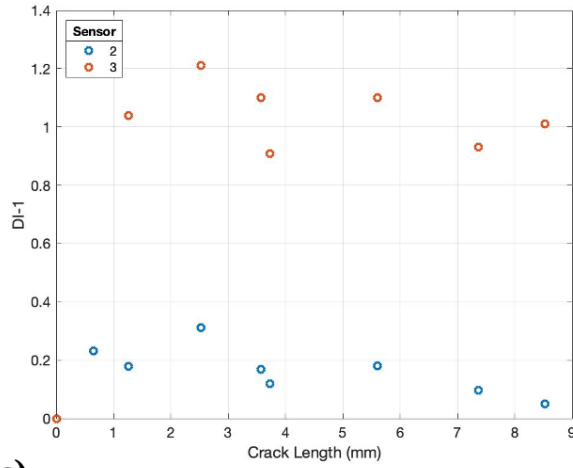
(b)
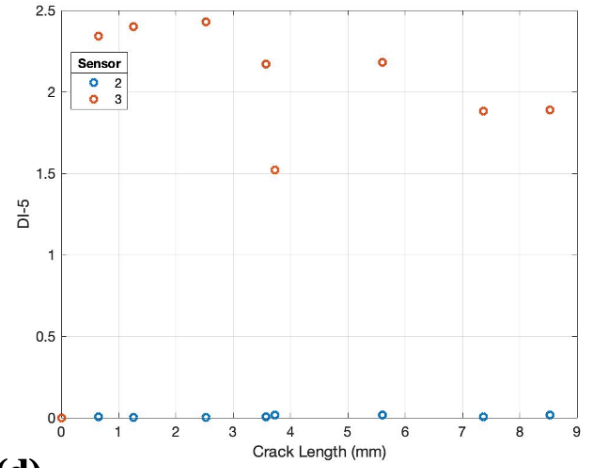
(c)
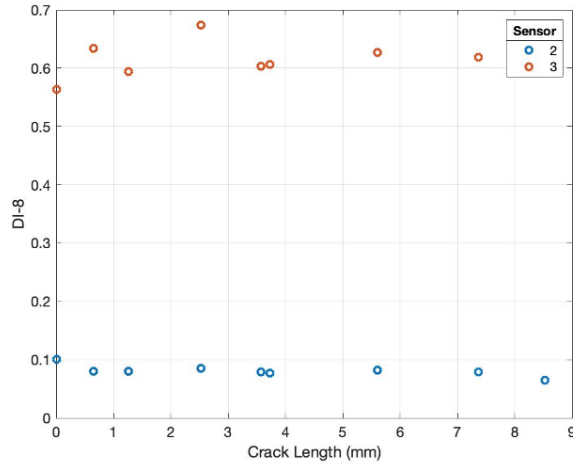
(d)
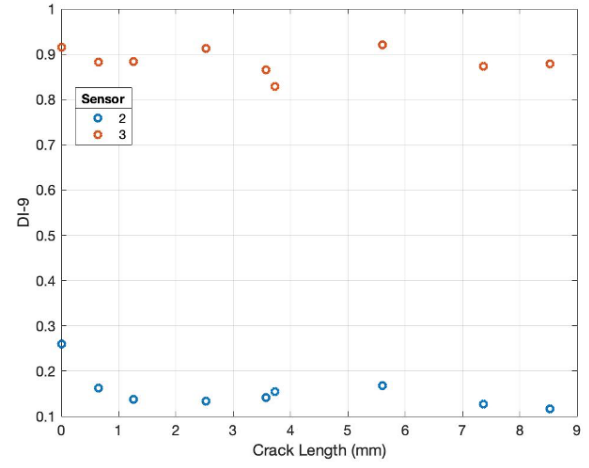
Figure 54. Damage index plot for (a) DI_1, (b) DI_5, (c) DI_8 and (d) DI_9 for sensors 2 and 3 only at a frequency of 400 kHz and a time range of 43-61 µs.

A similar trend was seen in between the crack lengths of 3 and 4 mm where the DI suddenly jumped. This was likely because the specimen was removed which led to sensors 3 and 4 to break around 40,000 cycles. This may have introduced experimental unknowns that affected the data. Overall, DI_8 and DI_9 were most consistent because there were not many drastic changed as seen in DI_1 and DI_5.

Figure 51 (a) and (b) show a sharp increase in the beginning, then the DI generally trends down until the second sharp increase at about 4 mm, before trending down again. The overall values of DI_1 and DI_5 for the 400 kHz frequency were much higher for window 2, perhaps because that is when the first reflection from the crack position was expected. Figure 53a and Figure 53b also show the similar sharp increase in the beginning and remain fairly constant after the jump at 4 mm. Sensor 3 in Figure 52 and sensor 2 in Figure 52a displays a U-shaped trend from the crack length of 0 mm to just before 4 mm. This somewhat follows what was expected with these DIs, which is that the DI would increase as the crack length increases because a bigger signal would return when the crack grows. Figure 52 and Figure 54 both show sensor 3 as having a larger DI than sensor 2, which contradicts the results presented in Chapter 3. However, Figure 52a shows a steadily increasing trend, while Figure 52c, Figure 54a and Figure 54c show a constant or decreasing trend. Figure 52a is based on DI_1 which showed the best results in Chapter 3. Therefore, sensor 2 presented reliable results for the time range of 21.7-33 μs, which was when the crack arrival signal was expected.

In addition, DIs were calculated from the frequency spectra as shown earlier in Figure 49 and Figure 50. The frequency amplitude-based DI equations are shown earlier in Table XIV in Section 3.4.2. In this case, the signal within the time ranges 21.7-33 μs and 43-61 μs was represented by A_{2n}, while the arrival surface wave signal in the 0-20 μs range was represented by A_{1n}. The damage index results and their normalizations for 400 kHz are shown in Figure 55 and Figure 56. Sensors 2 and 3 were tested since they were closest to the transmitter for both frequencies.
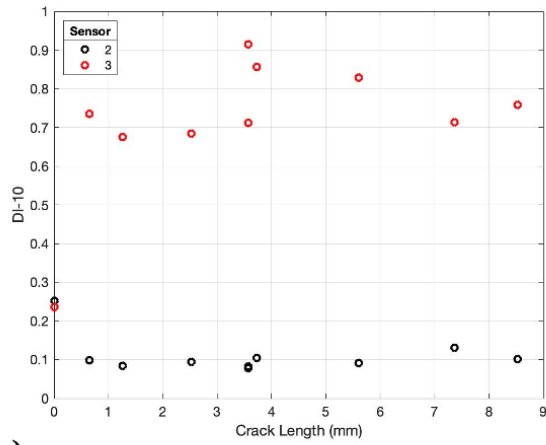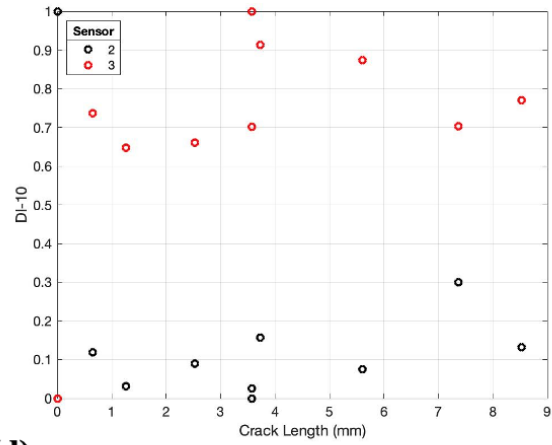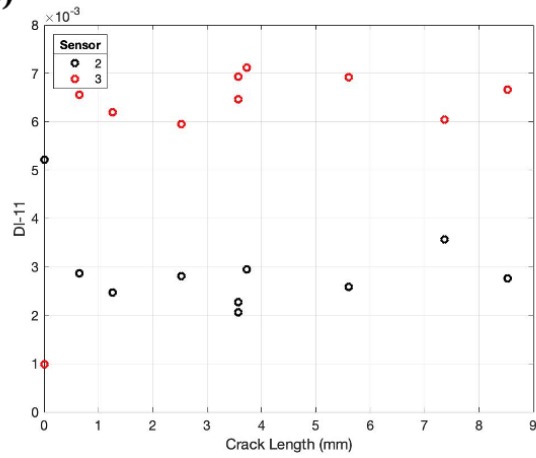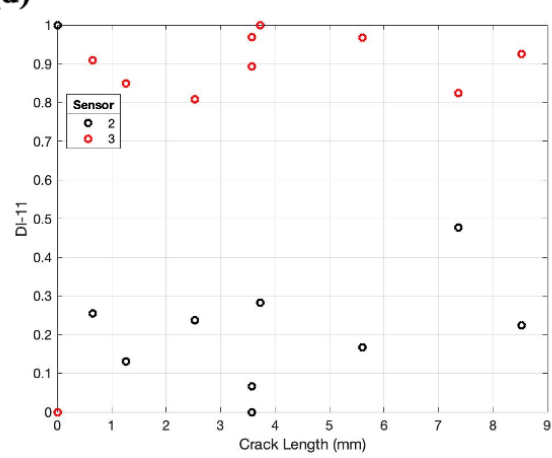
Figure 55. Damage indices based on frequency for (a) DI_{10}, (b) DI_{10} normalized, (c) DI_{11} and (d) DI_{11} normalized. Results are for sensors 2 and 3 at 400 kHz and 21.7-33 μs.

(a)
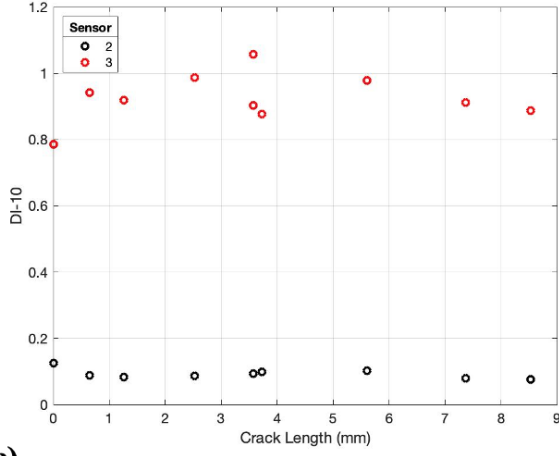
(b)
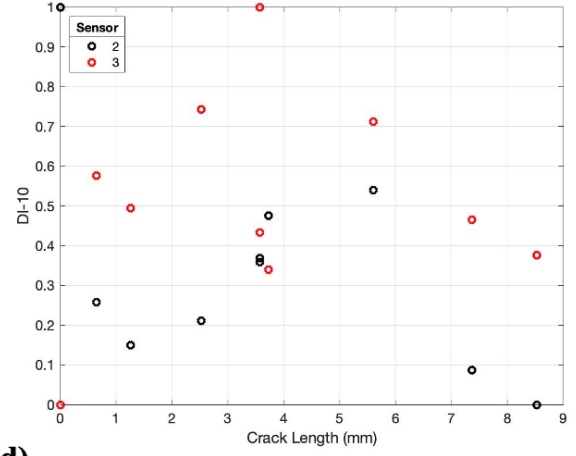
(c)
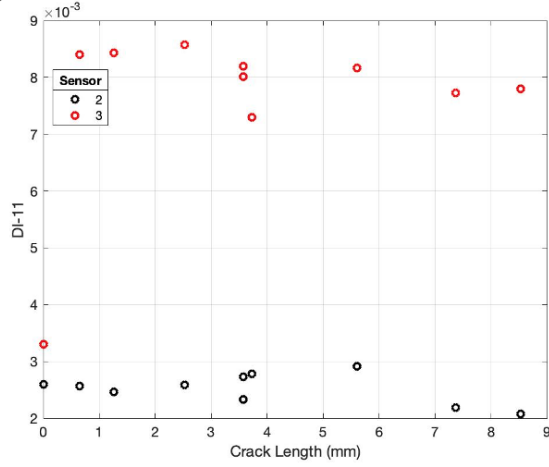
(d)
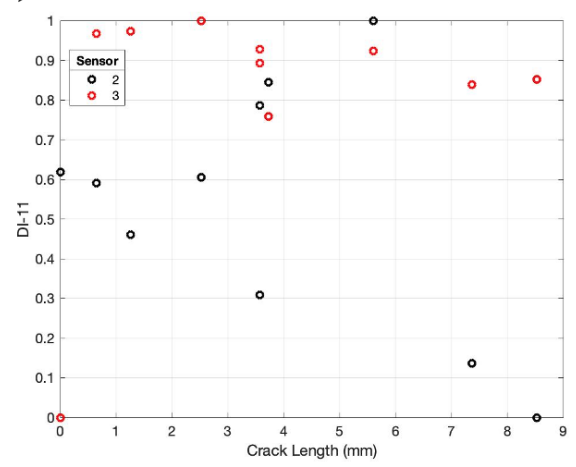
Figure 56. Damage indices based on frequency for (a) DI_{10}, (b) DI_{10} normalized, (c) DI_{11} and (d) DI_{11} normalized. Results are for sensors 2 and 3 at 400 kHz and 43-61 μs.

Sensor 3 in Figure 55 shows a positive increasing trend as the crack length increases up until 4 mm, which agrees with the numerical results and is similar to sensor 3 in Figure 52. This trend is also seen in Figure 56a. This agrees with the original assumption that for DI_{10} the reflection from the crack tip would increase A_{2n} relating to the surface wave arrival parameter, A_{1n}. In addition, DI_{11} was also expected to increase with crack length, because it was the maximum amplitude in the frequency domain which should follow the same increasing trend as

in the time domain. It is more feasible to use the results up to 4 mm because there may have been some experimental unknowns introduced after that point. In the normalized results from Figure 55b, Figure 55d, Figure 56b and Figure 56d, sensor 2 also displays this increasing trend up until 4 mm. This suggests that once the data integrity is improved, the expected results are obtained within the frequency amplitude-based DIs.

The next set of DIs calculated were based on phase shift, with DI_{12} relating to signal difference coefficient and DI_{13} relating to relative time delay. The results are shown in Figure 57 and Figure 58.
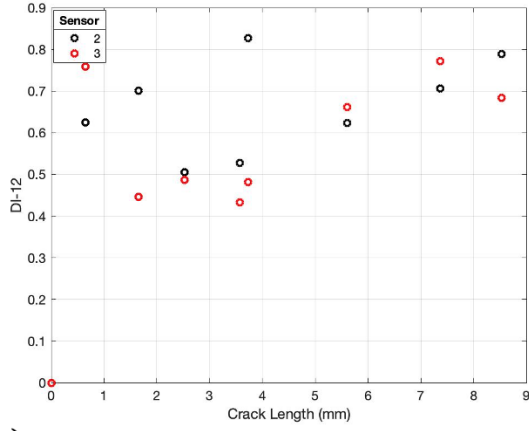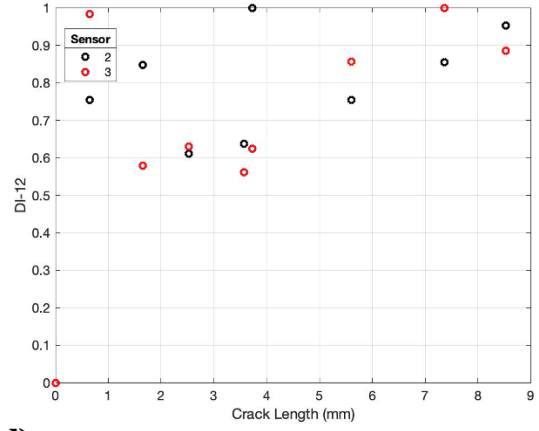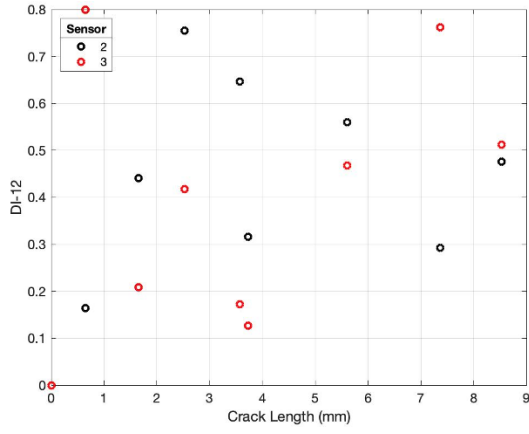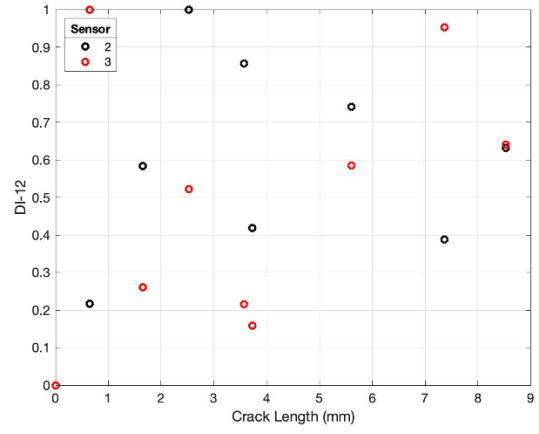
Figure 57. Damage index DI_{12} at 400 kHz for sensors 2 and 3 at (a) 21.7-33 µs, (b) 21.7-33 µs (normalized), (c) 43-61 µs, and (d) 43-61 µs (normalized).

93

(a)
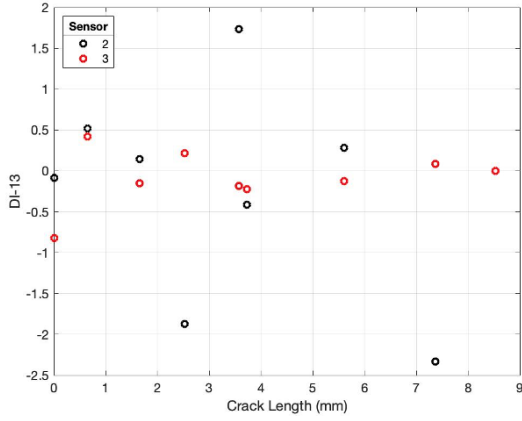
(b)
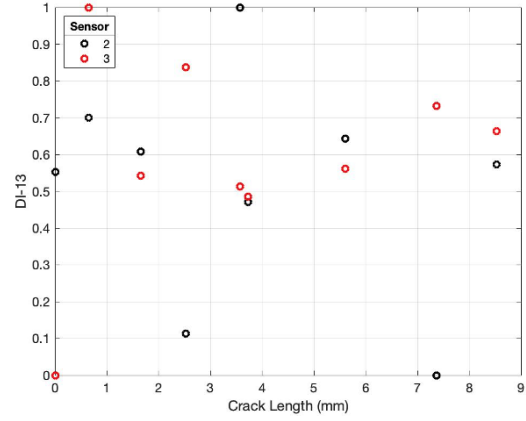
(c)
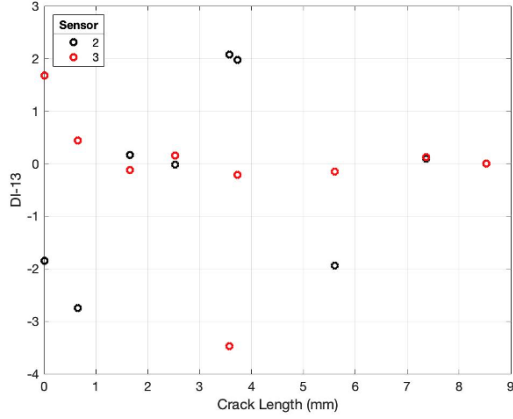
(d)
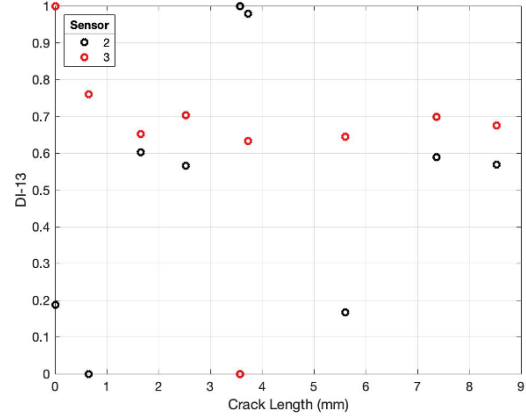
Figure 58. Damage index DI_{13} at 400 kHz for sensors 2 and 3 at (a) 21.7-33 µs, (b) 21.7-33 µs (normalized), (c) 43-61 µs, and (d) 43-61 µs (normalized).

Sensor 3 in Figure 57a showed an overall increasing trend after the initial jump and subsequent decrease. Sensor 2 in Figure 57a also started to increase but decreased suddenly in between the 3 mm and 4 mm crack length, but then increased again after that. Sensor 2 showed the same trend in Figure 57c, but sensor 3 does not present any conclusive results. Figure 58 presents the DI values for sensor 3 as almost constant besides some fluctuations, and sensor 2 does not show conclusive results. Therefore DI_{12} would be more reliable to use than DI_{13}.

The final DI calculated was based on frequency at the maximum amplitude in the frequency spectra. The results are shown in Figure 59.
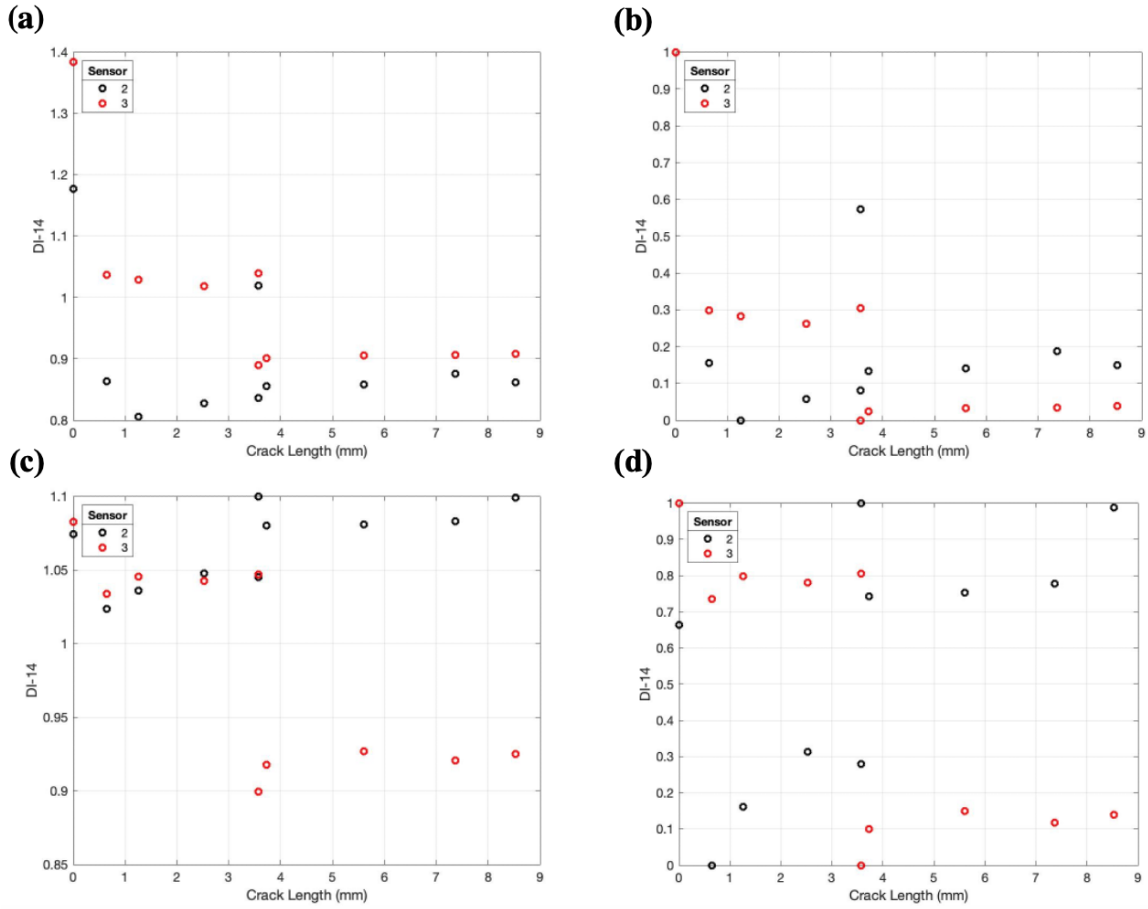
Figure 59. Damage index DI_{14} at 400 kHz for sensors 2 and 3 at (a) 21.7-33 µs, (b) 21.7-33 µs (normalized), (c) 43-61 µs, and (d) 43-61 µs (normalized).

Figure 59a shows a "u" shaped trend for both sensors, with the DI values increasing right before the unloading and reloading that occurred at 40,000 cycles. After this event, the DI values remained constant and decreased slightly towards the end. Figure 59c shows the DI values for

sensor 2 increasing, decreasing at 40,000 cycles and then increasing again. A similar trend is seen for sensor 3, except after 40,000 cycles its DI values stay almost constant. Therefore, this DI shows promising results but in order to verify this, more experiments would need to be done. The same DIs were also tested for the 300 kHz frequency.

The damage indices in the time domain were calculated for the 300 kHz frequency. Figure 60 through Figure 63 show the results for DI_1, DI_5, DI_8 and DI_9. Figure 61 and Figure 63 show the results for sensors 2 and 3 only.
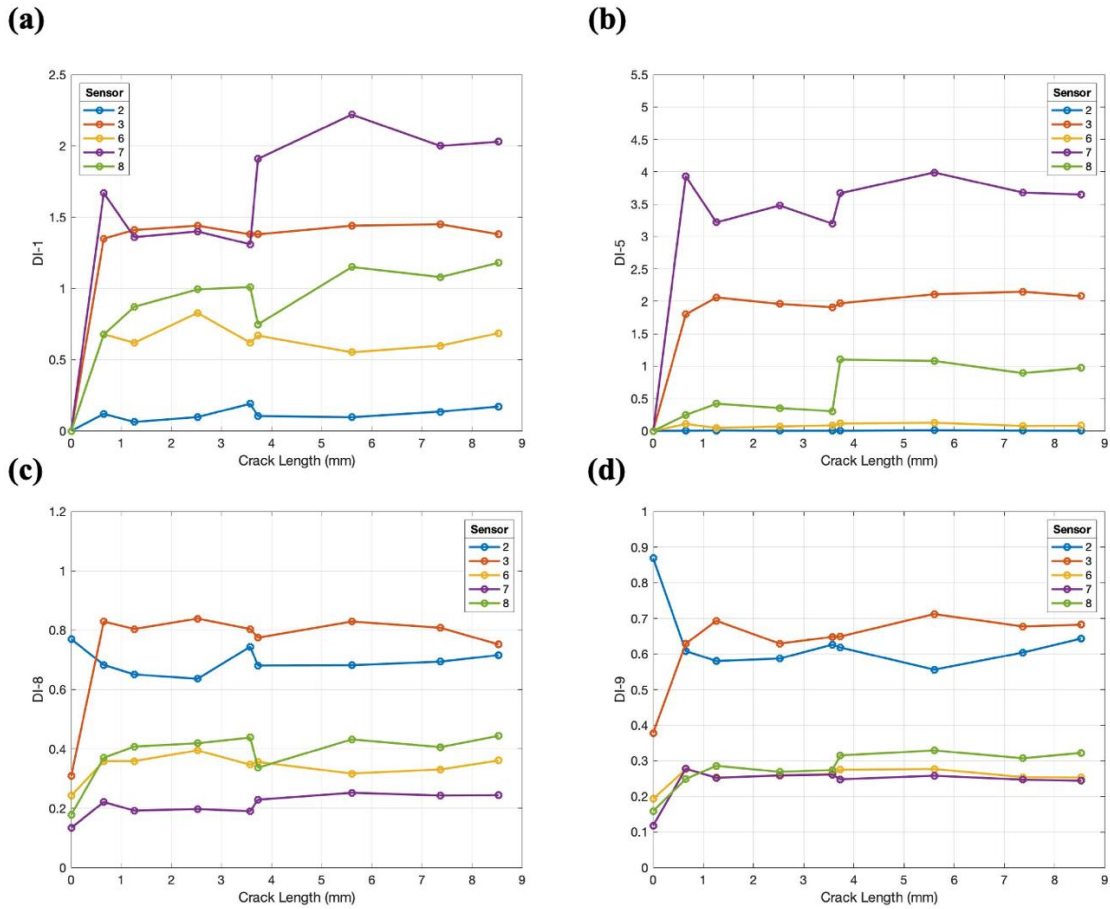
Figure 60. Damage index plot for (a) DI_1, (b) DI_5, (c) DI_8 and (d) DI_9 for all experimental sensors at a frequency of 300 kHz and a time range of 21.7-33 µs.

96
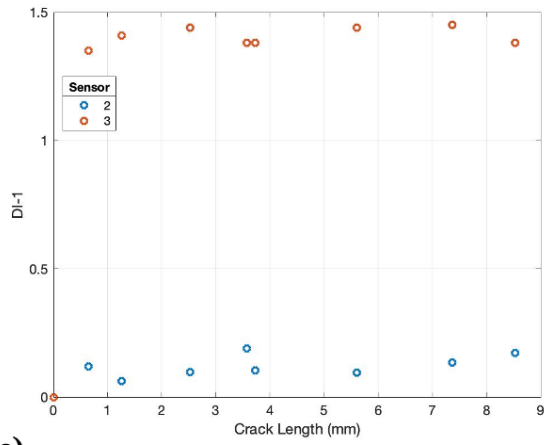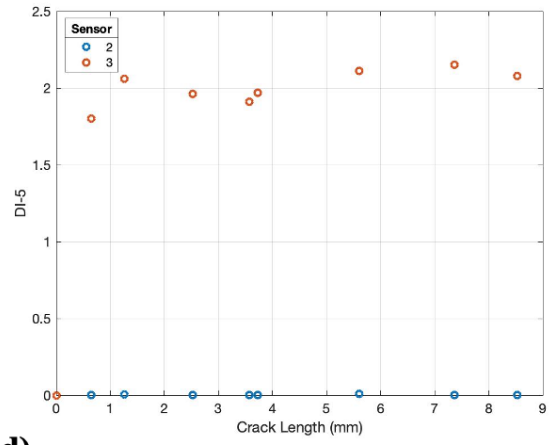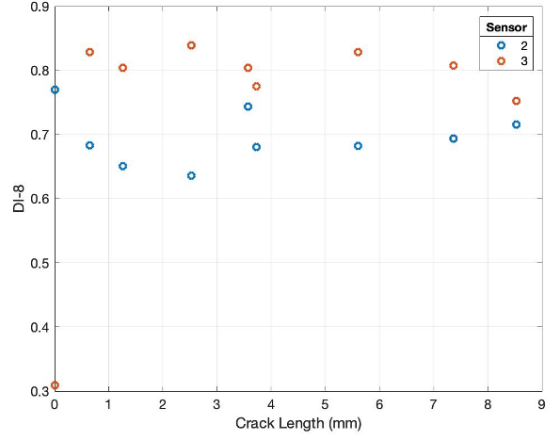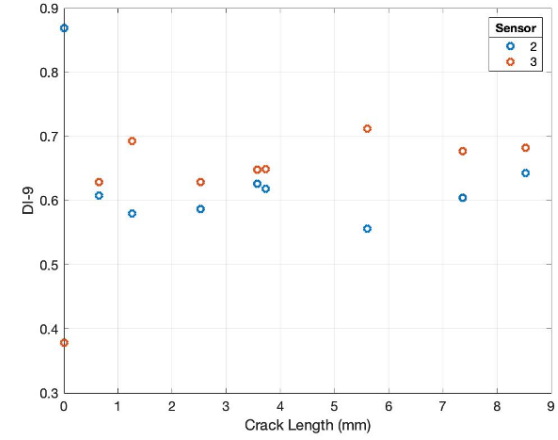
Figure 61. Damage index plot for (a) DI_1, (b) DI_5, (c) DI_8 and (d) DI_9 for sensors 2 and 3 only at a frequency of 300 kHz and a time range of 21.7-33 μs.
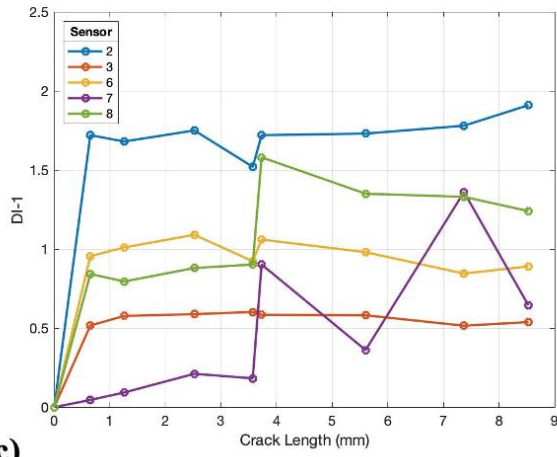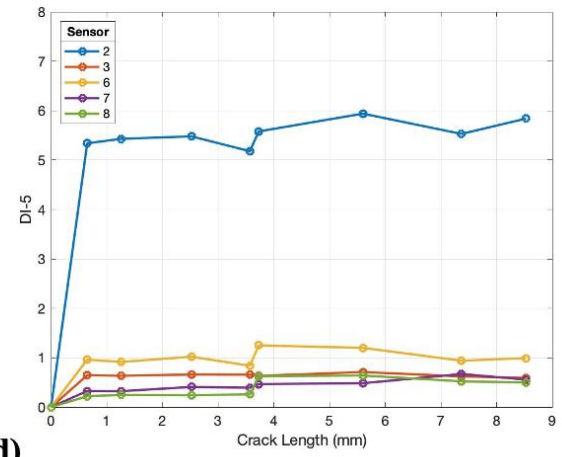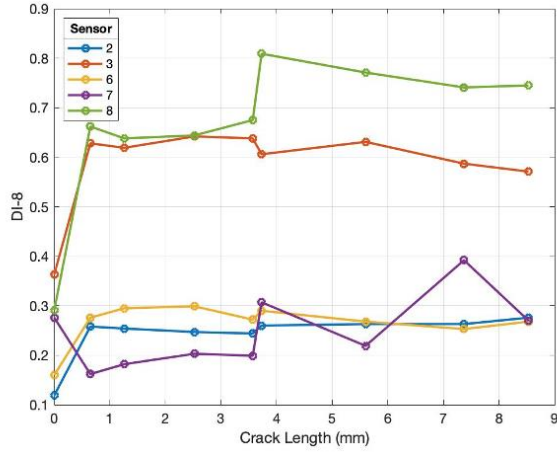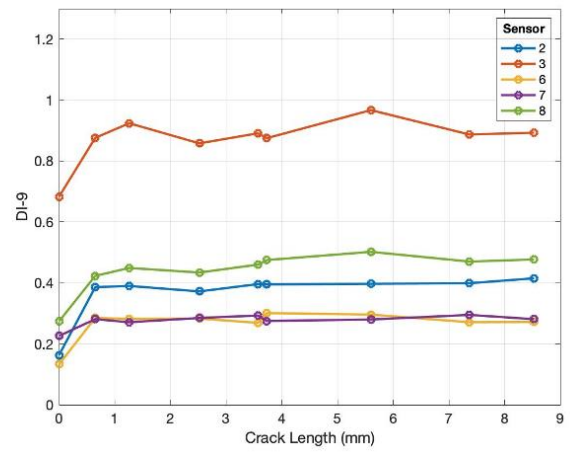
Figure 62. Damage index plot for (a) DI_1, (b) DI_5, (c) DI_8 and (d) DI_9 for all experimental sensors at a frequency of 300 kHz and a time range of 43-61 µs.

(a)

(b)

(c)

(d)
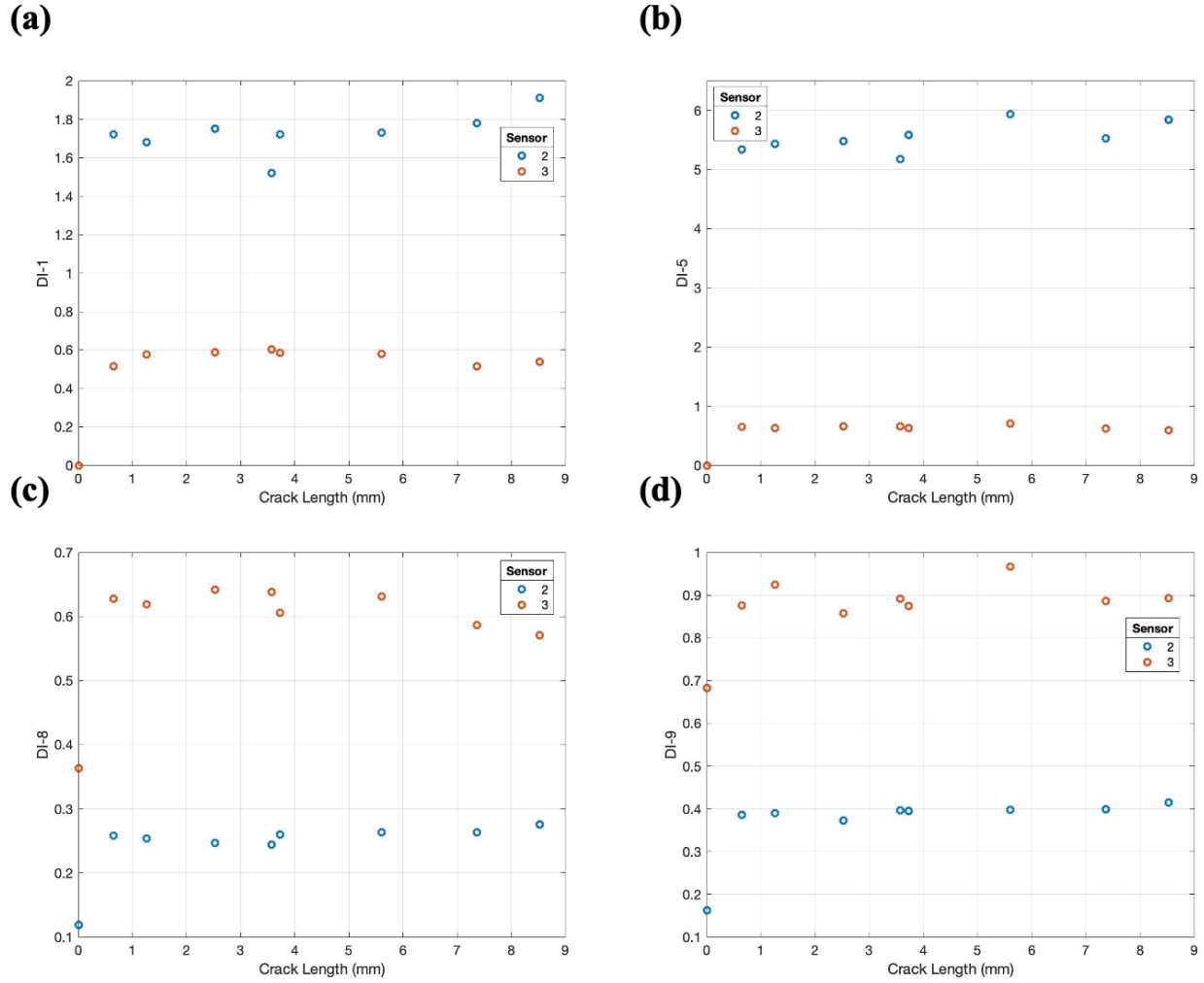
Figure 63. Damage index plot for (a) DI_1, (b) DI_5, (c) DI_8 and (d) DI_9 for sensors 2 and 3 only at a frequency of 300 kHz and a time range of 43-61 μs.

Figure 60a and Figure 60b suggest that sensor 2 is least sensitive since the DI was very low and did not change substantially. Figure 60c and Figure 60d show sensors 2 and 3 at the top. Sensor 2 starts out with the highest DI but ends lower than sensor 3. However, Figure 62a and Figure 62b suggest that sensor 2 is the most sensitive because the DI is the largest and seems to be trending upwards after the jump at 4 mm. Therefore, the time range chosen changed the

results drastically and the 43-61 µs time range produced results that corresponded to the numerical results in terms of sensor 2 having the largest DI values. Figure 61a shows sensor 3 having much larger DI values than sensor 2, while sensor 3 in Figure 61c and Figure 63c had slightly larger DI values. Sensor 3 displays an "m" shaped trend, where the DI increases and decreases by 4 mm, only to increase and decrease again after that. Only in Figure 63a and Figure 63b did sensor 2 have larger DI values than sensor 3. Therefore, for the 300 kHz frequency, in the 21.7-33 µs time range, sensor 3 dominates and in the 43-61 µs time range, sensor 2 is more sensitive to DI_1 and DI_5. To further obtain results for 300 kHz, frequency amplitude-based DIs and their normalizations are shown in Figure 64 and Figure 65.
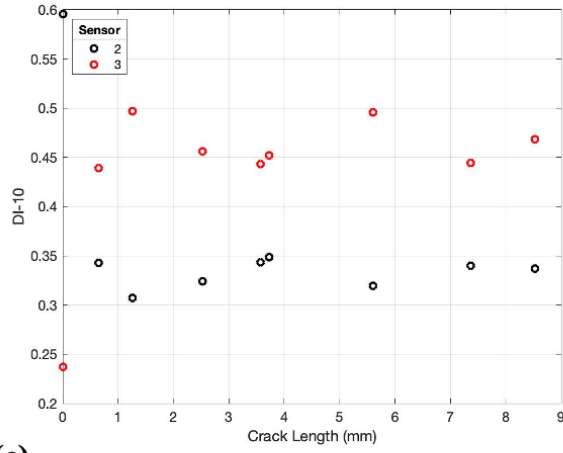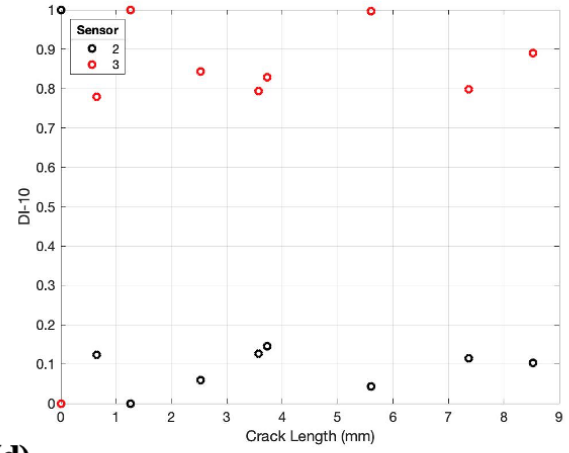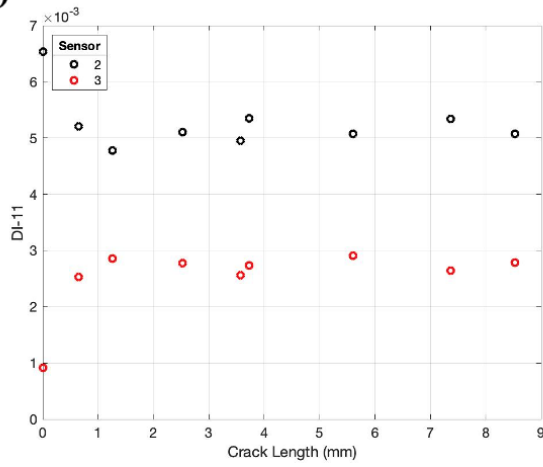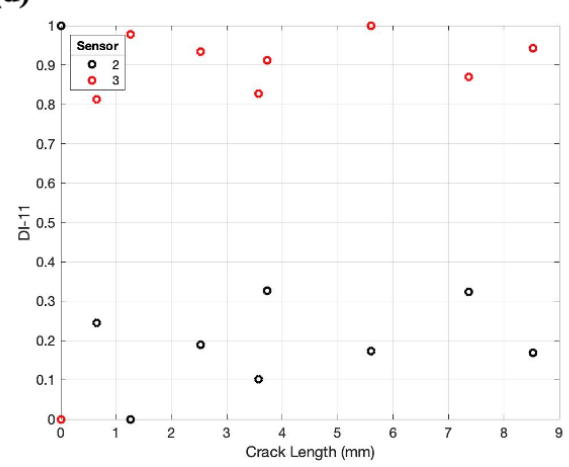
Figure 64. Damage indices based on frequency for (a) DI_{10}, (b) DI_{10} normalized, (c) DI_{11} and (d) DI_{11} normalized. Results are for sensors 2 and 3 at 300 kHz and 21.7-33 μs.
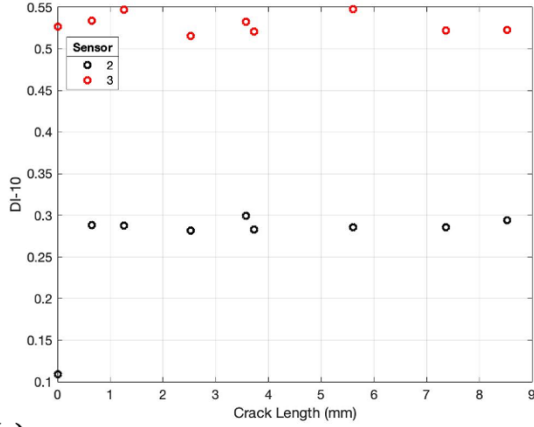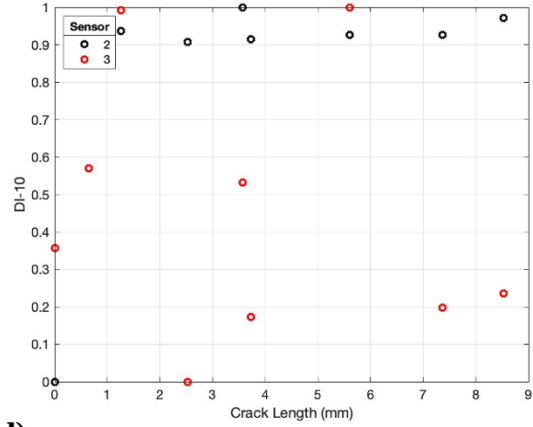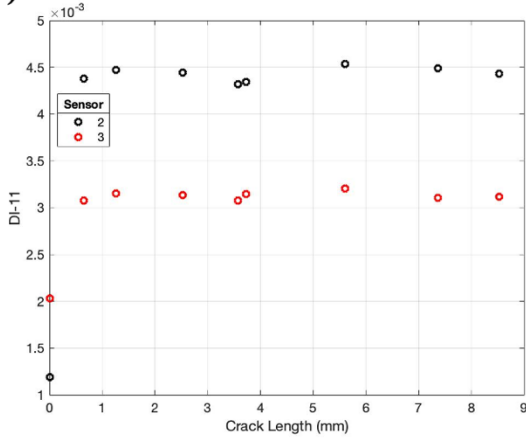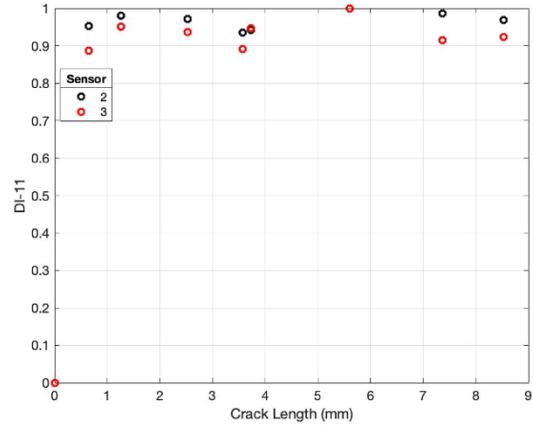
Figure 65. Damage indices based on frequency for (a) DI_{10}, (b) DI_{10} normalized, (c) DI_{11} and (d) DI_{11} normalized. Results are for sensors 2 and 3 at 300 kHz and 43-61 μs.

Sensor 3 in Figure 64a displays an "m" shaped trend, where the DI increases and decreases up to 4 mm and then repeats this again. Sensor 2 shows the same trend except reflected about the line $x = 0.4$. The DI for sensor 3 in Figure 64c increases in the very beginning, but then stays constant while sensor 2 decreases in the beginning and stays constant later. When the results were normalized, sensor 3 had the largest DI values in both cases. Figure 65a and Figure 65c show relatively constant DI values for both sensors after the initial jump in the beginning.

The next set of DIs calculated were based on phase shift. The results are shown in Figure 66 and Figure 67.

(a)

(b)

(c)

(d)
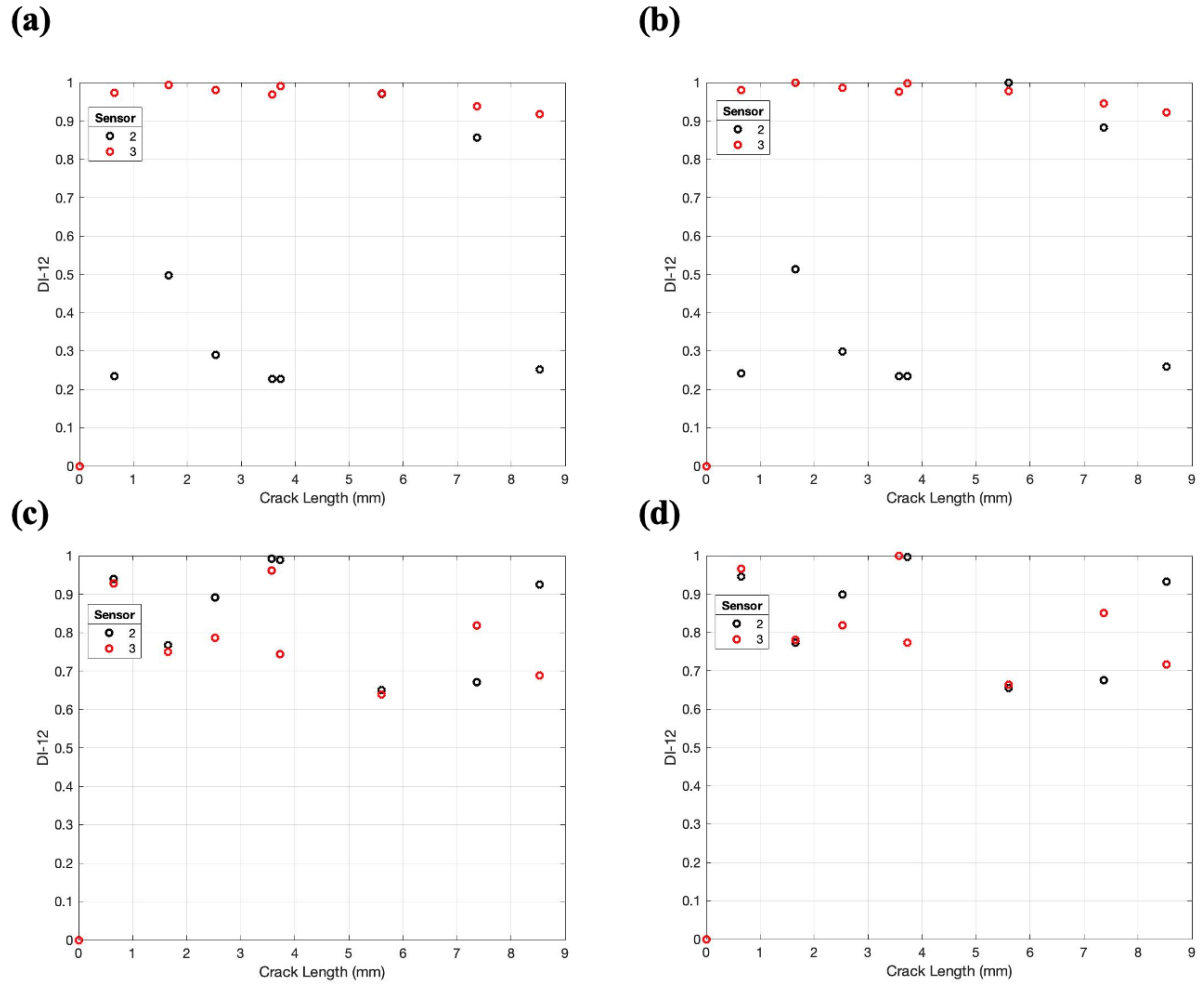
Figure 66. Damage index DI_{12} at 300 kHz for sensors 2 and 3 at (a) 21.7-33 µs, (b) 21.7-33 µs (normalized), (c) 43-61 µs, and (d) 43-61 µs (normalized).
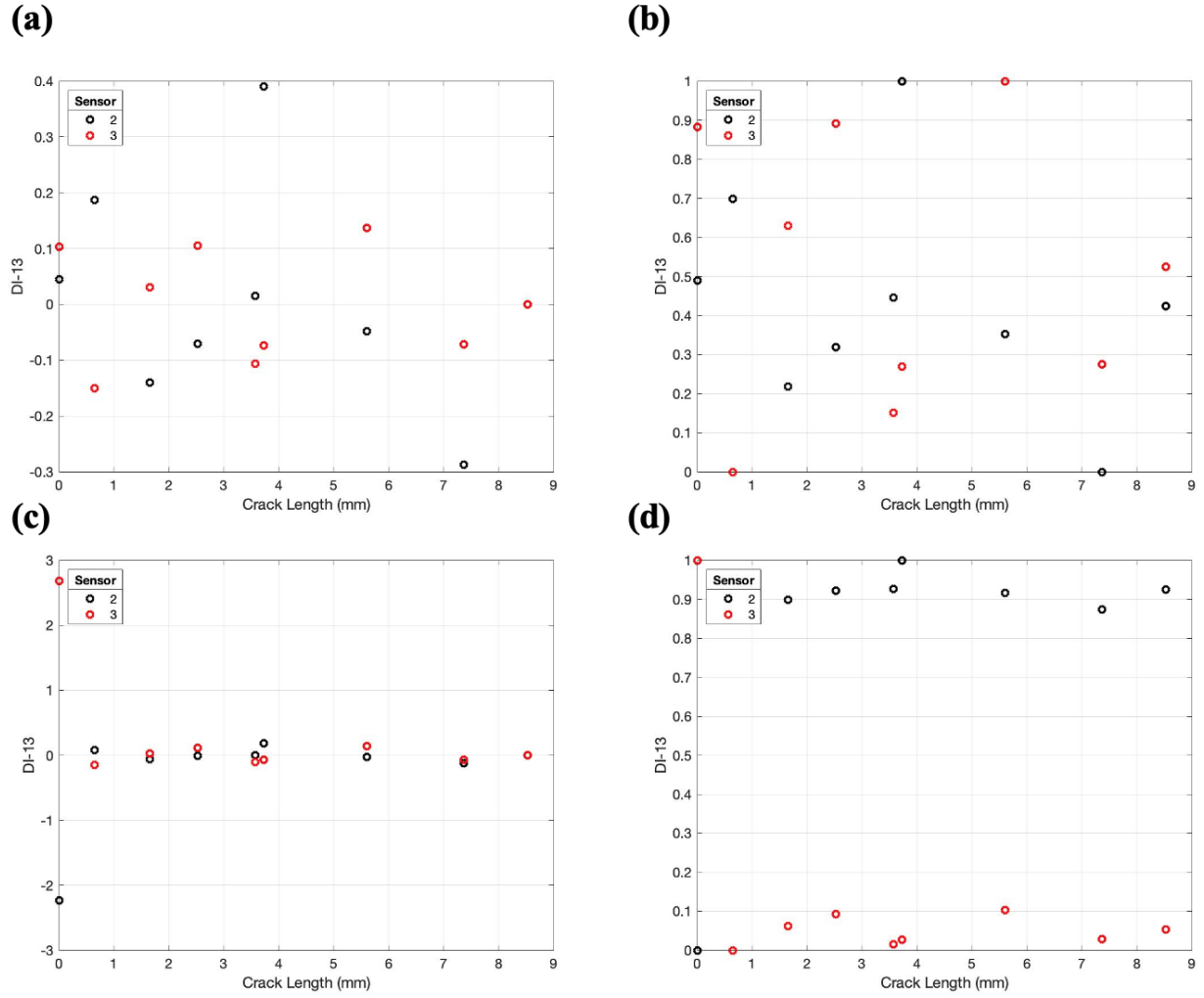
Figure 67. Damage index DI_{13} at 300 kHz for sensors 2 and 3 at (a) 21.7-33 μs, (b) 21.7-33 μs (normalized), (c) 43-61 μs, and (d) 43-61 μs (normalized).

Figure 66a shows a quick increase in DI for sensor 3, followed by a constant and then decreasing trend. The DI for sensor 2 increases sharply at about 2 mm and then decreases and reaches another peak at about 7 mm before decreasing again. Figure 66c and Figure 67a did not show any correlations between the DI and crack length. Figure 67c showed that the DIs for

104

sensors 2 and 3 were almost the same, but in the normalized results in Figure 67d, sensor 2 had larger DI values and a slight increasing trend until 4 mm.

The final DI was calculated based on frequency at the maximum amplitudes in the frequency spectra. The results are shown in Figure 68.
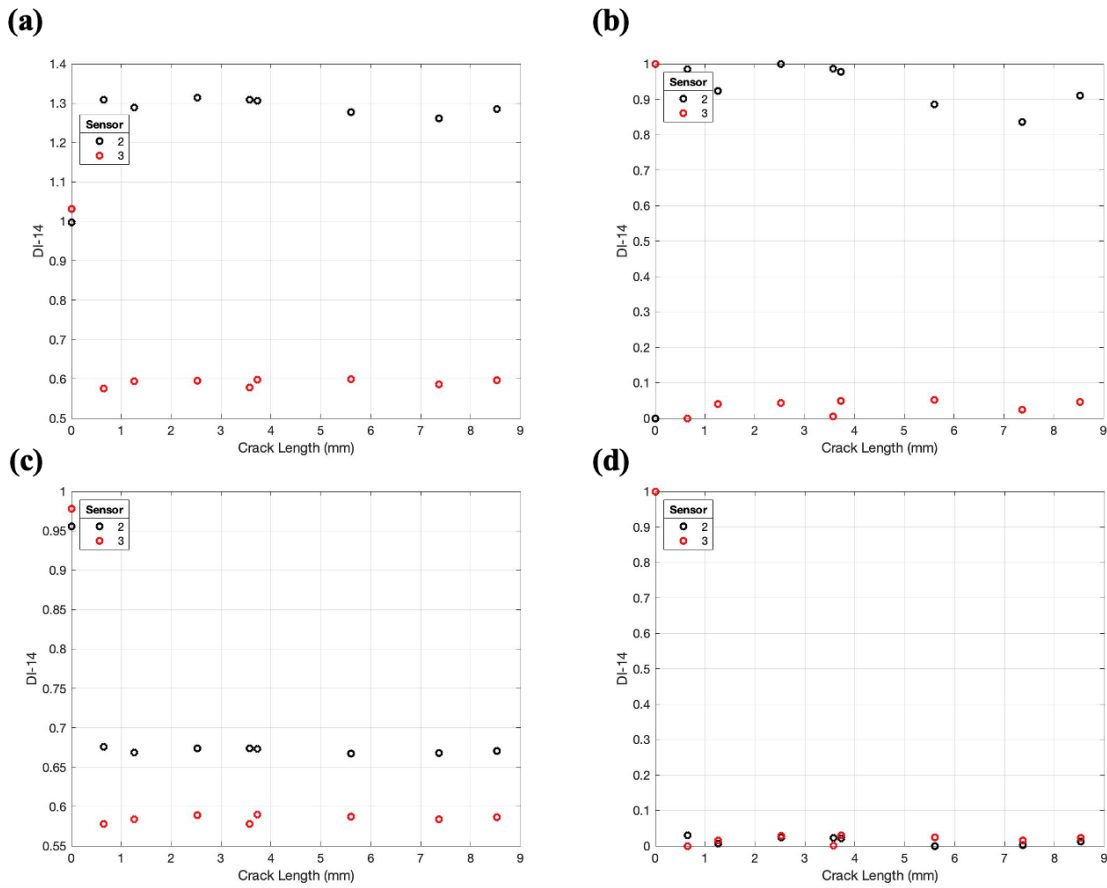
Figure 68. Damage index DI_{14} at 300 kHz for sensors 2 and 3 at (a) 21.7-33 μs, (b) 21.7-33 μs (normalized), (c) 43-61 μs, and (d) 43-61 μs (normalized).

Figure 68 shows the DI values for sensors 2 and 3 being almost constant. A small difference was observed in Figure 68b, where the DI for sensor 2 decreases towards the 8 mm crack length. Therefore this DI would not be effective at 300 kHz.

The plots shown below in Figure 69 and Figure 70 show the most effective amplitude and energy-based DIs (DI_1, DI_5, DI_8 and DI_9) for the experimental results with the location of sensors 2 and 3 relative to the crack length shown. Sensor 3 was actually located at about 10 mm relative to the crack length, but the data did not go past 9 mm and therefore the line for sensor 3 was placed at around 9 mm.
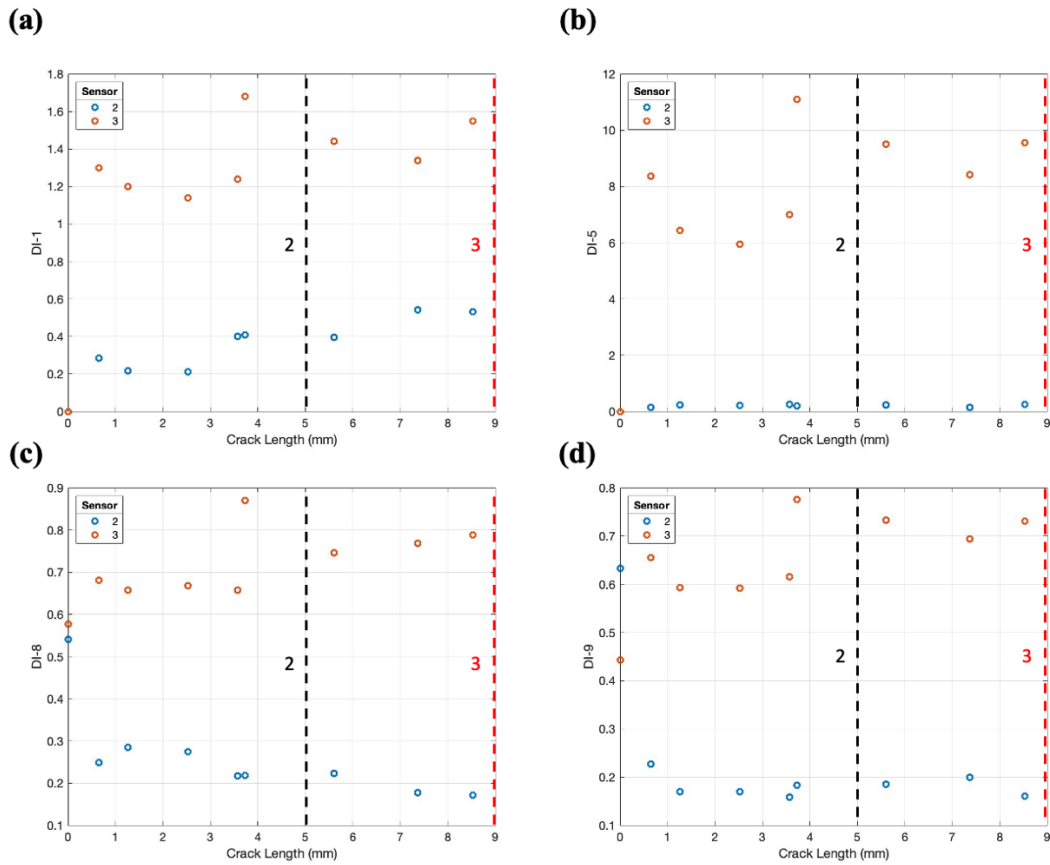
Figure 69. Damage index with sensor locations for (a) DI_1, (b) DI_5, (c) DI_8 and (d) DI_9 for sensors 2 and 3 only at a frequency of 400 kHz and a time range of 21.7-33 μs.
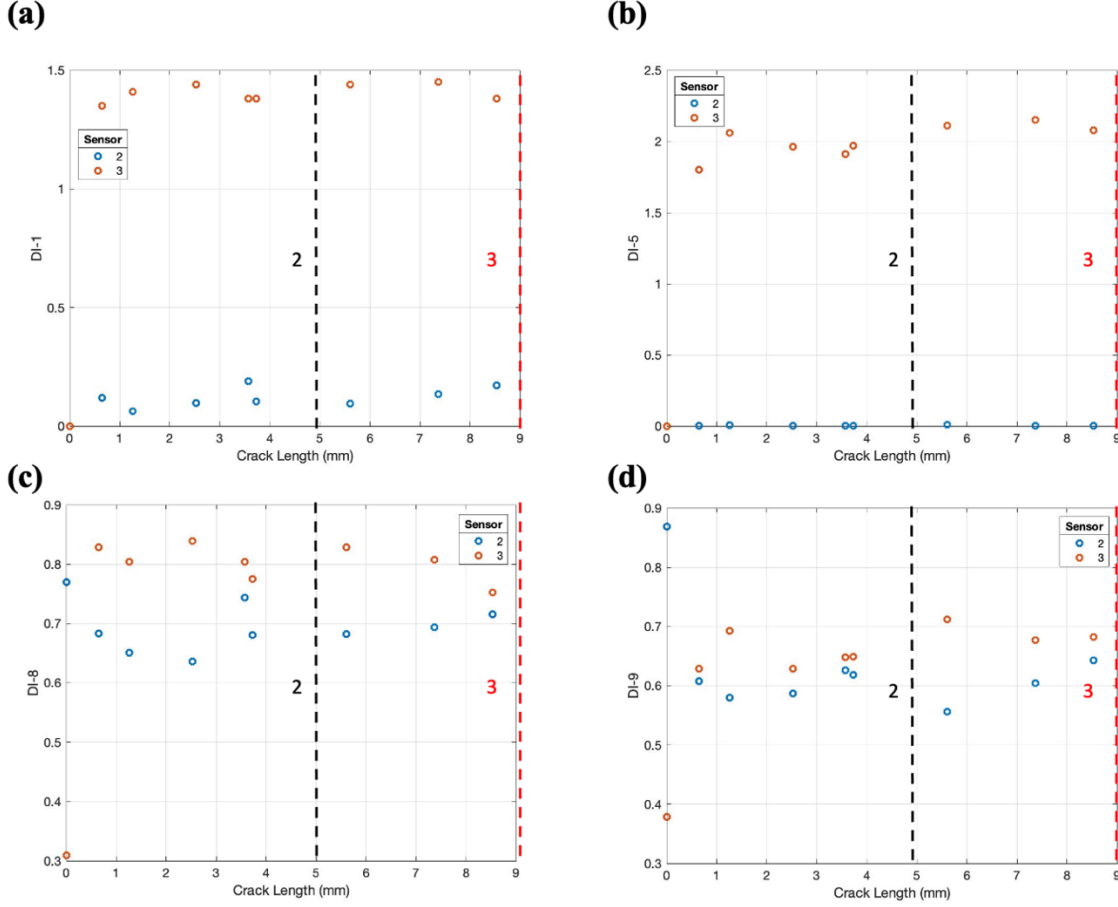
Figure 70. Damage index with sensor locations for (a) DI_1, (b) DI_5, (c) DI_8 and (d) DI_9 for sensors 2 and 3 only at a frequency of 300 kHz and a time range of 21.7-33 µs.

Figure 69 and Figure 70 show the classic amplitude and energy-based DIs for 400 kHz and 300 kHz within the same time range of 21.7-33 µs. They were expected to increase as the crack length increases because the amplitude and energy of the crack arrival signal should increase as the crack length becomes larger. It is clearly seen in Figure 69 that the DI for sensor 3 increases until 4 mm, when the specimen was removed, which follows what was expected. Figure 69a and Figure 69d show the same trend for sensor 2, but when the crack passed this sensor then the DI was not as effective. Figure 70a, Figure 70c and Figure 70d show the DI for

sensor 2 increasing up until 5 mm, where the sensor is located. After that, it either decreased or decreased and increased again.

The next set of effective DIs shown in Figure 71 and Figure 72 are based on frequency amplitude. These DI values were expected to increase because the reflection of the crack tip would increase while the surface wave parameters were practically constant. The normalized plots were only included if they showed better and more comparable results.
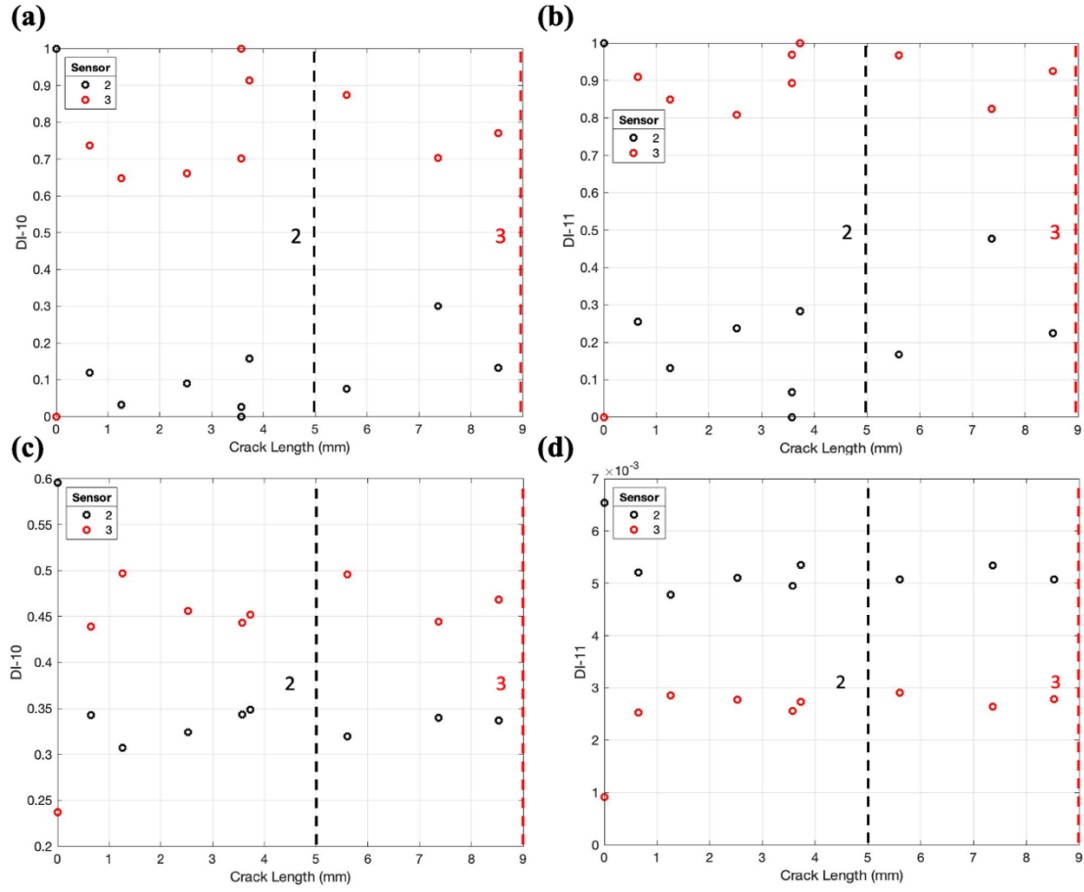
Figure 71. Damage index with sensor locations (a) DI_{10} normalized (400 kHz), (b) DI_{11} normalized (400 kHz), (c) DI_{10} (300 kHz) and (d) DI_{11} (300 kHz) for sensors 2 and 3 only at a time range of 21.7-33 μs.

(a)

(b)
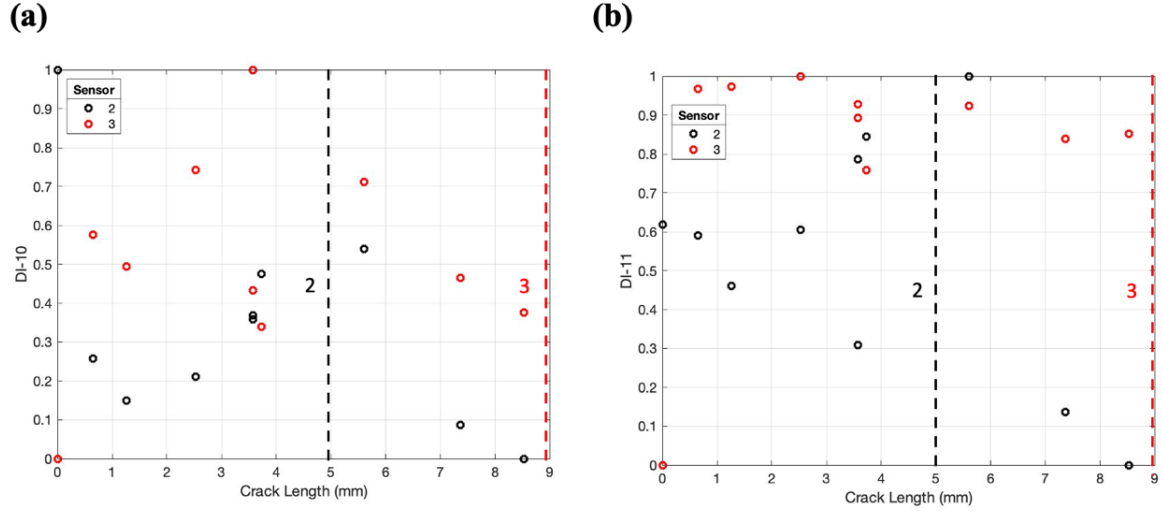
Figure 72. Damage index with sensor locations for (a) DI_{10} normalized and (b) DI_{11} normalized for sensors 2 and 3 only at a frequency of 400 kHz and time range of 43-61 μs.

Figure 71a and Figure 71b show the DI values for sensor 3 increasing up until about 4 mm. This is not apparent in Figure 72, but here, the DI values for sensor 2 increase until it the crack length reaches the sensor 2 location. There are some outlying points, which may be data fluctuations especially if the DI values are very small. This trend for sensor 2 is also seen in Figure 71c.

The next set of effective DIs (DI_{12}) shown in Figure 73 are based on phase shift parameters (signal difference coefficient). DI_{12} was expected to increase as described earlier in Chapter 3.
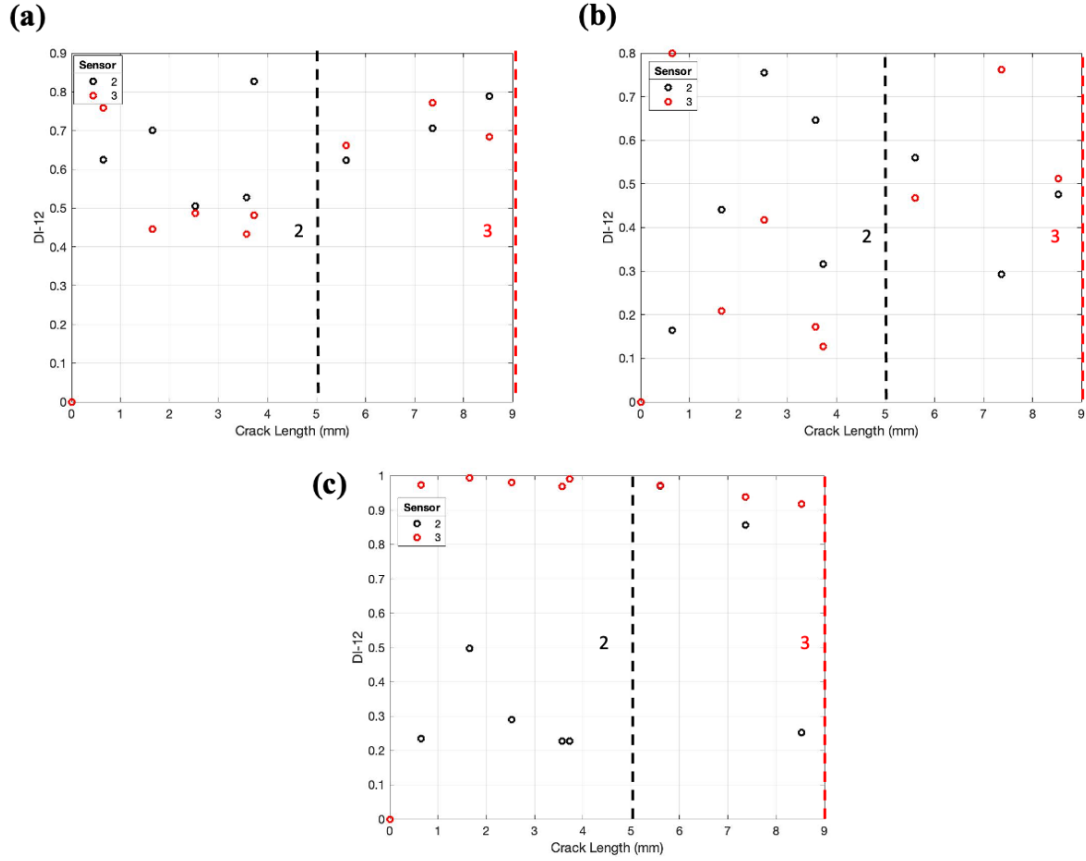
Figure 73. Damage index with sensor locations for (a) DI_{12} (400 kHz, 21.7-33 μs range), (b) DI_{12} (400 kHz, 43-61 μs range) and (c) DI_{12} (300 kHz, 21.7-33 μs range) for sensors 2 and 3.

Sensor 3 in Figure 73a showed an overall increasing trend after the initial jump and subsequent decrease. When it came close to the sensor 3 location, the DI started decreasing. Sensor 2 in Figure 73a and Figure 73b also showed an increasing trend that was interrupted by the jump at about 4 mm. Figure 73c showed a quick increase in DI for sensor 3, followed by a constant and then decreasing trend as it came closer to the location of sensor 3. Sensor 3 showed the expected results for the 400 kHz and 21.7-33 μs time range conditions. Sensor 2 showed the expected results for the 400 kHz and both time ranges.

The final set of effective DIs (DI_{14}) shown in Figure 74 are based on frequency at the highest amplitude in the frequency spectra. DI_{14} was expected to increase as described earlier in Chapter 3.
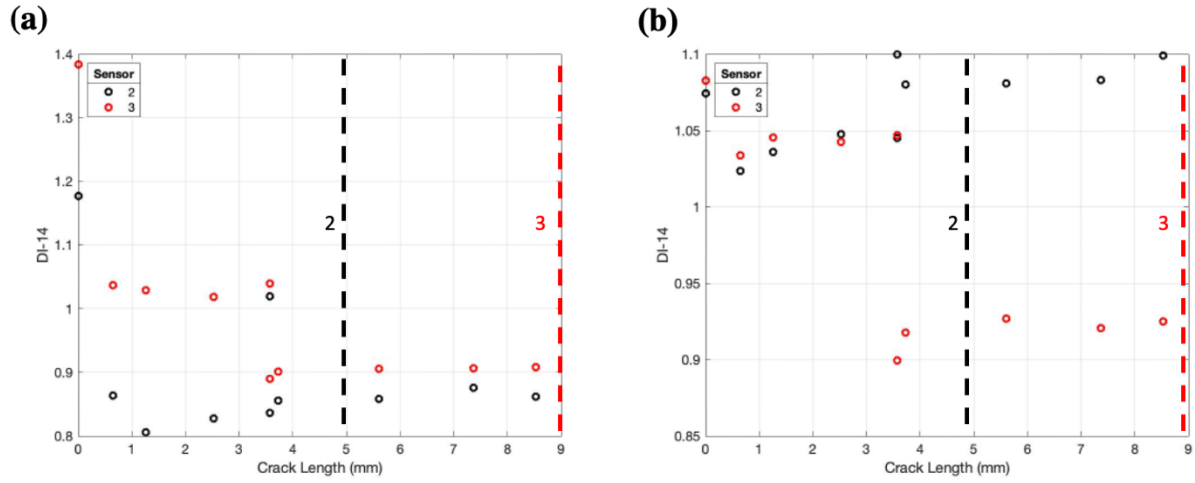
Figure 74. Damage index with sensor locations at 400 kHz for (a) DI_{14} (21.7-33 µs range) and (b) DI_{14} (43-61 µs range).

Figure 74a and Figure 74b show an increasing trend as the crack length reaches 4 mm. This was interrupted at 4 mm. However, if more experiments were conducted it would be possible to obtain constantly increasing DI values for DI_{14}.

A final comparison of the most effective DIs is presented in Table XVI in terms of efficient frequencies and time ranges.

Table XVI: COMPARISON OF MOST EFFECTIVE EXPERIMENTAL DI RESULTS

	Frequency (kHz)	
	Sensor 2	*Sensor 3*
Figure 69	400	400
Figure 70	300	300
Figure 71	300	400
Figure 72	400	-
Figure 73	400	400
Figure 74	400	400
	Time Range (µs)	
Figure 69	21.7-33	21.7-33
Figure 70	21.7-33	21.7-33
Figure 71	21.7-33	21.7-33
Figure 72	43-61	-
Figure 73	21.7-33 and 43-61	21.7-33
Figure 74	21.7-33 and 43-61	21.7-33 and 43-61

Both sensors 2 and 3 were more effective at 400 kHz than 300 kHz and at the first time range of 21.7-33. This agrees with the numerical results shown in Chapter 3. A comparison of the numerical and experimental results will be completed in Section 4.5.

4.5 Comparison Between Experimental and Numerical Results

Overall, there were quite a few differences between the numerical and experimental results regarding the inputs and DI values which are outlined in Table XVII and Table XVIII, respectively. The differences in the experimental setup and numerical modelling may have contributed to the differences in the DI plots. Even though some results seemed inconsistent, the general trend was observed that corresponded to the numerical results.

Table XVII: NUMERICAL AND EXPERIMENTAL INPUT DIFFERENCES

Parameter	Numerical	Experimental
Excitation signal	Sine wave sine shape.	Sine wave constant shape.
Excitation signal loading	Highly localized at one point.	Located at transmitter (finite area).
Crack approximation	Bézier polygon (looks almost like a right triangle). Crack becomes wider as it grows which produces better signals.	Does not look like a perfect polygon and has rough edges.
Sensor physics	Sensors were not assigned a piezoelectric physics. They were points.	Sensors were piezoelectric.
Model approximation	2D plain strain	3D
Separation of surface wave and crack wave arrivals	First surface arrival wave did not take up too much time and crack wave was easily separable. Wave amplitudes were the same.	First surface arrival wave took up too much time and overlapped into the expected time of flight which made it difficult to separate the crack. Wave amplitudes were not the same.

Table XVIII: NUMERICAL AND EXPERIMENTAL DI DIFFERENCES

DI	*Numerical*	*Experimental*
1		
5		
8		

9		
10		
12		

| 14 | |
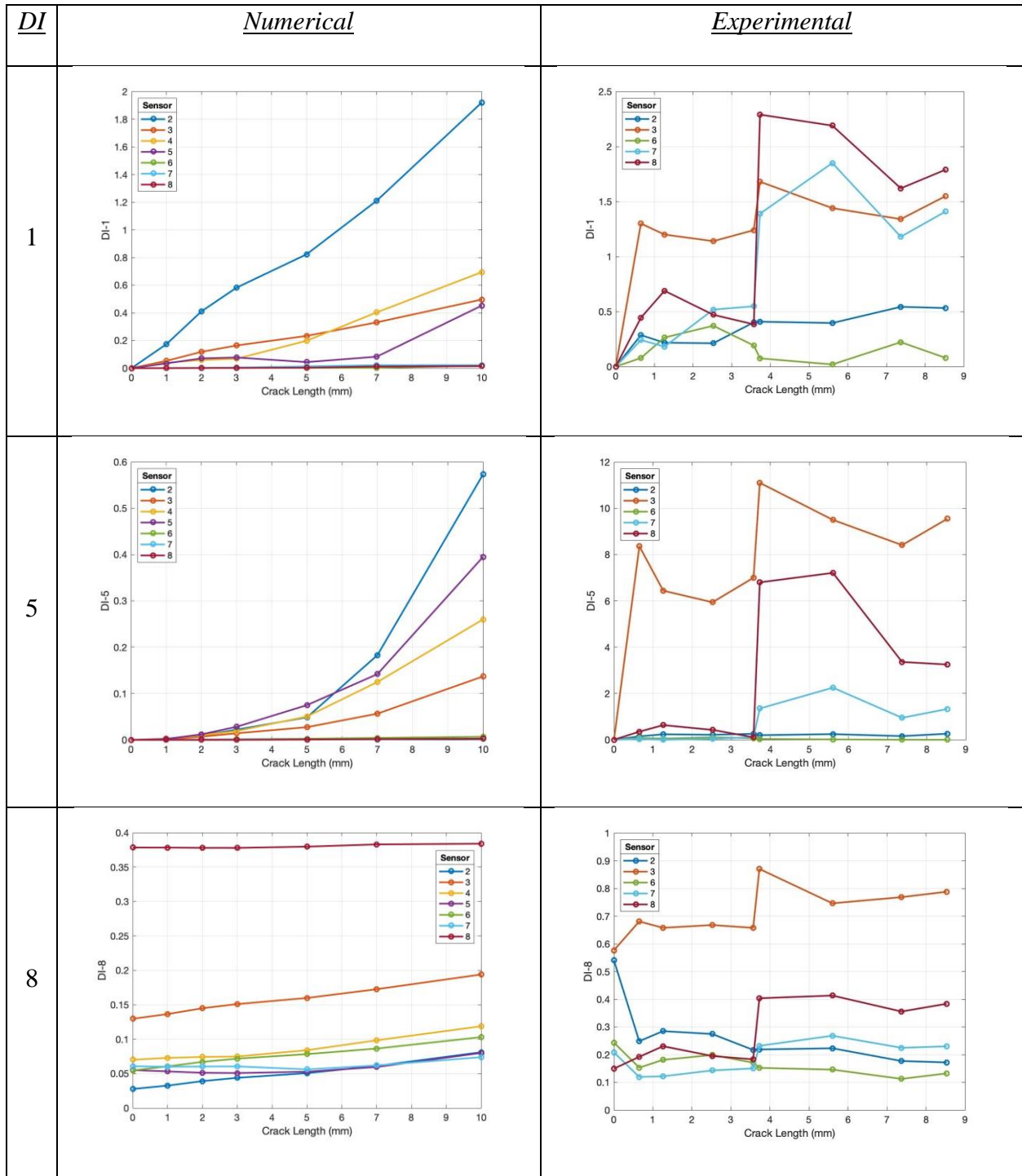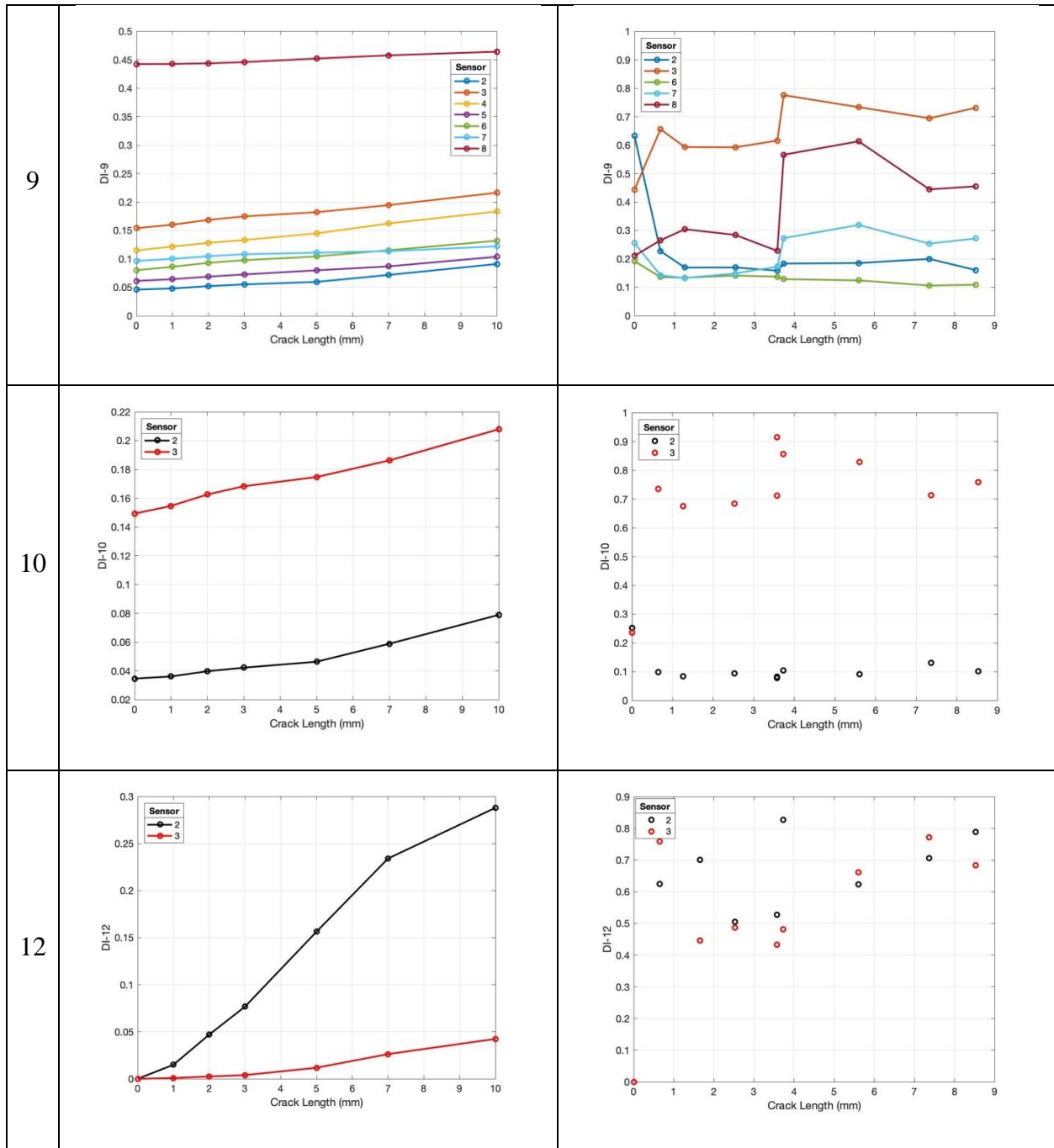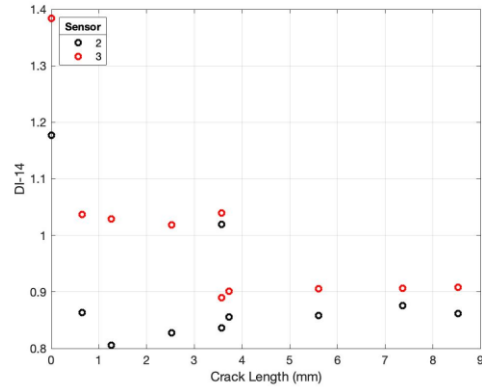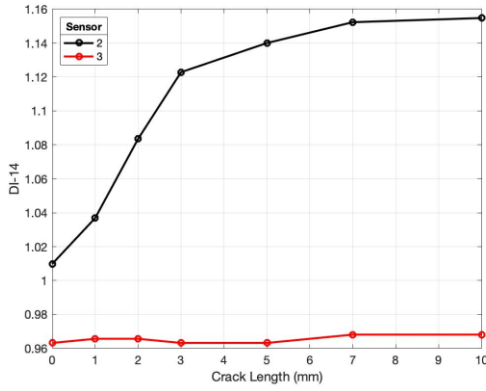
Table XVIII only shows the results for 400 kHz and the 21.7-33 μs range since these were the most effective parameters. Only DI_1, DI_5, DI_8, DI_9, DI_{10}, DI_{12} and DI_{14} were used because figures were available for both and they were the most effective DIs between both sets of data. For DI_1, sensor 2 shows an increasing trend for both numerical and experimental values. The DI values of sensors 7 and 8 may have been affected by specimen unloading and reloading to the load machine. For the experimental data, the DI suddenly jumped in between the 3-4 mm crack because the fatigue test was stopped at 40,000 cycles and then started again, which may have introduced experimental unknowns that affected the data. However, the numerical results show an upwards and sometimes linear trend. From all the DIs tested, it was concluded that the most compelling results were obtained from sensors 2 and 3 within the first time window (21.7-33 μs) at 400 kHz.

4.6 Summary

The experimental setup was presented which included the geometrical constraints and the machinery used in the laboratory for the ultrasonic measurements. The fatigue loading was used to grow the fatigue crack to 8.53 mm at 80,000 cycles. Images were captured with the optical microscope at each 10,000 cycle interval. The crack lengths were measured using MATLAB and used to correlate the ultrasonic data to them. Sensors 2, 3, 6, 7 and 8 were used as receivers to record the UT data. It was manipulated in the time and frequency domain to obtain DI values. The same DI equations were tested from Chapter 3 to compare the results at the end. The ones that produced the most acceptable results were DI_1, DI_5, DI_8, DI_9, DI_{10}, DI_{12} and DI_{14}. Therefore, the crack-free and surface wave reference DIs could be used to detect damage. Moreover, more attention was given to sensors 2 and 3 based on the numerical results. They were most sensitive at 400 kHz and the first time window of 21.7-33 µs which agreed with the numerical results.

5. CONCLUSION

5.1 Research Summary

Most metallic structures, especially airplanes, railways, and buildings, are subject to cyclic loading patterns. This leads to the formation of fatigue cracks which continue to grow as the number of cycles increases. Without proper inspection and monitoring, the fatigue crack can go unnoticed and eventually cause catastrophic failure. The purpose of this research was to examine the ability of guided wave UT in a phase array as a nondestructive evaluation method to detect a fatigue crack *in-situ* in a test specimen designed to grow a crack at the notch tip. This thesis provides a new method to categorize DIs depending on whether two signals are being used in the same waveform or time range. Damage indices based on maximum energy, maximum amplitude, frequency and phase shift parameters were used to correlate the UT data with fatigue crack length. UT is frequently used in the literature to detect damage in structures, with an emphasis on infrastructure like railways. People use this infrastructure every day, so it is imperative to monitor its health and prevent failure. Numerical and experimental studies were conducted to first obtain the stress distribution in the proposed geometry, and then to acquire the ultrasonic signals needed to calculate the various damage indices. The numerical studies investigated the maximum stresses for various geometries until it was verified that the crack would form at the notch tip first. They also provided the signals used for the DI calculation under ideal conditions at different crack lengths ranging from 0 mm – 10 mm. The final geometry was built and used in the experimental studies which examined the use of ultrasonic testing to detect the fatigue crack at the notch tip and the correlation of this data to the crack length.

5.2 Major Findings

The numerical static study confirmed that the maximum stresses at the notch tip and top hole were 340 MPa and 210 MPa, respectively. Since the notch tip stress was much larger than the endurance limit of steel, the crack was expected to form at the notch tip first. The numerical dynamic models provided insight into what patterns to expect in the damage index calculations. Since the numerical studies simulated ideal conditions, it was easier to find the time of flight, which is the time where the ultrasonic signal detected the crack as well as the second reflection from the crack. Within these time ranges, the amplitude and consequently energy for the sensors, especially sensor 2, increased because the crack length increased. Therefore, there was a linear correlation between DI and the crack length. However, this trend was not seen in all the amplitude and energy-based DI equations tested. One of the energy-based DIs increased sharply up to the 1 mm crack, and then decreased rapidly. Since the calculated energy increased as the crack length increased, as expected, the equation allowed larger energies in the denominator make the overall damage index smaller, as the baseline signal is constant. This trend was also seen in another energy-based DI; however it was also negative because the crack signal was subtracted from the baseline signal, and the crack signal was always larger. Overall, sensor 2 proved to be most sensitive as it had the largest DI when the waveforms were compared to the baseline, but when compared within the same waveform at different times, sensor 2 had the largest change. Sensor 3 was the next sensitive receiver, and both were used for further DI testing based on frequency and phase shift, which also showed linear correlations. The best results were produced at 400 kHz within the time range where the first crack reflection occurred. Acceptable DIs were narrowed down from each category and used to confirm the experimental

120

results. Therefore, DIs referencing the crack-free and the surface wave were both acceptable to predict damage. To validate this further, more experiments should be conducted.

The experimental study used UT to record signals propagating through the modified CT sample. Fatigue tests were completed to grow the crack, which were measured directly after each 10,000 cycle interval using the images processed with the MATLAB Image Processing Toolbox. By plotting the crack length vs. number of cycles, it was confirmed that the experiment took place in stage 2 of the crack propagation process, due to the linear correlation. The same DI equations were used from the numerical study. Similar acceptable DIs were obtained, and it was confirmed that sensors 2 and 3 were most sensitive at 400 kHz and the first time window of 21.7-33 μs which agreed with the numerical results.

5.3 Future Work

A substantial amount of research has been completed regarding UT and DIs, but there are more areas to explore within this topic. For example, the PoD curves can be applied to show which DI could give the best crack detection prediction and detect the smallest crack length. Figure 75a shows an example of the $\log(\hat{a})$ vs. $\log(a)$ plot created from the experimental data, where $\hat{a}$ represented the DI and a was the crack length. The PoD plot for sensor 2 at 400 kHz in window 2 (21.7-33 μs) is also shown in Figure 75b. A linear fit was added to obtain values of β_0 and β_1.
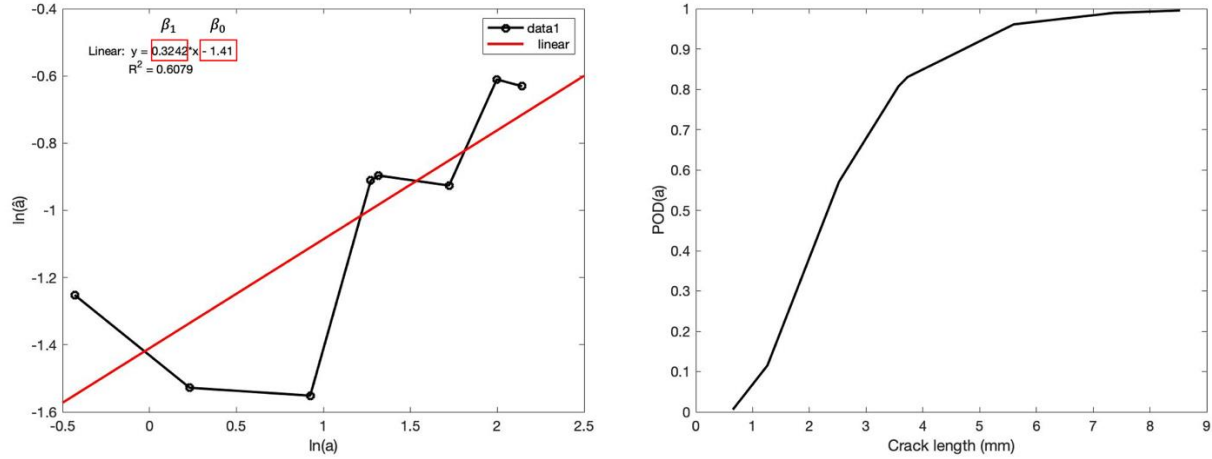
Figure 75. DI_1 PoD parameters: (a) $log(\hat{a})$ vs $log(a)$ plot and (b) corresponding PoD curve. This was created for sensor 2 in the first time range (21.7-33 μs).

The decision threshold $\hat{a}_{dec}$ was taken as the minimum DI value where anything above it was considered a "hit" and anything below it was considered a "miss" [47]. However, more research could be done to determine a more effective decision threshold that reveals certain damage if it is above a certain number. More experiments would need to be completed to obtain a threshold in a similar range. This would theoretically guarantee the presence of a crack using a certain damage index equation. The DI equation that can predict the smallest crack could be used for SHM to prevent the formation of large fatigue cracks.

Another area of research that can be expanded on is using acoustic emissions *in-situ* to obtain signals and calculate the DI from that data. Additional materials can be tested as well, including aluminum and concrete, since a significant amount of infrastructure is made with these materials. For further studies, an important concept can include minimizing the differences between numerical and experimental studies. The morphology of the actual crack can be obtained by metallographic studies to include more accurate crack shape in numerical models.

The numerical models can also be expanded to three-dimensional to include actual piezoelectric

sensors in a multiphysics model. Higher frequencies and more samples can be tested and

implemented in the field to validate the approach further.

CITED LITERATURE

1. Zhang, Lu, et al. "Acoustic Emission Signatures of Fatigue Damage in Idealized Bevel Gear Spline for Localized Sensing." *Metals (Basel)*, vol. 7, no. 7, 2017, pp. 242. *CrossRef*, https://explore.openaire.eu/search/publication?articleId=doajarticles::ef4d55c5f70291eaf6fa163eb94bbd9a, doi:10.3390/met7070242.

2. Kim, Geonwoo, et al. "Development of Phased Array Ultrasonic System for Detecting Rail Cracks." *Sensors and Actuators. A. Physical.*, vol. 311, 2020, pp. 112086. *CrossRef*, http://dx.doi.org/10.1016/j.sna.2020.112086, doi:10.1016/j.sna.2020.112086.

3. Yan, Jiajia, et al. "Active Monitoring of Fatigue Crack in the Weld Zone of Bogie Frames using Ultrasonic Guided Waves." *Sensors (Basel, Switzerland)*, vol. 19, no. 15, 2019, pp. 3372. *PubMed*, https://www.ncbi.nlm.nih.gov/pubmed/31370343, doi:10.3390/s19153372.

4. Zhu, Yanping, Fucai Li, and Wenjie Bao. "Fatigue Crack Detection Under the Vibration Condition Based on Ultrasonic Guided Waves." *Structural Health Monitoring*, vol. 20, no. 3, 2021, pp. 931-941. *CrossRef*, https://journals.sagepub.com/doi/full/10.1177/1475921719860772, doi:10.1177/1475921719860772

5. Jin, Hashen, et al. "Monitoring of Fatigue Crack Propagation by Damage Index of Ultrasonic Guided Waves Calculated by various Acoustic Features." *Applied Sciences*, vol. 9, no. 20, 2019, pp. 4254. *CrossRef*, https://explore.openaire.eu/search/publication?articleId=dedup_wf_001::32c636dbfb79fd81b67bafb9d54c7380, doi:10.3390/app9204254.

6. Tudose, Lucian, and Claudiu O. Popa. *Stress Intensity Factors Analysis on Cracks in the Hertzian Stresses Field of Teeth Gears*, 2007.

7. Zakar, Frank, and Erik Mueller. "Investigation of a Columbus, Ohio Train Derailment Caused by Fractured Rail." *Case Studies in Engineering Failure Analysis*, vol. 7, 2016, pp. 41-49. *CrossRef*, http://dx.doi.org/10.1016/j.csefa.2016.04.001, doi:10.1016/j.csefa.2016.04.001.

8. Fricke, Wolfgang. *Fatigue and Fracture of Ship Structures.* John Wiley & Sons, Ltd, Chichester, UK, 2017.

9. Connor, Robert, et al. "ARE YOU SURE THAT'S FRACTURE CRITICAL?." *Modern Steel Construction*, 2015.

10. ASTM E1316-17a, Standard Terminology for Nondestructive Examinations, ASTM International, West Conshohocken, PA, 2017, www.astm.org

11. Abbas, Muntazir, and Mahmood Shafiee. "Structural Health Monitoring (SHM) and Determination of Surface Defects in Large Metallic Structures using Ultrasonic Guided Waves." *Sensors (Basel, Switzerland)*, vol. 18, no. 11, 2018, pp. 3958. *PubMed*, https://www.ncbi.nlm.nih.gov/pubmed/30445724, doi:10.3390/s18113958.

12. Ushakov, V., D. Davydov, and L. Domozhirov. "Detection and Measurement of Surface Cracks by the Ultrasonic Method for Evaluating Fatigue Failure of Metals." *Russian Journal of Nondestructive Testing*, vol. 47, no. 9, 2011, pp. 631-641. *CrossRef*, doi:10.1134/S1061830911090099.

13. Michaels, Jennifer E. "Detection, Localization and Characterization of Damage in Plates with an in Situ Array of Spatially Distributed Ultrasonic Sensors." *Smart Materials and Structures*, vol. 17, no. 3, 2008, pp. 035035, http://iopscience.iop.org/0964-1726/17/3/035035, doi:10.1088/0964-1726/17/3/035035.

14. Syed Akbar Ali, Mohamed Subair, Anish Kumar, and Prabhu Rajagopal. "Signal Noise Based Transfer Function Approach for Reliability Estimation of Ultrasonic Inspection." *Ultrasonics*, vol. 96, 2019, pp. 276-283. *PubMed*, http://dx.doi.org/10.1016/j.ultras.2018.09.015, doi:10.1016/j.ultras.2018.09.015.

15. Felice, Maria V., and Zheng Fan. "Sizing of Flaws using Ultrasonic Bulk Wave Testing: A Review." *Ultrasonics*, vol. 88, 2018, pp. 26-42. *PubMed*, https://dx.doi.org/10.1016/j.ultras.2018.03.003, doi:10.1016/j.ultras.2018.03.003.

16. Wang, Rong, et al. "Nonlinear Ultrasonic Detection for Evaluating Fatigue Crack in Metal Plate." *Structural Health Monitoring*, vol. 18, no. 3, 2019, pp. 869-881. *CrossRef*, https://journals.sagepub.com/doi/full/10.1177/1475921718784451, doi:10.1177/1475921718784451.

17. Merazi Meksen, Thouraya, et al. "Automatic Crack Detection and Characterization During Ultrasonic Inspection." *Journal of Nondestructive Evaluation*, vol. 29, no. 3, 2010, pp. 169-174. *CrossRef*, doi:10.1007/s10921-010-0074-4.

18. Ostachowicz, Wieslaw, et al. "Damage Localisation in Plate-Like Structures Based on PZT Sensors." *Mechanical Systems and Signal Processing*, vol. 23, no. 6, 2009, pp. 1805-1829. *CrossRef*, http://dx.doi.org/10.1016/j.ymssp.2008.10.011, doi:10.1016/j.ymssp.2008.10.011.

19. Michaels, Thomas, and Jennifer Michaels. "Sparse Ultrasonic Transducer Array for Structural Health Monitoring." *AIP Conference Proceedings*, vol. 700, no. 1, 2004, https://aip.scitation.org/doi/abs/10.1063/1.1711788.

20. Kundu, Tribikram, Hayato Nakatani, and Nobuo Takeda. "Acoustic Source Localization in Anisotropic Plates." *Ultrasonics*, vol. 52, no. 6, 2012, pp. 740-746. *PubMed*, http://dx.doi.org/10.1016/j.ultras.2012.01.017, doi:10.1016/j.ultras.2012.01.017.

21. Du, Guofeng, et al. "Multiple Cracks Detection in Pipeline using Damage Index Matrix Based on Piezoceramic Transducer-Enabled Stress Wave Propagation." *Sensors (Basel, Switzerland)*, vol. 17, no. 8, 2017, pp. 1812. *PubMed*, https://www.ncbi.nlm.nih.gov/pubmed/28805666, doi:10.3390/s17081812.

22. Mal, Ajit, et al. "A Conceptual Structural Health Monitoring System Based on Vibration and Wave Propagation." *Structural Health Monitoring*, vol. 4, no. 3, 2005, pp. 283-293. *CrossRef*, https://journals.sagepub.com/doi/full/10.1177/1475921705055254, doi:10.1177/1475921705055254.

23. Banerjee, Sauvik, et al. "Autonomous Impact Damage Monitoring in a Stiffened Composite Panel." *Journal of Intelligent Material Systems and Structures*, vol. 18, no. 6, 2007, pp. 623-633. *CrossRef*, https://journals.sagepub.com/doi/full/10.1177/1045389X06067942, doi:10.1177/1045389X06067942.

24. Michaels, Jennifer E., Adam C. Cobb, and Thomas E. Michaels. *A Comparison of Feature-Based Classifiers for Ultrasonic Structural Health Monitoring*, vol. 5394, SPIE, Bellingham WA, Jul 21, 2004.

25. Lee, Sang E., and Jung-Wuk Hong. "Detection of Micro-Cracks in Metals using Modulation of PZT-Induced Lamb Waves." *Materials*, vol. 13, no. 17, 2020, pp. 3823. *CrossRef*, https://search.proquest.com/docview/2439754803, doi:10.3390/ma13173823.

26. Miguel Angel Climent-Llorca, et al. "Use of Higher-Harmonic and Intermodulation Generation of Ultrasonic Waves to Detecting Cracks due to Steel Corrosion in Reinforced Cement Mortar." *International Journal of Concrete Structures and Materials*, vol. 14, no. 6, 2020, pp. 903-919, https://www.dbpia.co.kr/journal/articleDetail?nodeId=NODE10494564.

27. Si, Liang, and Zongfeng Li. "Online Structural State Assessment for Aerospace Composite Structures using an Acousto-Ultrasonics-Based Multi-Damage Index Identification Approach." *Structural Health Monitoring*, vol. 19, no. 6, 2020, pp. 1790-1807. *CrossRef*, https://journals.sagepub.com/doi/full/10.1177/1475921719899334, doi:10.1177/1475921719899334.

28. Ono, K. *Acoustic Emission*, 2nd ed.; Rossing, Ed.; Springer Handbook of Acoustics: Berlin/Heidelberg, Germany, 2014; Chapter 30

29. Scruby, C. B. "An Introduction to Acoustic Emission." *Journal of Physics. E, Scientific Instruments*, vol. 20, no. 8, 1987, pp. 946-953. *CrossRef*, http://iopscience.iop.org/0022-3735/20/8/001, doi:10.1088/0022-3735/20/8/001.

30. Elasha, Faris, et al. "Application of Acoustic Emission in Diagnostic of Bearing Faults within a Helicopter Gearbox." *Procedia CIRP*, vol. 38, 2015, pp. 30-36. *CrossRef*, http://dx.doi.org/10.1016/j.procir.2015.08.042, doi:10.1016/j.procir.2015.08.042.

31. Strantza, Maria, et al. "Acoustic Emission Monitoring of Crack Propagation in Additively Manufactured and Conventional Titanium Components." *Mechanics Research Communications*, vol. 84, no. C, 2017, pp. 8-13. *CrossRef*, http://dx.doi.org/10.1016/j.mechrescom.2017.05.009, doi:10.1016/j.mechrescom.2017.05.009.

32. Kral, Zachary, Walter Horn, and James Steck. *Damage Detection in Metal Structures using Acoustic Emission*, 2009.

33. Holford, K. M., et al. "Damage Location in Steel Bridges by Acoustic Emission." *Journal of Intelligent Material Systems and Structures*, vol. 12, no. 8, 2001, pp. 567-576. *CrossRef*, https://journals.sagepub.com/doi/full/10.1177/10453890122145311, doi:10.1177/10453890122145311.

34. Syed Akbar Ali, Mohamed, and Prabhu Rajagopal. "Probability of Detection (PoD) Curves Based on Weibull Statistics."*Journal of Nondestructive Evaluation*, vol. 37, no. 2, 2018, pp. 1-13. *CrossRef*, https://search.proquest.com/docview/2006847140, doi:10.1007/s10921-018-0468-2.

35. Guan, Xuefei, et al. "Probabilistic Modeling and Sizing of Embedded Flaws in Ultrasonic Non-Destructive Inspections for Fatigue Damage Prognostics and Structural Integrity Assessment." *NDT & E International : Independent Nondestructive Testing and Evaluation*, vol. 61, 2014, pp. 1-9. *CrossRef*, http://dx.doi.org/10.1016/j.ndteint.2013.09.003, doi:10.1016/j.ndteint.2013.09.003.

36. Virkkunen, Iikka, et al. "Comparison of â Versus a and Hit/Miss POD-Estimation Methods: A European Viewpoint." *Journal of Nondestructive Evaluation*, vol. 38, no. 4, 2019, pp. 1-13. *CrossRef*, https://search.proquest.com/docview/2289611447, doi:10.1007/s10921-019-0628-z.

37. Pilyugin, S., and V. Lunin. "Determining the Probability of Detecting Flaws in Weld Joints by Phased-Array Ultrasonic Testing." *Russian Journal of Nondestructive Testing*, vol. 52, no. 6, 2016, pp. 332-338. *CrossRef*, https://search.proquest.com/docview/1880882838, doi:10.1134/S1061830916060085.

38. ASTM E647-15e1, Standard Test Method for Measurement of Fatigue Crack Growth Rates, ASTM International, West Conshohocken, PA, 2015, www.astm.org

39. Seitl, Stanislav, et al. "Comparison of Fatigue Crack Propagation Behaviour in Two Steel Grades S235, S355 and a Steel from Old Crane Way." *MATEC Web of Conferences*, vol. 310, 2020, pp. 34. *CrossRef*, https://search.proquest.com/docview/2442614460, doi:10.1051/matecconf/202031000034.

40. COMSOL Inc. "Understand, Predict, and Optimize Physics-Based Designs and Processes with COMSOL Multiphysics®.", 2021, https://www.comsol.com/comsol-multiphysics.

41. Velling, Andreas. "Material Fatigue Strength.", 2020.

42. American Institute of Steel Construction. *Steel Construction Manual.* AISC, Chicago, 2017.

43. Octal Metals. "ASTM A572 Grade 50, 60 Steel Plate Specification.", 2020, https://www.octalmetals.com/astm-a572-grade-50-60-steel-plate/.

44. MathWorks. "Hilbert Transform.", https://www.mathworks.com/help/signal/ug/hilbert-transform.html.

45. Abbasi, Z., and D. Ozevin. "Acoustoelastic Coefficients in Thick Steel Plates Under Normal and Shear Stresses." *Experimental Mechanics*, vol. 56, no. 9, 2016, pp. 1559-1575. *CrossRef*, https://search.proquest.com/docview/1880854144, doi:10.1007/s11340-016-0186-6.

46. MathWorks. "Practical Introduction to Frequency-Domain Analysis.", 2021, https://www.mathworks.com/help/signal/ug/practical-introduction-to-frequency-domain-analysis.html;jsessionid=486094919e6e29f8260c34200e52.

47. Department of Defense. *Nondestructive Evaluation System Reliability Assessment.* , 2009.

VITA

Tanja Rakovic is currently a pursuing a Master of Science in Civil Engineering at the University of Illinois at Chicago, which she will obtain in 2021. Ms. Rakovic graduated with honors with a Bachelor of Science in Civil Engineering from the University of Illinois at Chicago in 2020. Ms. Rakovic is the co-author of a paper of work in progress: "Reconstructing 3D Models of Steel Girders for Assessing Localized Defects by Unmanned Aerial Vehicles".